Surface Energy and Mass Balance Model for Greenland Ice Sheet and Future Projections

by

Xiaojian Liu

A dissertation submitted in partial fulfillment
of the requirements for the degree of
Doctor of Philosophy
(Atmospheric, Oceanic and Space Sciences)
in The University of Michigan
2017

Doctoral Committee:

Associate Professor Jeremy N. Bassis, Chair
Associate Professor Brian Arbic
Associate Professor Mark Flanner
Professor Richard Rood

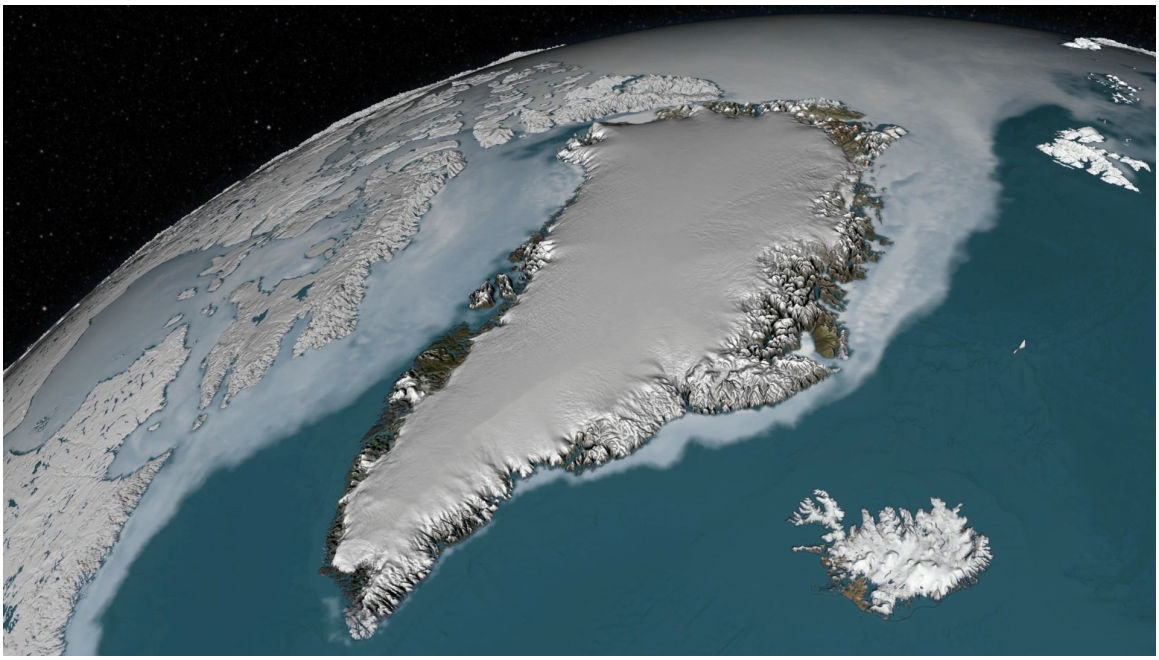

The Greenland Ice Sheet, figure courtesy of NASA Goddard video.

For all the people

ACKNOWLEDGEMENTS

There have been so many people I would like to extend my thanks to, who have been generously giving me help through the completion of this dissertation.

Foremost, I would like to express my earnest thanks to my advisor, Professor Jeremy N. Bassis for his enormous guidance, encouragement and support throughout my PhD life. He is one of the most brilliant and intelligent persons I have ever met. Every time when I got stuck in my research, he always helped me come out with his knowledge and insights. He has been not only an excellent academic advisor, but also a great mentor. He has not only provided me lots of advices on my research, but also many suggestions on present the findings. Working with him has been always an challengeable and enjoyable thing.

I would like to thank the rest of my dissertation committee members, Professors Richard B Rood, Mark Flanner and Brian Arbic, for their time and efforts on improving my thesis by providing insightful comments and suggestions. I would like to especially thank Professor Mark Flanner, who has given me lots of insights on snow and ice albedo and on my energy and mass balance model. I appreciate Professor Arbic's intriguing lectures on physical oceanography and also the impressive trip to the Great Lakes. I would also like to thank Professor Richard Rood for his help in finding CMIP5 data for the upper bound surface mass loss project for Greenland Ice Sheet.

I would also like to thank Professor Tony England, Professor Derek Posselt and Professor Allison Steiner for their kind help on resolving my scientific issues. I also ap-

preciate many faculties in the department, from whom I have received many excellent lectures and instructions on climate sciences.

Many thanks to Sandra Pytlinski, Sandee Hicks and Rachel Long for their administrative support, and to Darren Britten-Bozzone, Faye Ogasawara and other IT specialists for their timely help with my computer issues. Without them, I could not have conducted my research so successfully.

I would like to say thank you to many of my friends who have been supporting me from every aspect in graduate school, including Chaoyi Jiao, Yue Ma, Lizz Ultee, Yuxi Chen, Fang Pan, Yinsi Shou, to name a few.

Finally, I would like to express my deep gratitude to my family, for their support and encouragement helping me going through all of the difficult times during my graduate life.

TABLE OF CONTENTS

LIST OF FIGURES

Figure

LIST OF TABLES

Table

LIST OF ABBREVIATIONS

DEM Digital Elevation Model

MAR Modèle Atmosphérique Régional

PDD Positive Degree Day

PMM5 Polar Fifth-generation Mesoscale Model

RACMO 2.1 Regional Atmosphere Climate Model version 2.1

SMB Surface Mass Balance

SISVAT Soil Ice Snow Vegetation Atmosphere Transfer

ABSTRACT

Surface Energy and Mass Balance Model for Greenland Ice Sheet and Future Projections

by

Xiaojian Liu

Chair: Jeremy N. Bassis

The Greenland Ice Sheet contains nearly 3 million cubic kilometers of glacial ice. If the entire ice sheet completely melted, sea level would raise by nearly 7 meters. There is thus considerable interest in monitoring the mass balance of the Greenland Ice Sheet. Each year, the ice sheet gains ice from snowfall and loses ice through iceberg calving and surface melting. In this thesis, we develop, validate and apply a physics based numerical model to estimate current and future surface mass balance of the Greenland Ice Sheet. The numerical model consists of a coupled surface energy balance and englacial model that is simple enough that it can be used for long time scale model runs, but unlike previous empirical parameterizations, has a physical basis. The surface energy balance model predicts ice sheet surface temperature and melt production. The englacial model predicts the evolution of temperature and meltwater within the ice sheet. These two models can be combined with estimates of precipitation (snowfall) to estimate the mass balance over the Greenland Ice Sheet. We first compare model performance with in-situ observations to demonstrate that the model works well. We next evaluate how predictions are degraded when we

statistically downscale global climate data. We find that a simple, nearest neighbor interpolation scheme with a lapse rate correction is able to adequately reproduce melt patterns on the Greenland Ice Sheet. These results are comparable to those obtained using empirical Positive Degree Day (PDD) methods. Having validated the model, we next drove the ice sheet model using the suite of atmospheric model runs available through the CMIP5 atmospheric model inter-comparison, which in turn built upon the RCP 8.5 (business as usual) scenarios. From this exercise we predict how much surface melt production will increase in the coming century. This results in 4–10 cm sea level equivalent, depending on the CMIP5 models. Finally, we try to bound melt water production from CMIP5 data with the model by assuming that the Greenland Ice Sheet is covered in black carbon (lowering the albedo) and perpetually covered by optically thick clouds (increasing long wave radiation). This upper bound roughly triples surface meltwater production, resulting in 30 cm of sea level rise by 2100. These model estimates, combined with prior research suggesting an additional 40–100 cm of sea level rise associated with dynamical discharge, suggest that the Greenland Ice Sheet is poised to contribute significantly to sea level rise in the coming century.

CHAPTER I

Introduction

1.1 Cryosphere

The cryosphere is the part of Earth's surface where water is in solid form, including ice sheets, ice shelves, glaciers, ice caps, sea ice, river ice, lake ice, snow and frozen ground (*Cuffey and Paterson*, 2010; *Vaughan et al.*, 2013). Some parts of the cryosphere, such as lake ice and sea ice, vary seasonally, while some other components are more permanent, such as glaciers and ice sheets (*Bates et al.*, 1984; *Barry and Gan*, 2011). The cryosphere plays an important role in the Earth's climate system, water cycle and sea level rise (*Barry and Gan*, 2011). As part of the global climate system, the cryosphere influences the Earth surface energy budget through its large surface area, which covers about 10 percent of the Earth's surface, and high albedo, which plays a key role in the Earth's planetary albedo and radiative balance (*Hartmann*, 2015).

The Antarctic and Greenland ice sheets together contain more than 99 percent of the freshwater ice on Earth and about 75 percent of the world's fresh water. If the entire ice sheets melted, the sea level could rise about 70 meters (*Barry and Kiladis*, 1982; *Lythe and Vaughan*, 2001). This is not only a threat to people who live near the ocean, but also a potential disaster for maritime life (*FitzGerald et al.*, 2008). Mountain glaciers are important sources of clean water for animals and crucial for the

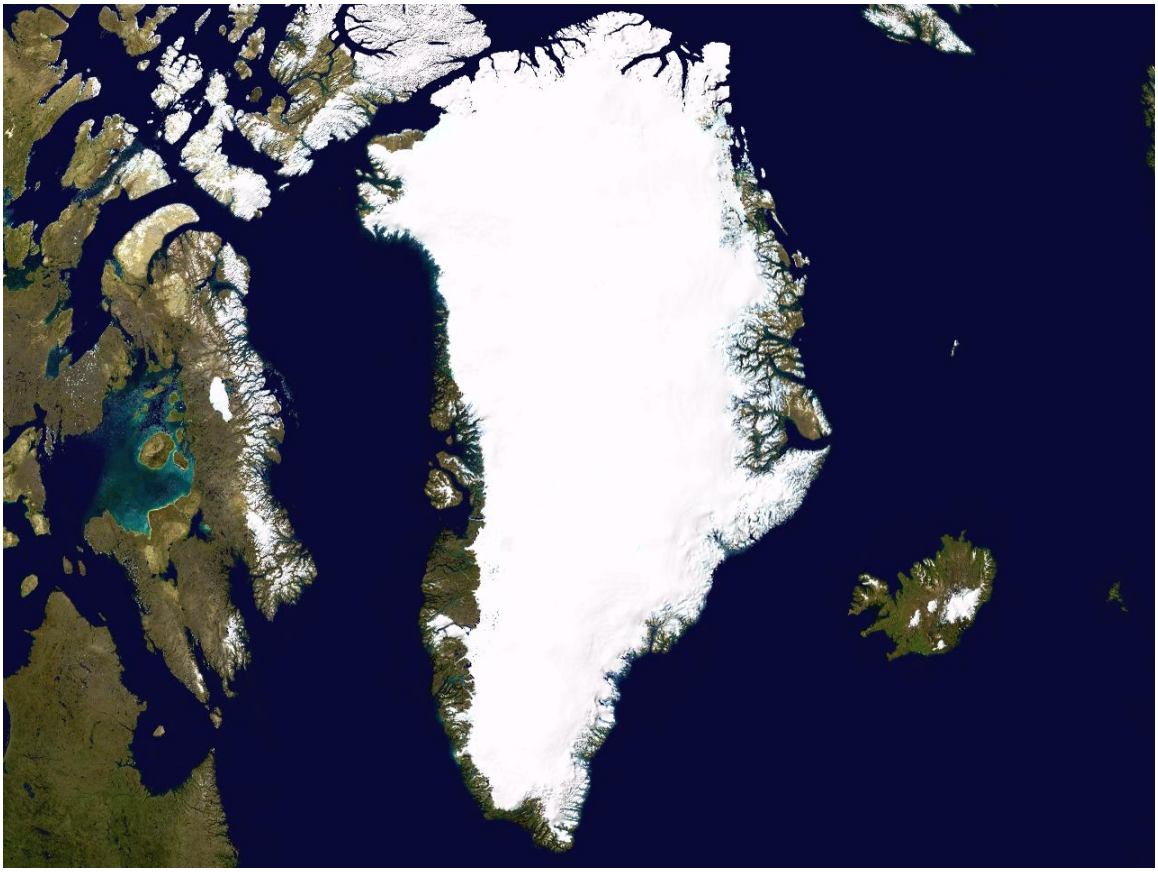

Figure 1.1: The map of Greenland Ice Sheets (indicated by the snow covered white area) and its location in the northern hemisphere based on *Dahl-Jensen et al.* (2009).

daily lives of people (*Kehrwald et al.*, 2008; *Immerzeel et al.*, 2010). Sea ice can affect the atmospheric and ocean circulation (*Mori et al.*, 2014). Thus, the cryosphere has an essential control over the physical, biological and social part of Earth's system. Since all these components of cryosphere are sensitive to the climate change, the investigation of cryosphere will provide signatures about climate change (*Flato et al.*, 2013).

1.2 Greenland Ice Sheet

An ice sheet is a body of ice, formed by accumulation of snowfall over many years, with area larger than 50,000 km^2. Currently, there are only two ice sheets on Earth, the Greenland Ice Sheet and Antarctic Ice Sheet. The Greenland Ice Sheet as shown in Figure 1.1, is the largest body of ice in the Northern Hemisphere and the second largest ice sheet in the world. It extends about 1.7 million square kilometers, stretching 2600 km, and covers about 85 percent all the surface of Greenland (*Morlighem et al.*, 2014). The Greenland Ice Sheet consists of about 2.9 million km^3 of ice and would cause the sea level to rise about 7 m if completely melted (*Ekholm and Krabill*, 2001), which would submerge many of the world's heavily populated coastal cities. Figure 1.2 shows the elevation of the bedrock underneath the Greenland Ice Sheet, and Figure 1.3 shows the thickness of the ice sheet (*Bamber et al.*, 2013). These plots show that the base of Greenland is below the sea level, especially in the central part. Most of the Greenland Ice Sheet is over 1000 meters thick with a maximum thickness of 3200 m.

As shown in Figure 1.4, every year snow falls and accumulates on the surface of the ice sheet. The freshly fallen snow, with density about 300 kg m^{-3}, gradually transforms into glacier ice density about 910 kg m^{-3} under the influence of gravity and successive yearly snowfall. Under the influence of gravity, the unbalanced accumulated mass leads ice streams downward from the center of the ice sheet to the edge suggest moving as indicated. Ice shelves form at the extended part where ice meets ocean. Ice sheets are surrounded by sea ice. The Greenland Ice Sheet gains mass from the precipitation and losses mass from both surface melt and iceberg calving at the front of ice shelf.

The Greenland Ice Sheet area reached its maximum during the last glacial maximum (LGM) of the latest Pleistocene (23 ka), at which time it was about 140% larger than at present (*Lambeck et al.*, 2002; *Huybrechts*, 2002). It is thought that

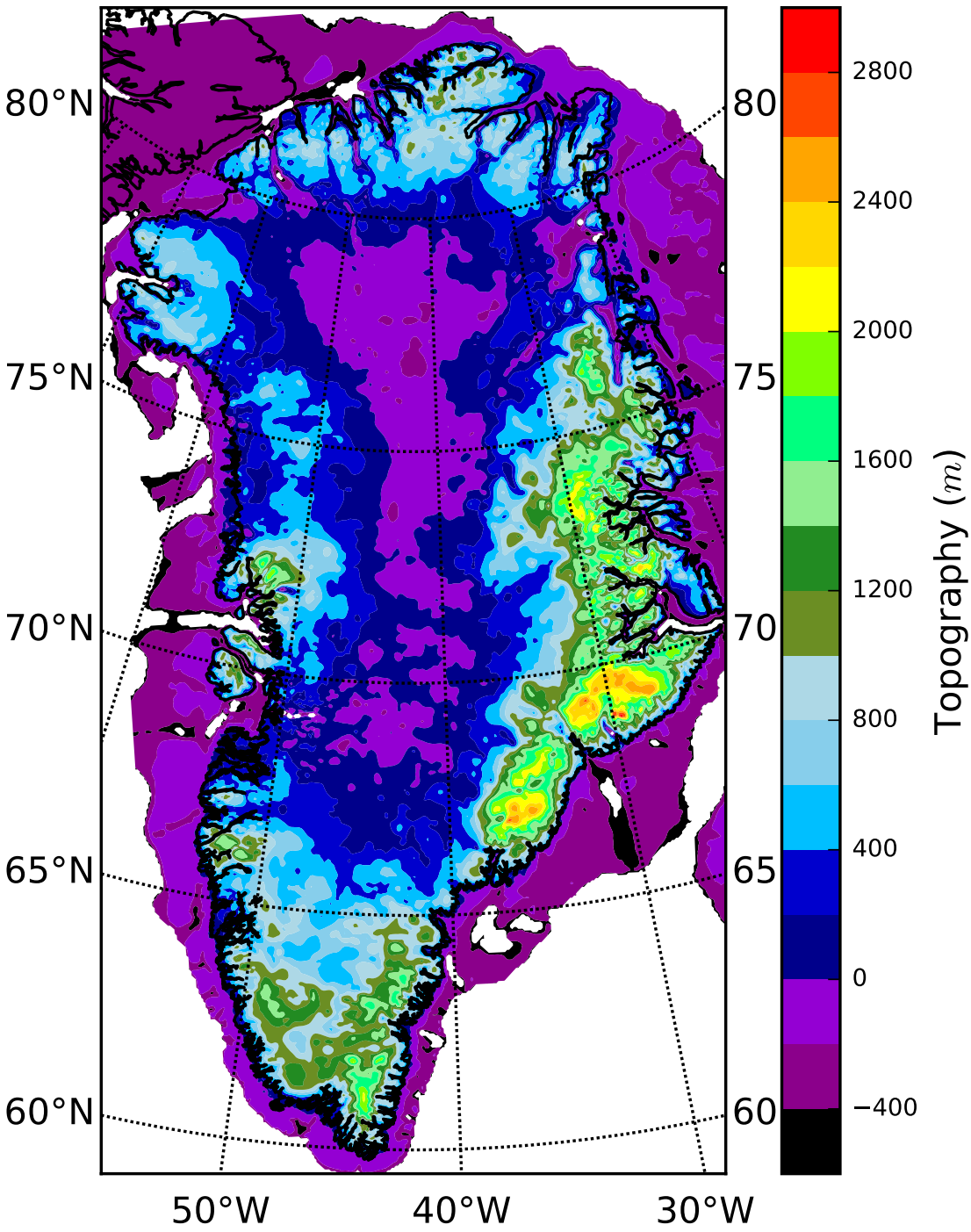

Figure 1.2: The Greenland Ice Sheet bedrock topography based on *Bamber et al.* (2013).

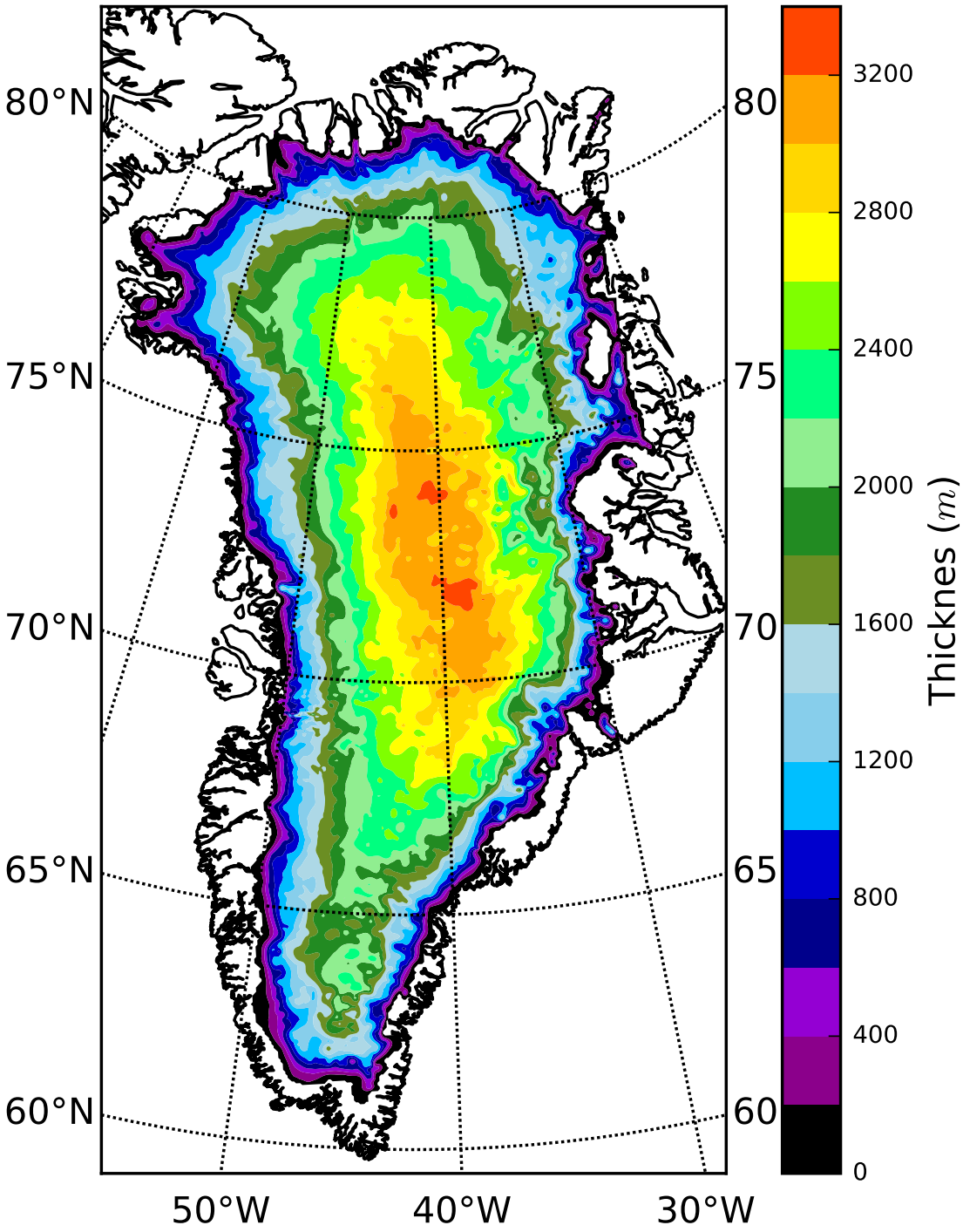

Figure 1.3: The Greenland Ice Sheets ice thickness based on *Bamber et al.* (2013).

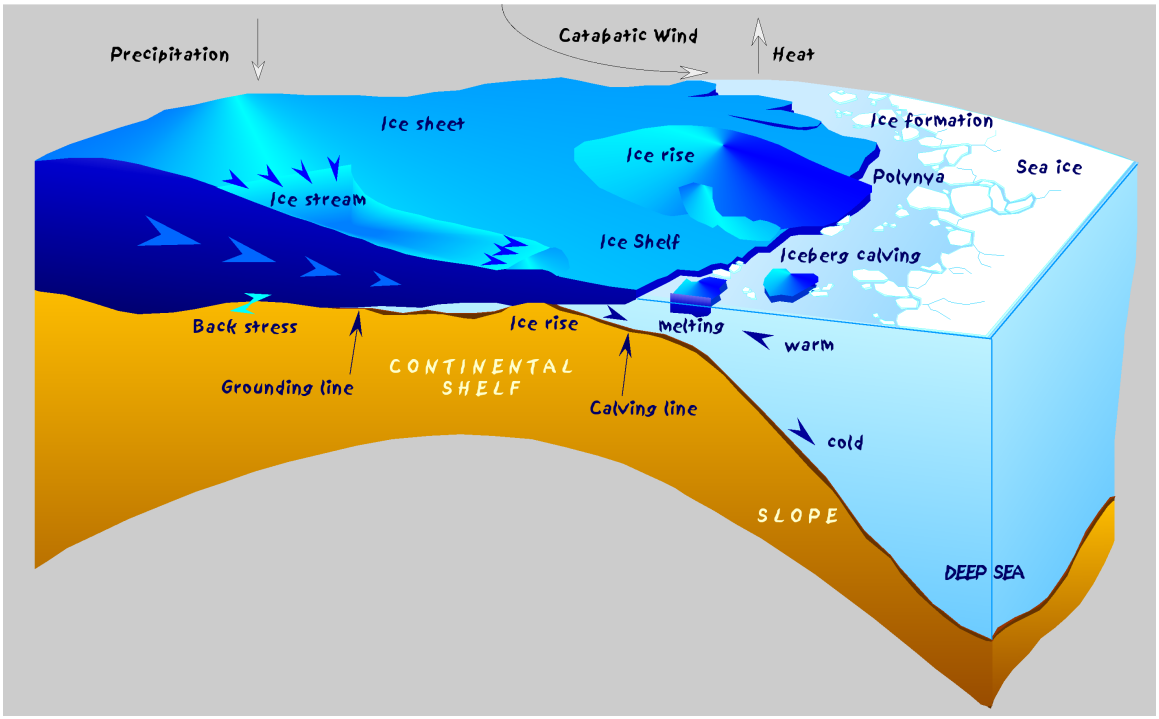

Figure 1.4: Conceptual figure of the ice sheet illustrating ice sheet dynamics, figure courtesy of wikipedia.org.

the entire continent of Greenland, along with the surrounding continental shelf, was glaciated (*Bennike and Björck*, 2002). From that time the ice sheet grew until the termination of the Little Ice Age and then gradually decreased to the present day (*Huybrechts*, 1994, 2002), with ice melting first on the southern peninsula (14 ka) and later on the northern tip (9 ka) (*Bennike and Björck*, 2002; *Håkansson et al.*, 2007).

1.3 Mass Balance of Greenland Ice Sheet

The Greenland Ice Sheet gains mass through accumulation processes (snow and rain fall) and loses mass through ablation processes including iceberg calving, submarine melting and surface meltwater runoff (*Box*, 2002; *Cuffey and Paterson*, 2010). The net result of the mass change is called the total mass balance. A negative value means Greenland loses more mass than it gains and therefore contributes to the global

sea level rise. Mass balance for the Greenland Ice Sheet is usually given in gigatons per year (Gt yr^{-1}), where one gigaton is 10^{12} kilogram.

It's important to understand the physical processes in the mass balance of Greenland ice sheet. During winter seasons, snow falls over the surface of the whole Greenland Ice Sheet and accumulates at the the high elevations and central parts, where temperatures are coldest. The fallen snow is compacted into ice through metamorphosis under the influence of pressure. The accumulated mass in the central part drives the ice sheet to move toward the marginal areas through deformation and sliding. Ice shelves can form along the edge of ice sheets. As ice flows towards the margin, it eventually fractures and break off in a process called iceberg calving (Figure 1.4). During summer time melt occurs at the ice sheet surface. Part of the meltwater percolates, refreezes and is retained in the snow pack or surface. The rest of the water runs off from the surface into the ocean either over the ice sheet surface or by draining to the bed through a moulin and then being routed subglacial towards the margin.

The largest contributor to accumulation is precipitation, including both snowfall and rain. This amounts to nearly 697 $Gt\,yr^{-1}$ for total snowfall and 46 $Gt\,yr^{-1}$ for rainfall (*Ettema et al.*, 2009). Other processes include water vapor deposition, basal freeze and snow blowed from adjacent land by wind. Ablation processes include melting, iceberg calving, and sublimation. Current estimates of accumulation, ablation, and mass balance, as well as the relevant uncertainties, are shown in Table 1.1.

Process	Mass ($Gt\,yr^{-1}$)
Net surface accumulation	228 ± 34
Ablation from ice discharge	-495 ± 29
Total	-267 ± 38

Table 1.1: Mass budget for Greenland Ice Sheet in 2007, based on data from *Rignot et al.* (2008).

The Greenland Ice Sheet has lost ice over the past two decades (*Flato et al.*, 2013;

Enderlin et al., 2014; *Khan et al.*, 2015). Research shows the high confidence that ice loss has happened in several parts of Greenland Ice Sheet and the large mass loss rates have spread to more regions based on the combination of data from satellite and airborne remote sensing as well as field data (*Flato et al.*, 2013). The mass loss rate of Greenland Ice Sheet has accelerated since 1992. The average rate has increased from 121 Gt yr^{-1} over the period 1993–2002 to 229 $Gt\,yr^{-1}$ over the period 2005–2010, and the related sea level rise is equivalent to 0.3 mm yr^{-1} and 0.6 mm yr^{-1} respectively (*Rignot et al.*, 2008; *Enderlin et al.*, 2014; *Khan et al.*, 2015). Figure 1.5 shows the contribution of Greenland Ice Sheet to sea level change and the cumulative mass loss from ice sheet (*Flato et al.*, 2013). Figure 1.6 shows the mass loss estimation from different methods and work.

The mass loss from surface melt and outlet glacier discharge contribute nearly equally to the total ice loss for Greenland Ice Sheet. Mass loss from both processes has increased in the past 20 years (*Flato et al.*, 2013). The accelerated surface mass loss is more than models predicted and has increased faster than the contribution from dynamical discharge (*Enderlin et al.*, 2014). The relative contribution of ice discharge to total loss decreased from 58% before 2005 to 32% between 2009 and 2012. As such, 84% of the increase in mass loss after 2009 was due to increased surface runoff (*Enderlin et al.*, 2014). The mass loss from Greenland Ice Sheet is one of the major contributors to sea level rise in the recent (*Cazenave*, 2006), while the surface mass loss may dominate in the future mass balance of Greenland Ice Sheet (*Enderlin et al.*, 2014).

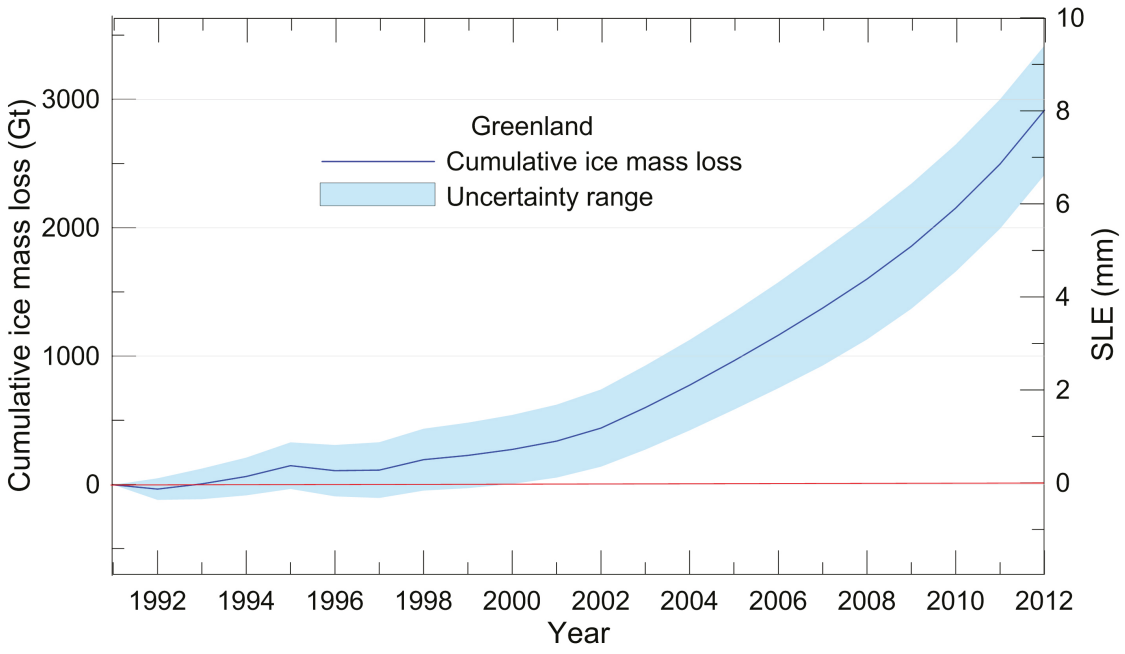

Figure 1.5: The Greenland Mass loss from the past two decades and related sea level rise *Flato et al.* (2013).

1.3.1 Surface Mass Balance

The surface mass balance (SMB) is the net sum of mass fluxes in and out of the ice sheet surface, usually defined as (*Dahl-Jensen et al.*, 2009)

$$SMB = \int (P + TMT + R + \nabla Q)\delta t \delta A \tag{1.1}$$

where A is surface area, P is precipitation, TMT is turbulent moisture transport, R is run-off and Q is the snowdrift mass flux. Ice sheet gains mass from the solid fraction (snow, hail and freezing rain) as well as from liquid rain. Ice sheets lose mass from run-off of surface water (meltwater and liquid rain), turbulent moisture transport (surface evaporation, sublimation and deposition). In addition, drifting snow can blow mass into the ocean, but this is usually negligible compared to the other terms in the total surface mass balance estimation. Not all the meltwater and

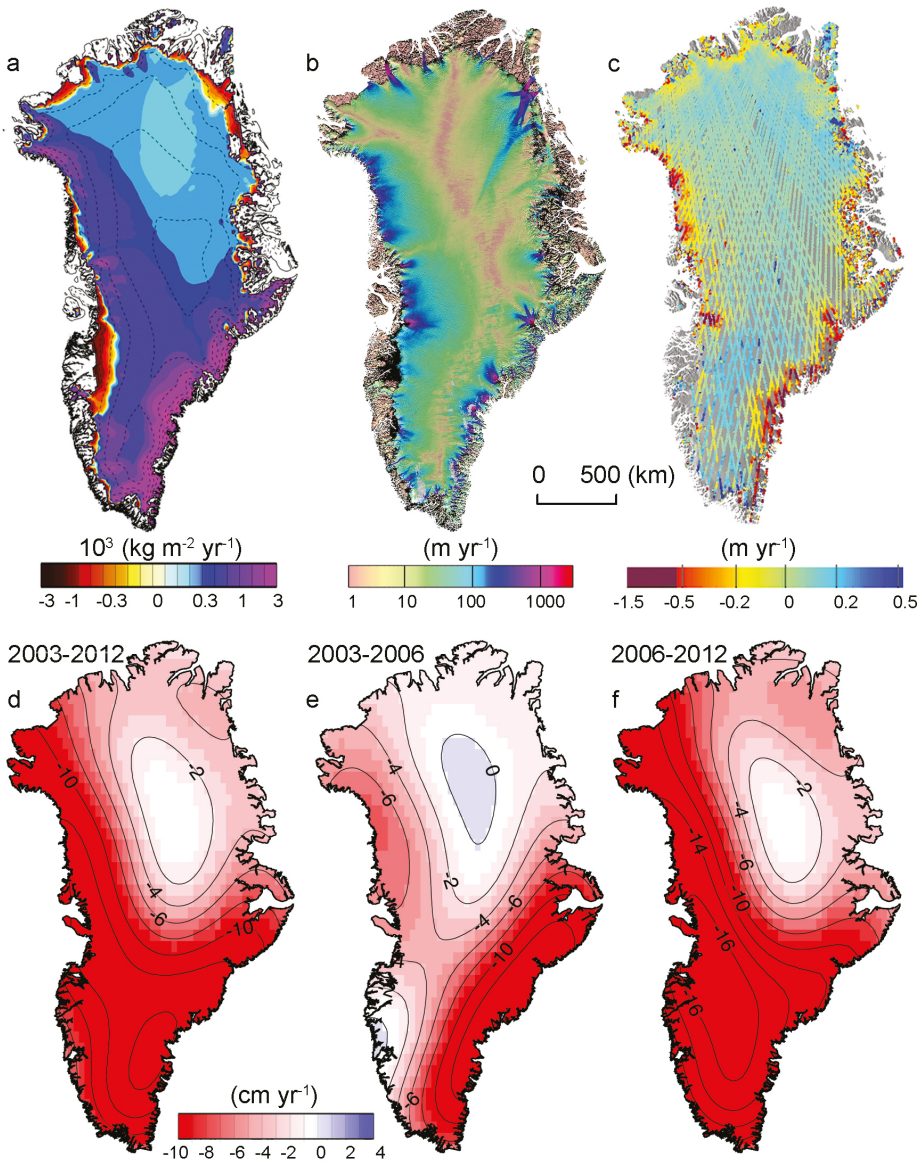

Figure 1.6: Key variable related to the determination of the Greenland ice sheet mass changes. (a) Mean surface mass balance for 1989–2004 from regional atmospheric climate modeling *Ettema et al.* (2009). (b) Ice sheet velocity for 2007–2009 determined from satellite data, showing fastest flow in red, fast flow in blue and slower flow in green and yellow *Rignot and Mouginot* (2012). (c) Changes in ice sheet surface elevation for 2003-2008 determined from ICESat altimetry, with elevation decrease in red to increase in blue *Pritchard et al.* (2009). (d, e) Temporal evolution of ice loss determined from GRACE time-variable gravity, shown in centimeters of water per year for the periods (a) 2003–2012, (b) 2003–2006 and (c) 2006–2012, color coded red (loss) to blue (gain) *Velicogna* (2009). Image compilation from *Flato et al.* (2013).

rain is run-off from the ice sheet. Part of the liquid water will penetrate into snow or firn pack, refreezes is retained there.

Regions where Surface Mass Balance (SMB) > 0 are called accumulation zones, while ablation zones are defined as regions where SMB < 0. The equilibrium line is the elevation where SMB $= 0$. Figure 1.7 shows the ice sheet surface melt and runoff processes. Part of the meltwater retained in the ice sheet (meltwater ponds or refreeze in snowpack). Other water runoff through the the crevasses or moulins down to the bottom of the ice sheet. These kind of meltwater will influence the ice sheet dynamic processes (*Zwally et al.*, 2002). The average SMB for the Greenland Ice Sheet in the past 50 years is 285 $Gt\,yr^{-1}$ with a range of 62 Gt based on three reconstructions (*Box et al.*, 2004; *Fettweis*, 2007; *Hanna et al.*, 2008). Table 1.2 shows the different components of surface mass balance from previous works.

Model	Period	P	M	R	RF	SMB
MAR^a	1958–2007	550	532	−282	250	264
$PMM5^b$	1958–2006	638	228	−213	48	326
$Hanna^c$	1958–2007	559	313	−261	77	264
$Mote^d$	1988–1999	591		−255		239
$Reeh^e$	1900s	552		−279		273

Table 1.2: Surface mass balance components for Greenland Ice Sheet based on different methods and works. P is precipitation, M is meltwater, R is run-off, RF is refreeze and SMB is the surface mass balance, with units $Gt\,yr^{-1}$. (a) MAR *Fettweis* (2007), (b) PMM5 *Box et al.* (2004), (c) *Hanna et al.* (2008), (d) *Mote* (2003), (d) *Reeh et al.* (1999); *Reeh* (1999).

1.4 Numerical Models

Numerical models have been used in the polar region research for long time and they have several advantages over other techniques. Numerical models are much cheaper to develop and use than satellite missions or even airborne experiments. Nu-

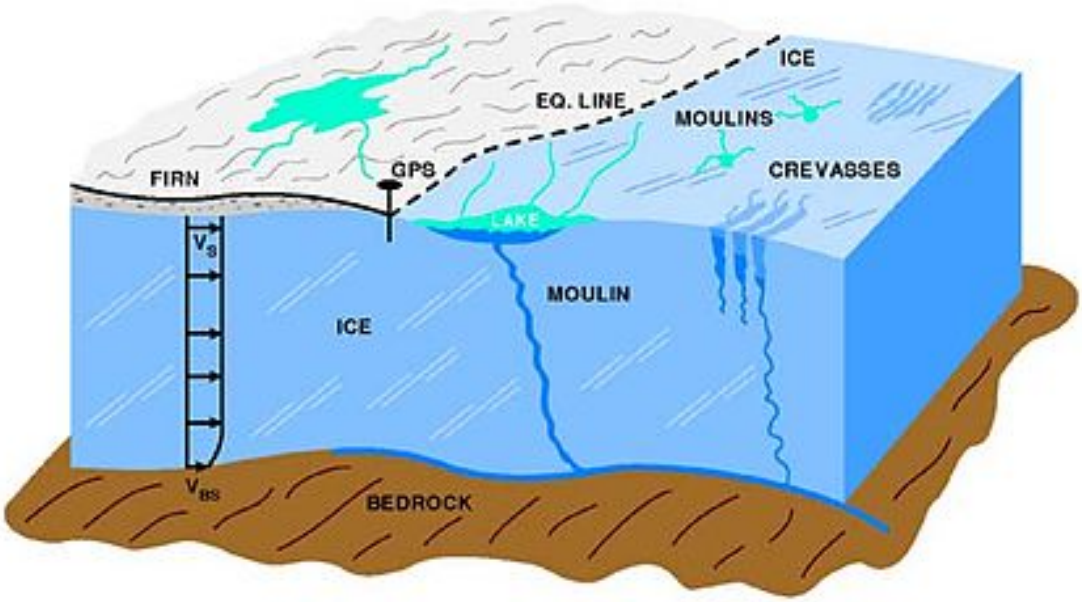

Figure 1.7: Schematic of glaciological features in the equilibrium and ablation zones, including surface lakes, inflow channels, crevasses, and moulins *Zwally et al.* (2002).

merical models can provide more details in specific areas and time periods compared with the limited measurement. Also the need for future projects forces scientists to come up with different numerical models to estimate the mass balance of the Greenland Ice Sheet. Regional climate model can provide details about the temporal evolution and relative importance of different components of the surface mass balance as well as their sensitivity to the climate and future projection. Some regional climate model are used to help technical methods. For example, regional models are often used to estimate firn corrections needed for altimetry based estimates of ice sheet mass balance.

1.4.1 Positive Degree Day

The air temperature is a well known important factor for the ice sheet melting estimation. The positive degree day or the temperature index models, are based on the assumption that the relationship between snow or ice melt and air temperature usually expressed in the form of positive temperatures sum (*Braithwaite*, 1995). Which means the melting during any time periods is proportional to the sum of all temperatures over the melting point at the same place during the same periods (*Hock*, 2003). The melt of snow or ice is described by (*Hock*, 2003) as,

$$\sum_{n=1}^{n} M = DDF \sum_{n=1}^{n} T^{+} \Delta t, \tag{1.2}$$

where M is the melt amounts during a period of n time intervals, Δt is the sum of positive air temperatures of each time interval, T^{+} is the difference between air temperature and reference temperature during the same period and the DDF is the degree day factor, with units mm d^{-1} °C. Normally, the models are applied with daily time intervals for the melt estimation, any other time intervals are also able to be used in the calculation, such as hourly or monthly intervals.

The positive degree day approach was first used by (*Finsterwalder*, 1887) in Alps glacier and then tested in Greenland conditions (*Braithwaite and Olesen*, 1984, 1989). The method was then modified by *Reeh* (1989) to estimate the melting over the whole Greenland Ice Sheet and used in ice sheet dynamics modeling by (*Huybrechts et al.*, 1991). Since the simplicity of the model and the availability of the air temperature data, the positive degree day models have been widely used in the snow and ice melt estimation (*Oerlemans et al.*, 1998; *Hanna et al.*, 2008).

The degree day factors vary considerably in different spatial and temporal regimes. Ice usually has a larger degree day factors than those for snow, due to the lower albedo of ice compared to that of snow, the values for snow and ice at different sites range from 2.5–11.6 mm d^{-1} °C and 6.6–20.0 mm d^{-1} °C, respectively based on measurements (*Hock*, 2003). There also exist diurnal and seasonal variations in the degree day factors by measurements (*Singh and Kumar*, 1996) and modeling studies (*Hock*, 1999). The diurnal variations is caused by diurnal radiation fluctuations while the seasonal variations is due to the decreases in snow albedo as the melt season progresses (*Kuusisto*, 1980).

Although the positive degree day models simplify the complex physics processes in the surface energy balance, the models often match the performance of energy balance models on a catchment scale (*Hock*, 2005; *Van den Broeke et al.*, 2010). The reason why the model work is generally attributed to the high correlation between air temperature with several important components of the energy balance equation, like the incoming long-wave radiation, the turbulent heat fluxes. These terms have a strongly dependence on the air temperature, while the temperature in turn is affected by global radiation, although not in a simple way (*Kuhn*, 1993; *Ohmura*, 2001).

The Positive Degree Day (PDD) have proven to be a powerful tool for the melt calculation, but there exists some shortcomings. The method simplifies the complex processes involved in the energy balance of ice sheet surface and atmospheric bound-

ary layer. The degree day factor itself depends on the energy balance, this make the universal factor impossible (*Braithwaite*, 1995). Although the models work well over long time periods when the temporal resolution increase the accuracy decrease. There also exists spatial variability, the degree day factor maybe different for different topographic, such as shading, slope and aspect angles, the accurately of the model may vary substantially for different locations. The uncertainty of the variations of degree day factor limits the positive degree day models performance in the future and past estimation for the melt of ice sheet.

1.4.2 PMM5

The Polar MM5 is the Fifth-generation Mesoscale Model (MM5) developed by the Polar Meteorology Group of the Byrd Polar Research Center at The Ohio State University, the Pennsylvania State University and National Center for Atmospheric Research based on a modified version of previous mesoscale modeling in polar regions (*Bromwich et al.*, 2001; *Cassano et al.*, 2001). PMM5 is the first high resolution regional climate model for Greenland Ice Sheet, it has a horizontal grid resolution of 24 km (*Box et al.*, 2004, 2009).

The PMM5 is forced with 6 hourly ERA-40 data at the boundaries for the period 1958–2002 and 12-hourly ECMWF data for the period 2002–2005 (*Box et al.*, 2006, 2009). The model was reinitialized every month (*Box et al.*, 2004).

The melting of the ice sheet is estimated through an surface energy balance model and corrected with bias based on in situ data (*Box et al.*, 2004, 2009). The melt amount is defined as (*Vernon et al.*, 2013),

$$M = \frac{Q_M t}{L_f \rho}, \tag{1.3}$$

where M is the melt amount, Q_M is the residual energy, t is the time period, ρ is the

ice density and L_f is the latent heat capacity of fusion. The Q_M is calculated in the energy balance model as,

$$Q_M = Q_N - (Q_H + Q_E + Q_G + Q_R), \tag{1.4}$$

where Q_N is the net radiative flux, Q_H and Q_E are the turbulent sensible and latent heat fluxes, respectively, Q_G is the conductive heat flux within firn and ice layers and Q_R is the sensible heat flux from rain (*Vernon et al.*, 2013).

The surface albedo of the model is applied with several satellites observational albedo product. For the period 2000–2008, the grid cell albedo was updated with MODIS MOD10A1 data product everyday (*Stroeve et al.*, 2006; *Hall et al.*, 2011). In the 1981–1999 period, the albedo is based on AVHRR product (*Key et al.*, 2002), for time prior to 1981, multi-year daily averaged MOD10A1 data are used (*Vernon et al.*, 2013). The surface water runoff is calculated with the scheme described by *Pfeffer et al.* (1991). Surface water percolates into snow or firn pack if possible, with retention and refreezing in the later processes, if the snow or firn is saturated, the surplus water will runoff downslope.

Since the Polar Fifth-generation Mesoscale Model (PMM5) model only consider single season's accumulation layer, the meltwater is unable to percolate into previous years' snow or firn pack, this may overestimate the surface water runoff of the surface mass balance.

1.4.3 RACMO 2.1

The Regional Atmosphere Climate Model (RACMO 2.1) was developed by the Royal Netherlands Meteorological Institute (*Van Meijgaard et al.*, 2008) based on the RACMO2.0 to improve model performance under present-day climate (*Lenderink et al.*, 2003). The model is forced by ERA-40 data at its boundaries every 6 hour with

an horizontal resolution about 11 km (*Ettema et al.*, 2010a,b; *Vernon et al.*, 2013).

RACMO implemented an energy balance snow metamorphism model to the atmosphere model to calculate the surface mass balance for ice sheet. In additional, the model also applied a multiple snow-layer snow scheme for the calculations on Antarctica and Greenland (*Reijmer et al.*, 2005). The melting-refreezing conditions are also considered in these processes for Greenland Ice Sheet (*Ettema et al.*, 2009).

The surface energy balance of the RACMO 2.1, as described by (*Bougamont et al.*, 2005),

$$M_E = (1-\alpha)SW_{\downarrow} + \varepsilon LW_{\downarrow} - \varepsilon\sigma T^4 + Q_H + Q_E + Q_R, \tag{1.5}$$

where M_E is the melt energy, $SW_{\downarrow}$ and $LW_{\downarrow}$ are the downward shortwave and longwave radiation fluxes, α is the surface albedo, T is the surface temperature and ε is the surface emissivity. T is also used as the boundary condition for temperature modeling through the snow/firn/ice layer.

In the model, surface albedo is a function of snow density and cloudiness. The subsurface multilayer snow model is based on the Simulation Of glacier surface Mass balance And Related Subsurface processes (SOMARS) by (*Greuell and Konzelmann*, 1994). The thermal dynamics processes are solved vertically through the column. When surface water presents, liquid water percolates downward and refreeze in the snow/firn layers. The remaining water will continue the same processes until reaches an impermeable ice layer. If there exist more water than refreeze and percolate, a slush layer will form after all pore space is filled with liquid water. The surface runoff is based on an exponential decay of water as a function of surface slop (*Greuell and Konzelmann*, 1994; *Ettema et al.*, 2009).

The Regional Atmosphere Climate Model version 2.1 (RACMO 2.1) has the highest resolution in the regional climate models and tends to capture high accumulation peaks which result in more precipitation and higher surface mass balance (*Ettema et al.*, 2009; *Vernon et al.*, 2013).

1.4.4 MAR

The Modèle Atmosphérique Régional (MAR) is a coupled atmosphere snow regional climate model especially developed for polar regions (*Fettweis et al.*, 2012). Modèle Atmosphérique Régional (MAR) was forced every 6h with ERA-40 data for 1958–2002 and with ERA-interim data after 2002 at the boundaries. The model has an horizontal resolution of 25 km, the sea surface temperatures and sea ice cover were prescribed from the ECMWF data (*Fettweis et al.*, 2005; *Fettweis*, 2007).

The atmospheric part of the model is described by (*Gallée and Schayes*, 1994) and fully coupled with the energy balance model based Soil Ice Snow Vegetation Atmosphere Transfer (SISVAT) snow model by (*De Ridder and Gallée*, 1998) to resolve the interactions between the atmosphere, sea ice, snow-covered tundra and the ice sheet surface (*Fettweis*, 2007).

The Soil Ice Snow Vegetation Atmosphere Transfer (SISVAT) snow ice model is based on the snow model CROCUS (*Brun et al.*, 1992; *Reijmer et al.*, 2012). For the surface albedo, when snow depth exceeds 10 cm, albedo depends on the shape and size of snow grains as described by CROCUS (*Vionnet et al.*, 2012), for shallow snow cover, albedo varies linearly from snow to bare ice ($\alpha = 0.45$) (*Lefebre et al.*, 2003). The snowpack model is a multilayered energy balance snow model used to estimate meltwater percolation, retention and refreezing, snow densification due to liquid refreezing and firn compaction.

MAR has not been calibrated or corrected with in situ data. Comparison of modeled water vapor flux from MAR with automatic weather station data suggests that the turbulent moisture transport is underestimated in MAR (*Fettweis*, 2007) which may influence the estimation for finall mass balance, and less meltwater compared with (*Hanna et al.*, 2008; *Dahl-Jensen et al.*, 2009).

CHAPTER II

Method

2.1 Surface Mass Balance Method

The total annual specific surface mass balance of Greenland Ice Sheet is defined by the accumulation through precipitation (snow, rain) minus surface mass runoff during a year (*Vernon et al.*, 2013):

$$SMB = M_{precip} - M_{runoff} - M_{trans} \tag{2.1}$$

where SMB is the surface mass balance, M_{precip} is the precipitation mass including snow fall and rain, M_{runoff} is the total run off mass, M_{trans} is the mass transported by turbulent moisture (evaporation, sublimation and deposition).

The runoff is defined as (*Vernon et al.*, 2013):

$$M_{runoff} = M_{water} - M_{refreeze} - M_{retention} \tag{2.2}$$

where M_{water} is the total surface water produced from melt or rain, $M_{refreeze}$ is the liquid water refreeze mass and $M_{retention}$ is the mass of water retention is the snow and firn layers. All components have the unit of millimeter water equivalent $mm\,w.e.$ while the total SMB is given by $Gt\,yr^{-1}$ after integrated over the ice sheet.

The precipitation happens over all Greenland Ice sheet, while the runoff mostly

focuses in the ablation area. Part of the surface water will refreeze during cold time (night or winter) (*Janssens and Huybrechts*, 2000), some may retent in the surface, as melt pond or surface lake (*Zwally et al.*, 2002) and later run off through supra-glacial lake drainage (*Das et al.*, 2008), or in firn layer as firn aquifer under large snow precipitation rate and warm condition (*Forster et al.*, 2014; *Koenig et al.*, 2014), the rest will runoff directly (*Das et al.*, 2008).

In our model, we get the total precipitation from input data directly, for the differential of snow or rain precipitation. If the driven data has both input, we can use the snow and rain precipitation to drive the model and estimate the mass balance. If the input data only contains precipitation flux, we will treat snow and rain differently based on the air temperature. If the air temperature larger than 2°C, we will treat the precipitation as rain, otherwise we treat it as snow. For the meltwater refreeze and water retention, we simulate and record them in the englacial model, while we calculate the meltwater production from the surface balance model. While the runoff of the meltwater and rain water is complicate in the dynamics ways and the time scale, we assume they runoff from our model using a slope based scheme. We neglect the mass change by moisture turbulent transport, since the total amount is slight compared with precipitation and runoff (*Vernon et al.*, 2013).

2.2 Model Method

Our model is based on a column mutil-layer model, which simulate all the processes on the supra-glacial and englacial part of ice sheet. The surface energy balance model computes surface energy fluxes, surface melting and runoff. It serves as the upper boundary condition for the subsurface englacial model. The subsurface englacial model estimates the heat transfer, liquid water percolation, water refreezing, retention as well as runoff in the layers. Figure 2.1 shows the surface energy processes and the relationship between this two models and Figure 2.2 shows the physical processes

simulated in the englacial model.

In the surface energy balance model, the surface energy flux is the sum of radiative flux, turbulent flux with conductive flux (*Greuell and Konzelmann*, 1994):

$$Q_n = SW_\downarrow + SW_\uparrow + LW_\downarrow + LW_\uparrow + Q_{sen} + Q_{lat} \tag{2.3}$$

where Q_n is the net surface energy flux, $SW_\downarrow$ and $SW_\uparrow$ are the incoming and reflected shortwave radiation, $LW_\downarrow$ and $LW_\uparrow$ are the incoming and outgoing longwave radiation, Q_{sen} is the sensible heat fluxes, Q_{lat} is the latent heat flux, Q_{con} is the conductive heat flux through snow layers.

$$\dot{m} = Q_n / L_f, \tag{2.4}$$

where $\dot{m}$ is the melt rate (units of kg m^{-2} s^{-1}) and L_f is the latent heat.

The model is forced by seven meteorological input, including incoming shortwave and long-wave radiation, atmospheric air temperature, wind speed, humidity, precipitation and surface pressure, the details of all model description are in the chapter 3.

2.3 Surface Energy Balance Model

2.3.1 Surface Albedo

In the surface energy balance model, the surface albedo is one of the most important physical variables. In the accumulation area, surface is mostly covered with snow or firn over the year, in the ablation zone, during the winter time when precipitation happened the surface is covered by snow or firn, while in the summer time melt will remove all snow and firn, the surface will be covered by bare ice. The surface layer type varies at different locations and seasons. For a better estimation of the surface albedo, our model use a combination of snow albedo and bare ice albedo for

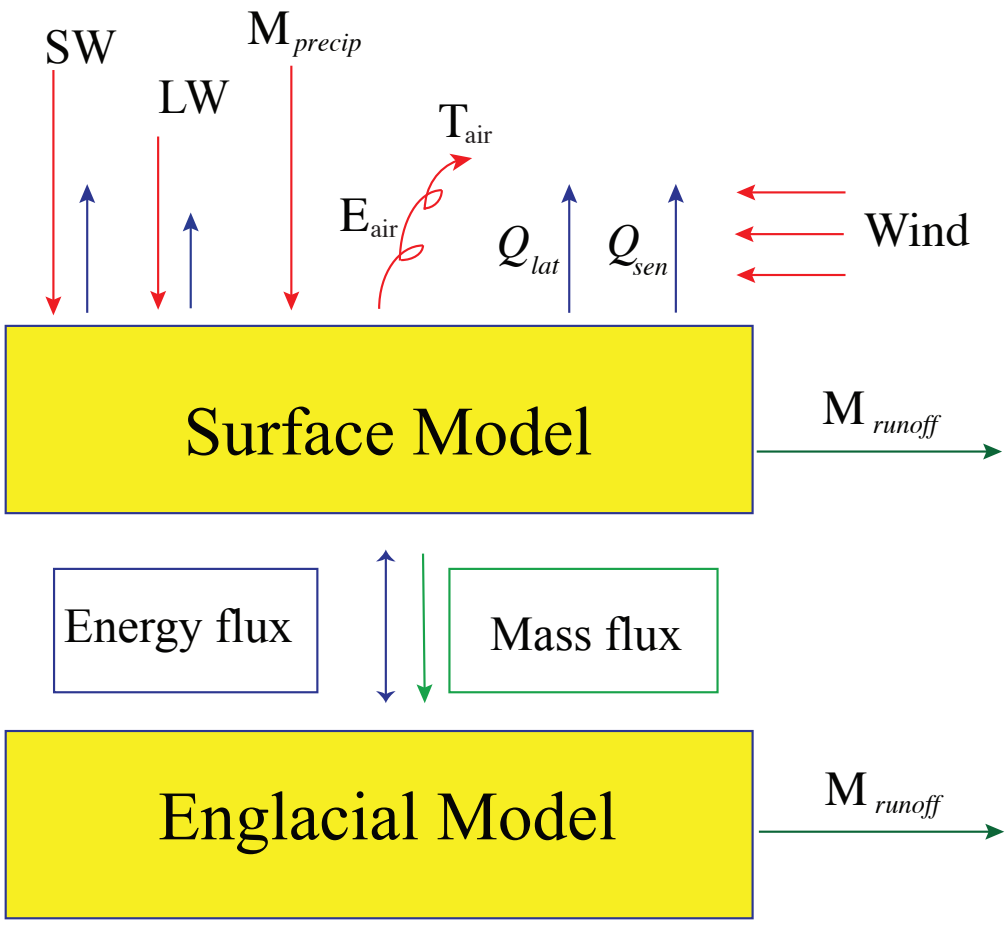

Figure 2.1: Scheme figure for energy and mass flux processes in the model.

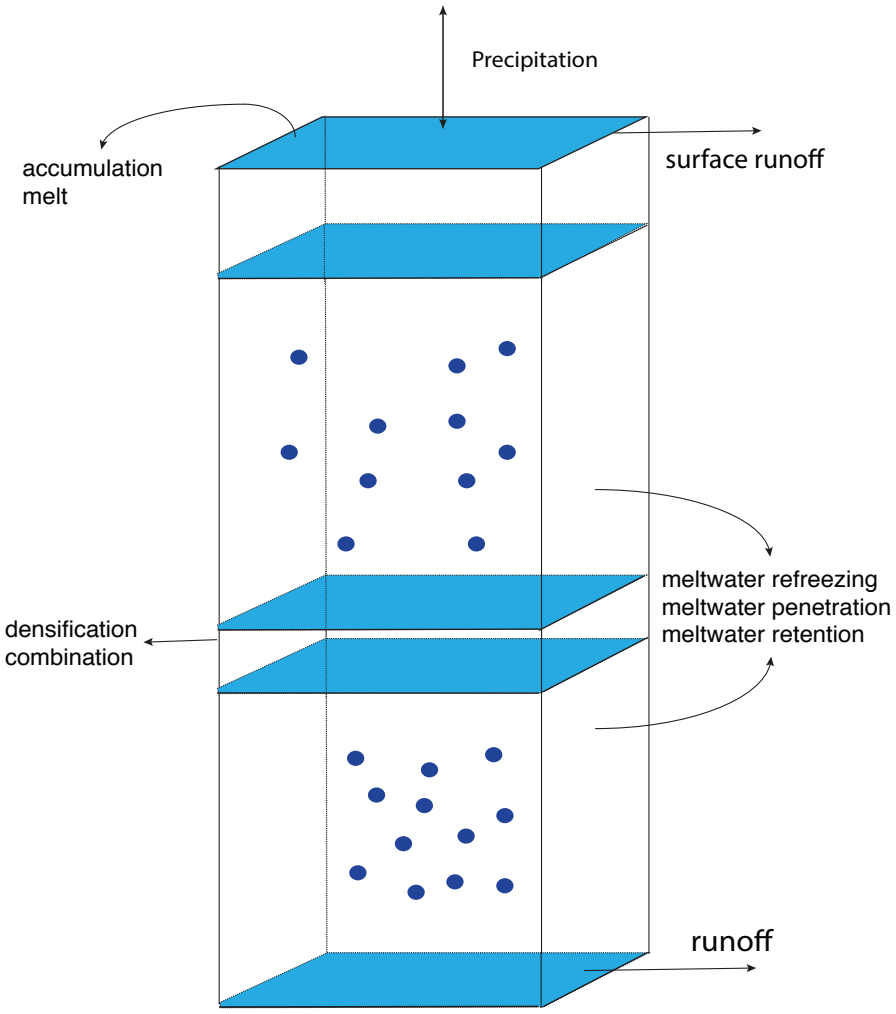

Figure 2.2: Scheme figure for the englacial model, physical processes simulated in the model.

the surface albedo simulation in the model. When surface is covered by snow or firn, we estimate the snow layer albedo with the layer snow grain size, black carbon concentration, solar zenith angle and cloud optical properties (*Gardner and Sharp*, 2010; *Flanner and Zender*, 2006). For bare ice surface, we set the background ice albedo with spatially-varying constant value from the MODIS satellite data (*Van Angelen et al.*, 2012).

2.3.1.1 Snow Albedo

For the snow albedo, the method is based on (*Gardner and Sharp*, 2010), in which the broadband albedo is calculated by snow grainsize, black carbon concentration, solar zenith angle, cloud optical thickness as

$$\alpha_s = \alpha_{\hat{s}} + \delta\alpha_c + \delta\alpha_u + \delta\alpha_\tau, \tag{2.5}$$

where α_s is the albedo for snow layer surface, $\alpha_{\hat{s}}$ is the pure snow albedo, $\delta\alpha_c$, $\delta\alpha_u$ and $\delta\alpha_\tau$ are the corrections associated with light-absorbing carbon, solar zenith angle and cloud optical thickness.

For a solar zenith angle and cloud optical depth of zero, pure snow (without light-absorbing carbon), the snow albedo is:

$$\alpha_{\hat{s}} = 1.48 - \hat{S}^{-0.07}, \tag{2.6}$$

where $\hat{S}$ is the specific surface area, range from 0.07 to 1300 $cm^2\, g^{-1}$,

The correction with light-absorbing carbon is

$$\delta\alpha_c = \max(0.04 - \alpha_{\hat{s}}, \frac{-c^{0.55}}{0.16 + 0.6\hat{S}^{0.5} + 1.8c^{0.6}\hat{S}^{-0.25}}), \tag{2.7}$$

where c is the concentration of light-absorbing carbon range from 0 to 2 $ppmv$.

$$\alpha_c = \alpha_{\hat{s}} + \delta\alpha_c, \tag{2.8}$$

The correction for solar zenith angle is

$$\delta\alpha_u = 0.53\alpha_{\hat{s}}(1 - \alpha_{\hat{c}})(1 - u)^{1.2}, \tag{2.9}$$

where u is the cosine of the solar zenith angle.

The correction for the cloud optical thickness is

$$\delta\alpha_\tau = \frac{0.1\tau\alpha_c^{1.3}}{(1 + 1.5\tau)^{\alpha_{\hat{s}}}}, \tag{2.10}$$

where τ is the optical cloud thickness range from 0 to 30.

For the specific surface area, we calculated it with the snow grain size.

$$\hat{s} = \frac{3}{\rho_i r_e}, \tag{2.11}$$

where $\rho_i \sim 917\text{kg/m}^3$ is the density of snow and r_e is the layer grain size.

Snow and firn grainsize ages with the time through dry grow and wet grow, the net change in grain size in snow layer is a summation of changes caused by dry snow metamorphism, liquid water-induced metamorphism, refreezing of liquid water, and addition of freshly-fallen snow (*Oleson et al.*, 2010). As the grainsize increases, surface layer albedo will decrease, while the snow precipitation brings fresh snow with small grainsize to refresh the layer. The snow grainsize is calculated by (*Flanner and Zender*, 2006; *Oleson et al.*, 2010):

$$r_e(t) = [r_e(t-1) + dr_{e,dry} + dr_{e,wet}]f_{old} + r_{e,0}f_{new} + r_{e,rfz}f_{rfrz}, \tag{2.12}$$

where f_{old}, f_{new} and f_{rfrz} are the snow layer mass fraction of snow carrying from the

previous time step, freshly-fallen snow, and refrozen liquid water, respectively.

Dry snow aging is based on microphysical model by (*Flanner and Zender*, 2006), as

$$\frac{dr_{e,dry}}{dt} = (\frac{dr_e}{dt})_0 (\frac{\eta}{(r_e - r_{e,0}) + \eta})^{1/\kappa}, \tag{2.13}$$

where$(\frac{dr_e}{dt})_0$, η and κ are retrieved interactively from a lookup table with snow temperature, temperature gradient and density.

The contribution of liquid water to enhanced metamorphism is based on parametric equations published by (*Brun et al.*, 1989), the grain growth rates under different liquid water content fraction is

$$\frac{dr_e}{dt} = \frac{10^{18} C_1 f_{liq}^3}{4\pi r_e^2}, \tag{2.14}$$

where f_{liq} is the liquid water content, C_1 is constant as 4.22×10^{-13}.

2.3.1.2 Ice Albedo

The albedo of bare ice in the ablation zone of Greenland Ice Sheet varies over space and time (*Tedesco et al.*, 2013; *Box et al.*, 2012). In the southwestern region of Greenland, the albedo values could smaller than 0.4 *Wientjes et al.* (2011), some even could be called as " dark snow ", while for the present of snow over the year, it could be as high as 0.6. We set the bare ice albedo as constant for a specific location, while different location may have different values (*Bøggild et al.*, 2010). We take the scheme from (*Van Angelen et al.*, 2012), use lower value from MODIS satellite data to represent the bare ice albedo during the summer time, take the mean value for data record for bare ice constants.

$$\alpha_i = \alpha_{bare} \tag{2.15}$$

where α_i is the background ice albedo for surface covered by bare ice, α_{bare} is bare ice albedo.

Surface layer type is essential in the estimation the surface layer albedo, we use the surface layer thickness and bottom layer density to determine which strategy of albedo will apply on the surface layer albedo calculation. When the surface snow layer melt out all snow or firn and the bottom layer density reaches threshold density we set the surface as bare ice, while fresh snow will create a new snow layer at the surface in the winter, in which we apply snow albedo scheme.

2.3.2 Emissivity

In the surface energy balance model, we estimate the outgoing longwave radiation with the Stefan–Boltzmann method as (*Hock*, 2005),

$$LW_{\uparrow} = \varepsilon \sigma {T_s}^4, \tag{2.16}$$

where ε is the surface emissivity coefficient for longwave radiation and σ is Stefan-Boltzmann's constant. For the emissivity coefficient, it usually ranges from 0.95 to 1 for snow or ice over longwave part. In the model we use automatic weather station data calibrated and validated the emissivity for the surface energy balance model, Figure 2.3 show the root mean square of daily mean surface temperate difference between model and observational data over different emissivity coefficient with the other parameters calibrated. The smallest error is when the $\varepsilon = 1$, which means a black body assumption is best for the model, as least over ablation zone over Greenland Ice Sheet.

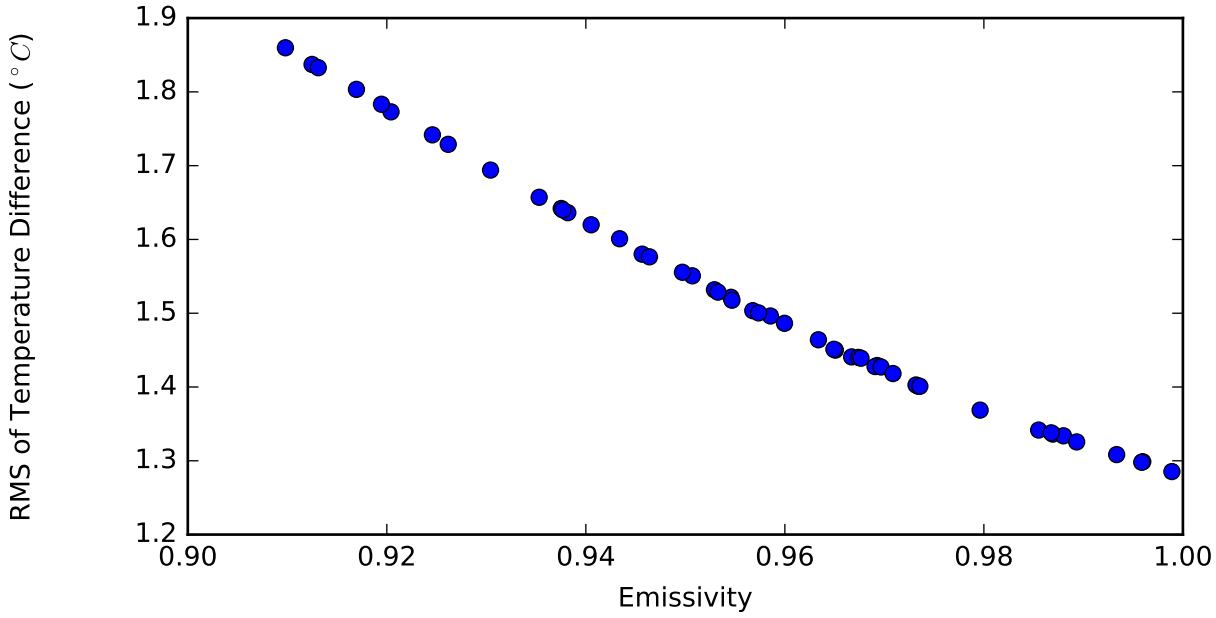

Figure 2.3: Emissivity calibration for the model with automatic weather station data at KAN_U.

2.3.3 Wind Speed

The wind speed at different input data may vary, usually wind speed are provide at East-West and South-North two vertical directions, as U_{as} and V_{as}. For the wind speed we used in the model simulation, we just need the total wind speed as,

$$U_a = (U_{as}^2 + V_{as}^2)^{1/2} \tag{2.17}$$

When the given wind speed are not at the same heigh as the input air temperature. We need take a wind speed adjustment based on wind speed power law to put these two variable at same heigh for the turbulent heat flux calculation. In general, wind speed in the surface layer exhibits a nearly logarithmic profile, as approximated by (*Wallace and Hobbs*, 2006)

$$U_z = \frac{U_r}{k_v} \ln \frac{Z}{Z_r} \tag{2.18}$$

where U_z is the wind speed at height Z, U_r is the wind speed at Z_r, Z_r is the aerodynamic roughness length and k_v is the von Karman constant. So wind speed from two different height Z_a and Z_b can be transferred as

$$U_a = U_b[\ln(Z_a) - \ln(Z_r)]/[\ln(Z_b) - \ln(Z_r)] \tag{2.19}$$

The roughness length is defined as the height of zero wind speed as extrapolated down logarithmically from the stronger winds in the surface layer. With the adjustment for the wind speed, the turbulent calculation will be at same height, we tend to use 2 meter air temperate.

2.3.4 Humidity

In the model, we take the relative humidity as the standard input, but some data set (AWS, reanalysis and CMIP5 data) provide specific humidity or even air dew point temperature instead. In the case, model will calculate the humidity based on input type. For the specific humidity and relative humidity, they are defined as (*Yau and Rogers*, 1996):

$$q = \varepsilon_v \frac{e}{P} \tag{2.20}$$

$$f = \frac{e}{e_s} \tag{2.21}$$

where q is the specific humidity, while f is the relative humidity, ε_v is constant as 0.622, e is the water vapor pressure, e_s is saturation water vapor pressure and P is the atmosphere pressure. For the surface vapor pressure, we use (*Yau and Rogers*, 1996)

$$e_s(T) = 6.112 \exp(\frac{17.67\,T}{T + 243.5}) \tag{2.22}$$

where e_s is the saturation water vapor pressure in mb and T is the temperature in degrees C. So the relationship between relative humidity and specific humidity is:

$$f = \frac{\varepsilon_v P}{q e_s} \tag{2.23}$$

2.4 Subsurface Englacial Model

The subsurface model takes the surface energy balance model as a boundary condition and computes the thermal dynamics processes within a column of snow or ice along with layer evolution like, densification, refreeze of liquid water and formation superimposed ice within the column. The englacial model also simulates the surface water percolation, refreeze, runoff and retention, as showed in the Figure 2.2, the details of the model description are in Chap2.

2.4.1 Uneven Grid Method

In the model layer setting, we apply uneven space grid method to reduce numerical calculation and keep the accuracy by put more layers near the surface and less at the bottom. Since in the ice sheet thermal processes, the surface layers are more sensitive than the bottom part, since the whole ice sheet can be taken as a refrigerator. In the englacial model we are always trying to solve the thermodynamic problem as

$$\frac{\partial T}{\partial t} = \alpha \frac{\partial^2 T}{\partial x^2}, \tag{2.24}$$

Where T is the layer temperature, α is the represent of thermal conductivity, density and related variable for simple. For the left term, we have

$$\frac{\partial T}{\partial t} = \frac{T_i^{j+1} - T_i^j}{\delta t}, \tag{2.25}$$

for the right term under the uneven space layer setting, we have

$$T(x-\delta x_1) = T(x) - \delta x_1 \frac{\partial T}{\partial x} + \frac{1}{2}\delta x_1^2 \frac{\partial^2 T}{\partial x^2} - \frac{1}{6}\delta x_1^3 \frac{\partial^3 T}{\partial x^3} + O(\delta x_1^4), \tag{2.26}$$

$$T(x+\delta x_2) = T(x) + \delta x_2 \frac{\partial T}{\partial x} + \frac{1}{2}\delta x_2^2 \frac{\partial^2 T}{\partial x^2} + \frac{1}{6}\delta x_2^3 \frac{\partial^3 T}{\partial x^3} + O(\delta x_2^4), \tag{2.27}$$

use δx_1 mutiple equation 2.26 and δx_2 mutiple equation 2.27, we have:

$$\delta x_2 T(x-\delta x_1) + \delta x_1 T(x+\delta x_2) = (\delta x_1 + \delta x_2)T(x) + (\delta x_1 + \delta x_2)\delta x_1 \delta x_2 \frac{\partial^2 T}{\partial x^2} + O(\delta x^4), \tag{2.28}$$

$$\frac{\partial^2 T}{\partial x^2} = \frac{(\delta x_2 T(x-\delta x_1) + \delta x_1 T(x+\delta x_2) - (\delta x_1 + \delta x_2)T(x))}{(\delta x_1 + \delta x_2)\delta x_1 \delta x_2} - O(\delta x^2). \tag{2.29}$$

So, for uneven spaced layer, we can solve the thermal dynamics equation as,

$$\frac{T_i^{j+1} - T_i^j}{\delta t} = \frac{(\delta x_2 T_{i-1}^j + \delta x_1 T_{i+1}^j - (\delta x_1 + \delta x_2)T_i^j)}{(\delta x_1 + \delta x_2)\delta x_1 \delta x_2}. \tag{2.30}$$

With the equation, we are able to solve the uneven space numerical thermodynamic equation for the englacial model. In the model, the layer setting can be adjust based on case requirement, the minimum layer thickness will be related to the thermal conductivity and layer density. The default setting for the model is set the top layer about 10 cm and bottom layer thickness as 1 m.

2.4.2 Enthalpy Method

We apply enthalpy method (*Anderson*, 1976) to avoid the calculation of meltwater percolation from upper layers and refreeze in the thermodynamic of englacial model layer to simplify the treatment of mixed phases. The specific enthalpy H is defined as (*Moran et al.*, 2010):

$$H = u + p/\rho, \tag{2.31}$$

where u is the internal energy and p/ρ represent the energy caused by the volume change. If heat transfer occurs under constant pressure, there is no volume change and we can neglect the second term in Equation (2.31) and the enthalpy becomes (*Aschwanden et al.*, 2012).

$$H = U \tag{2.32}$$

For cold ice layer, the specific enthalpy is defined as:

$$H_i = \int_{T_0}^{T} C_p dT^* \tag{2.33}$$

Where T_0 is the reference temperature,C_p is the hear capacity of ice. For temperate ice which reach melt point with no meltwater, the specific enthalpy is:

$$H_s = \int_{T_0}^{T_m} C_p dT^* \tag{2.34}$$

Where T_m is the melting point temperate of ice or snow. For the specific enthalpy of liquid water, if the layer ice all melt into water, the specific enthalpy is:

$$H_w = \int_{T_0}^{T_m} C_p dT^* + L_f \tag{2.35}$$

Where L_f is the fusion latent heat.

So for a mixture layer with ice and meltwater water, the specific enthalpy becomes:

$$H = \begin{cases} \int_{T_0}^{T} C_p dT^* & T < T_m, \\ \int_{T_0}^{T_m} C_p dT^* + \omega L_f & T = T_m. \end{cases} \tag{2.36}$$

Where C_p is the heat capacity (we take it as constant), ω is the water fraction in the layer and L_f is the latent heat of fusion. When we have the layer specific enthalpy, we can retrieve layer temperature and water fraction with (*Aschwanden et al.*, 2012):

$$T = \begin{cases} T_i & H < H_s, \\ T_m & H \geq H_s. \end{cases} \tag{2.37}$$

Where H_s is the specific enthalpy for layer reach melt point, T_i is the temperature calculate from ice enthalpy.

$$\omega = \begin{cases} 0 & H < H_s, \\ (H - H_s)L_f^{-1} & H \geq H_s. \end{cases} \tag{2.38}$$

Since the enthalpy is just function of the layer temperatures and liquid water content, we can retrieve the temperature and liquid water from the enthalpy and *vice versa*. If we set the T_0 as the T_m, we even don't need to calculate H_s. When we solve the thermodynamic equation of englacial model layers, we get specific enthalpy for the layer first from layer temperature and water content, solve the thermodynamic equation and get the new specific enthalpy, then retrieve the new layer temperature and liquid water. The advantage of the enthalpy method is that it we do not need to solve the phase transitions in snow and ice (i.e. the Stefan problem) associated with the moving melt and refreezing boundary within a layer.

2.4.3 Meltwater Runoff

Part of the surface water from melt or rain fall will percolate in the snow or firn layers and then may refreeze there when the layer temperature does not exceed the melting point and space is available (*Pfeffer et al.*, 1991). The irreducible water saturation of the layer is a function of layer firn density as described in 3.31 by (*Coleou and Lesaffre*, 1998), if the water content of a given layer exceeding the maximum capacity, liquid water percolates downward, until an impermeable layer is reached (*Hirashima et al.*, 2010). while part of the free water runs off immediately from the surface or inside the snowpack. The rest fills up all the pores to form a slush layer, which can later on refreeze as superimposed ice. For a column site, the surface water evolution equation is (*Zuo and Oerlkmans*, 1996):

$$\frac{dW_r}{dt} = -\frac{W_r}{t_{runoff}} + Q_{in} + Q_{out} \tag{2.39}$$

where W_r is the surface water from melt or rain, Q_{in} is the liquid water flux coming to the site from rain or melt, Q_{out} is the liquid water out from the site through penetration into snow or firn layers. So the first term in the right side is the melt water runoff at each time step.

We use runoff method based on slope of surface and a timescale t_{runoff} to estimate the water runoff as (*Lefebre et al.*, 2003; *Bougamont et al.*, 2005):

$$t_{runoff} = c_1 + c_2 \exp^{-c_3 S} \tag{2.40}$$

where S is the slope in radians and $c_1 = 0.05$, $c_2 = 15$ and $c_3 = 142$ (*Bougamont et al.*, 2005). The values used in this study are such that surficial water runs off in about 1.2 days if the slope equals one degree, while 15 days would be required on a flat surface. If the surface has an infinitely slope, the surface water would run

off immediately. The runoff time scale in the snow layers and surface may varies at different location (*Lefebre et al.*, 2003), we set them at the same speed for simple.

2.5 Surface Elevation Class Method

For Greenland Ice Sheet surface mass balance estimation, the surface elevation has influence on the result when we applied lapse rate correction in the input data. In the Figure 2.4, we show surface elevation difference in every ERA-interim data footprint box ($0.75^\circ \times 0.75^\circ$) based a high resolution digital elevation model (150m $\times$150m) (*Ekholm and Krabill*, 2001). As we can see, for Greenland Ice Sheet, the coastal part exists a difference about 1000m in surface elevation in a single ERA-interim footprint cell, although the difference is small in the inner land. In the southeastern part, the difference could reach 3000m. The atmosphere air temperature lapse rate over Greenland is about $-6\,K\,km^{-1}$, the 3000m difference means 18 degree in the air temperature which has a huge difference in the meltwater production. Since mostly surface meltwater and runoff happens in the coastal part of the ice sheet, this huge difference should be considered.

To better estimate the mass balance, we apply a method, called by elevation bin class method, in which we summary the digital elevation models point in every original input data footprint cell and divide them into several surface elevation range, as we show in Figure 2.4. We then downscale the climate forcing with nearest neighbor interpolation method and lapse rate correction for the temperature, humidity (if get from dew temperature) and pressure based on every bin elevation. After that, the model is driven by the new bin class elevation data, to estimate the energy and mass balance. For each bin class the new elevation is the mean of all point in it, the total surface meltwater production is the area based sum of all bin classes.

$$M_{footprint} = \sum M_i f_i \tag{2.41}$$

$$f_i = \frac{N_i}{\sum N_j} \tag{2.42}$$

Where $M_{footprint}$ is the total meltwater for every footprint, M_i is the melt for every bin class and f_i is the bin class total area fraction, N_i is the DEM points in each bin elevation class.

In this way, we get a high resolution and better input and output result for the estimation for the surface mass balance.

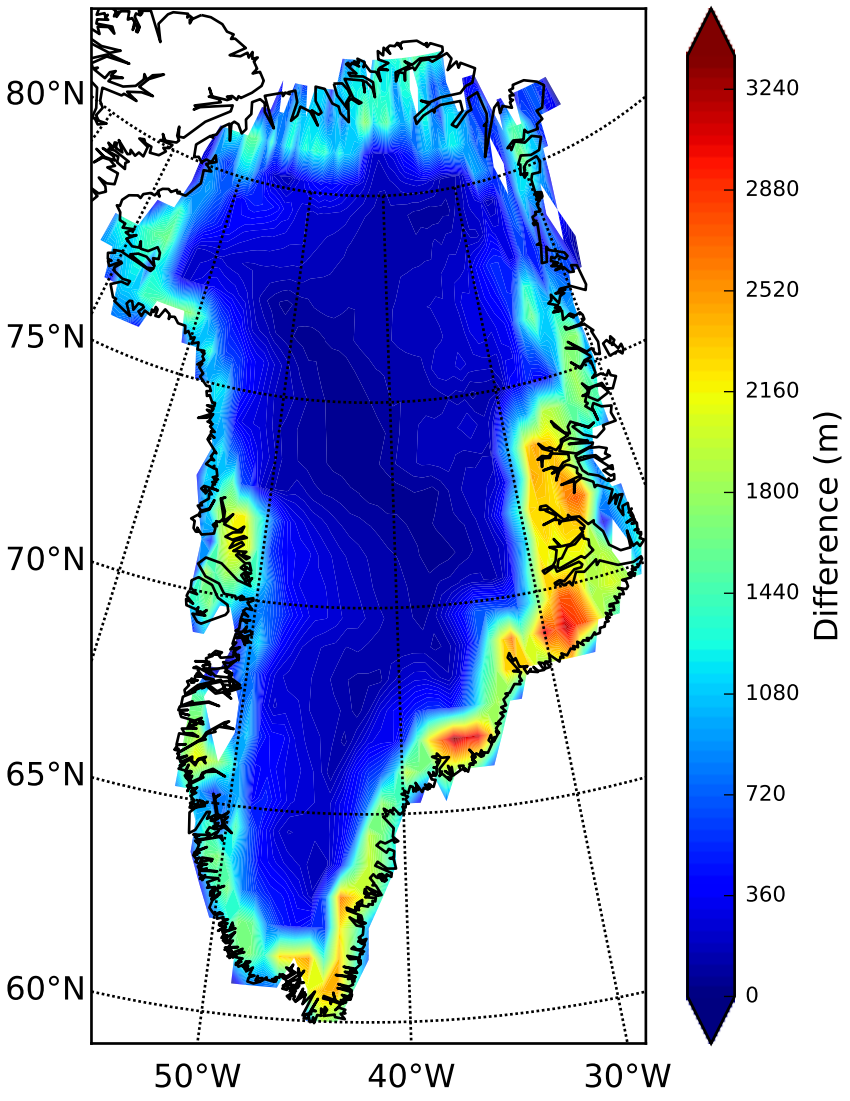

Figure 2.4: Surface elevation difference in ERA-interim footprint (150m × 150m) from DEM *Ekholm and Krabill* (2001) data.

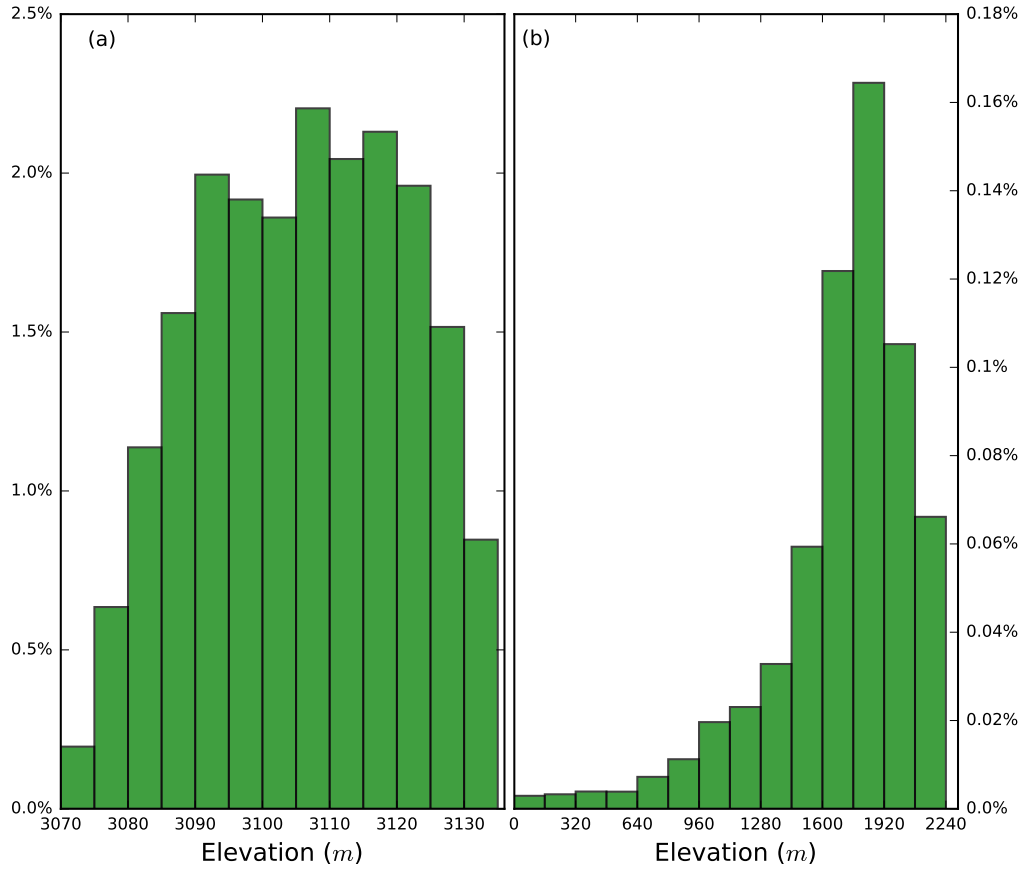

Figure 2.5: Surface elevation hist figure at flatten and high gradient footprint, panel (a) show flatten footprint at (70°N, 40°W), panel (b) with high difference at (69°N, 29°W).

CHAPTER III

A coupled energy and surface mass balance model for the Greenland Ice Sheet

3.1 Abstract

Ice sheet models often rely on empirical positive degree day schemes to compute surface melting. These schemes have often been based on input from large-scale models or adjustments to present climatology. More recently, full featured regional models have been used to dynamically downscale climate forcing to provide more physically motivated projections of ice sheet mass balance. However, dynamic downscaling remains computationally expensive and multi-century and longer simulations needed to understand past and future ice sheet changes remain problematic. In this study we present an intermediate complexity, distributed surface energy balance model coupled with a multi-layer, englacial model and use it to evaluate the impact of statistical downscaling global climate forcing on estimates of surface melt production. We first calibrated and validated our model with automatic weather station data from the PROMICE network. We then examined how model performance degraded when the model was instead driven by ERA-interim reanalysis downscaled using a suite of interpolation schemes. We find that nearest neighbor interpolation with a lapse-rate correction is adequate to reproduce large-scale trends and magnitudes of ice sheet

melt production. Furthermore, although statistical downscaling only alters our integrated estimates of total melt production over Greenland by 2%, downscaling can adjust local patterns of melt production by as much as 10–25%. Regional models may provide the best short term estimates of ice sheet surface processes, but statistical downscaling becomes increasingly promising over longer time scales when climate forcing is uncertain.

3.2 Introduction

The Greenland Ice Sheet plays a critical role in global climate not only because of its large area with high albedo, but also because it contains a vast reservoir of frozen freshwater with the potential to raise global sea level as much as 7.3 m (*Ekholm and Krabill*, 2001). Moreover, the Greenland Ice Sheet has been one of the largest contributors to recent global sea level rise, accounting for 0.5 out of a total of 3.2 mm yr^{-1} observed over the past decade (*Cazenave and Remy*, 2011; *Jacob et al.*, 2012; *Barletta et al.*, 2013; *Groh et al.*, 2014; *Shepherd et al.*, 2012; *Helm et al.*, 2014; *Khan et al.*, 2014; *Andersen et al.*, 2015). If this situation continues, the Greenland Ice Sheet alone could contribute as much as 9 cm of sea level rise by 2050 (*Shepherd et al.*, 2012; *Church and White*, 2006). However, significant uncertainties remain in projecting Greenland's role in sea level rise in the coming centuries.

The fate of the Greenland Ice Sheet is intimately tied to its mass balance, which is controlled by the discharge of ice into the ocean and the surface mass balance (e.g., *Howat and Eddy*, 2011; *Van den Broeke et al.*, 2009). (Basal melting is small, except near the few remaining ice tongues where it can be locally important (e.g., *Fahnestock et al.*, 2001; *Buchardt and Dahl-Jensen*, 2007).) Surface mass balance (SMB) is determined by the difference between accumulation (from precipitation) and mass loss from ablation (sublimation, drifting snow erosion and runoff). When the surface temperature is warm, snow and ice melt. Part of the meltwater produced

at the surface refreezes, either in the snowpack or in the firn (*Robinson et al.*, 2012). Water that doesn't freeze can be transported off of the ice sheet by running off the surface or by draining to the bed (*Harper et al.*, 2012), with both mechanisms of transport off the bed called runoff.

Numerical models are able to simulate the surface mass balance of the ice sheet and have been useful in improving our understanding of the temporal evolution and spatial distribution of the surface mass balance of ice sheets in greater detail than scarce observational data alone (e.g., *Greuell*, 1992; *Hock*, 1999; *Box et al.*, 2009; *Ettema et al.*, 2010a; *Reijmer et al.*, 2012). Additionally, mass balance models have been used to project how glacial mass balance is likely to change with climate change (e.g., *Hock et al.*, 2007; *Fettweis*, 2007; *Marco Tedesco and Alexander*, 2013). Currently, there are a variety of methods used to project future surface mass balance. For example, it is possible to statistically downscale relatively coarse reanalysis products or climate model output to estimate surface melt (*Hanna et al.*, 2001, 2008; *Gregory and Huybrechts*, 2006). The advantage of this method is that it relies on relatively few model inputs and is relatively straightforward to incorporate in large-scale ice dynamics models. At present almost all continental scale ice sheet models used for century to millennial scale projections rely on some type of empirical relationship, like the popular positive degree day (PDD) scheme to account for surface melting (*Hanna et al.*, 2008). However, this method relies on empirical relationships valid for today's climate that may fail when applied to future (or past) climate states. This is especially true when considering darkening of the ice associated with increased black carbon deposition (*Wientjes and Oerlemans*, 2010; *Dumont et al.*, 2014; *Tedesco et al.*, 2016) and changes in long wave radiation associated with changes in cloudiness (*Bennartz et al.*, 2013; *Van Tricht et al.*, 2016)

Alternatively, it is possible to dynamically downscale reanalysis data or climate model output using regional models (e.g., *Fettweis*, 2007; *Van Meijgaard et al.*, 2008;

Vernon et al., 2013; *Van Wessem et al.*, 2014). Regional models use climate or reanalysis data as boundary conditions to drive full featured regional atmospheric models that satisfy appropriate conservation laws combined with detailed process level models of ice surface processes. Although complications remain, the current generation of regional models matches the observational record remarkably well (e.g., *Fettweis*, 2007; *Lenaerts et al.*, 2012). These models, however, are computationally expensive to run making it difficult to perform century much less millennial time scale (or longer) simulations. Similar computational limitations bedevil attempts to drive regional models with a large number of climate model forcing, like those from the Climate Model Inter-comparison Project (CMIP) archive. Surprisingly, regional models and statistical downscaling methods predict similar surface mass balance trends with the largest differences associated, paradoxically enough, with the ice mask used by the model (*Vernon et al.*, 2013). Moreover, despite large-scale agreement, these models also predict markedly different regional patterns of ablation, suggesting that processes in the ablation zone, more than downscaling techniques, might control uncertainty in surface mass balance estimates (*Vernon et al.*, 2013).

Increasingly high resolution global climate models provide the necessary physics to drive ice sheet surface process models, but typically require downscaling (statistical or dynamical) to obtain the desired resolution for operational use in ice sheet models. Recent studies have, for example, shown promise that surface mass balance of ice sheets can be estimated by statistically downscaling input from global climate models (*Lenaerts et al.*, 2016). These models, however, rely on relatively simple snow-firn-ice models that are currently limited to 5 snow layers. In contrast, state-of-the-art snow models can contain hundreds of layers in an effort to simulate the detailed metamorphic processes that occur on seasonal and shorter time scales (*Jordan*, 1991; *Douville et al.*, 1995).

Here we seek to bridge the gap between the efficiency of empirical, statistical

downscaling techniques and more physically based dynamical downscaling by developing an intermediate complexity surface energy balance and englacial model that can be driven by a suite of inputs, including automatic weather stations, regional models or larger scale climate data. The model is designed to be detailed enough that it can resolve important processes, but simple enough to be incorporated in continental scale ice sheet models for century to millennial scale predictions. Our energy balance and englacial model is similar to models previously proposed (*Greuell*, 1992; *Bougamont et al.*, 2005), but focuses more quantitatively on estimates and projections of the surface mass balance. After first calibrating and validating the model against a suite of automatic weather stations, we examine how model performance degrades when the model is driven by lower resolution reanalysis data.

3.3 Model Physics

The model we present is a column surface energy balance model with a mutillayer subsurface model designed to estimate the energy and mass balance over an ice sheet surface. The surface energy balance model computes surface energy fluxes, surface melting and serves as the upper boundary condition for the subsurface model. The subsurface model estimates the heat transfer, liquid water percolation as well as water refreezing and retention in the layers. The two models are similar to models previously described in the literature (*Brun et al.*, 1992; *Gallée and Schayes*, 1994; *Van Meijgaard et al.*, 2008). However, due to the large number of processes and parameterizations involved and because it is often difficult to decipher the precise set of parameters used in existing and continuously evolving models, we provide a complete specification of the model and parameterizations below.

3.3.1 Surface Energy Balance Model

The surface energy balance model estimates radiative, convective and conductive fluxes at the surface to solve the local energy balance. The energy balance equation at the surface can be written (*Greuell and Konzelmann*, 1994):

$$Q_n = SW_\downarrow + SW_\uparrow + LW_\downarrow + LW_\uparrow + Q_{sen} + Q_{lat} + Q_{con}, \tag{3.1}$$

where Q_n is the net energy flux available for surface melting, $SW_\downarrow$ and $SW_\uparrow$ are the incoming and reflected shortwave radiation, $LW_\downarrow$ and $LW_\uparrow$ are the incoming and outgoing longwave radiation, Q_{sen} and Q_{lat} are the sensible and latent heat fluxes, Q_{con} is the conductive heat flux. All the terms in the conservation equation have units W m^{-2}, and a positive sign indicates the energy flux is directed into the surface. The energy balance provides a nonlinear equation for the surface temperature, which we solve using Newton's Method when the surface temperature is colder than the melting point temperature T_m. Once the surface temperature reaches the melting point, we instead set the surface temperature $T_s = T_m$ and excess energy Q_n is used to calculate the surface melt according to:

$$\dot{m} = Q_n / L_f, \tag{3.2}$$

where $\dot{m}$ is the melt rate (units of kg m^{-2} s^{-1}) and L_f is the latent heat. We discuss all the terms in the energy balance equation below. Symbols and variables used in the surface energy balance model are listed in Table 3.1.

3.3.2 Radiation

The incoming shortwave and longwave radiation terms, $SW_\downarrow$ and $LW_\downarrow$ are controlled by atmospheric forcing and must be provided as inputs to the model from observations or an atmospheric model. The outgoing longwave radiation $LW_\uparrow$ is es-

timated by the Stefan-Boltzmann equation:

$$LW_{\uparrow} = \varepsilon \sigma {T_s}^4, \tag{3.3}$$

where ε is the surface emissivity for longwave radiation and σ is Stefan-Boltzmann's constant. The reflected shortwave radiation $SW_{\uparrow}$ is calculated using the incoming shortwave radiation and the surface albedo α:

$$SW_{\uparrow} = \alpha SW_{\downarrow}. \tag{3.4}$$

Following *Gardner and Sharp* (2010), we decompose the albedo into a contribution associated with pure snow/firn or ice albedo ($\alpha_{\hat{s}}$) and corrections associated with light absorbing carbon ($\delta\alpha_c$), solar zenith angle ($\delta\alpha_u$) and cloud optical properties ($\delta\alpha_\tau$):

$$\alpha = \alpha_{\hat{s}} + \delta\alpha_c + \delta\alpha_u + \delta\alpha_\tau. \tag{3.5}$$

Details of the parameterization of $\delta\alpha_c$, $\delta\alpha_u$ and $\delta\alpha_\tau$ are in *Gardner and Sharp* (2010). For bare ice we set the albedo to 0.55 based on MODIS satellite data (*Van Angelen et al.*, 2012). We ignore the effect of black carbon on albedo here, but note that this could have a significant effect in portions of the Greenland Ice Sheet.

3.3.3 Snow albedo parameterization

The snow or firn albedo $\alpha_{\hat{s}}$ depends on grain size (*Gardner and Sharp*, 2010):

$$\alpha_{\hat{s}} = 1.48 - \hat{s}^{-0.07}, \tag{3.6}$$

where $\hat{s}$ is the specific surface area of snow or the ice grains. The grain size is also a function of time and increases through metamorphic processes. Snow grain size is also refreshed to snow-like values by the addition of freshly fallen snow. The aging

processes that increase grain size includes dry snow metamorphism, liquid water-induced metamorphism, refreezing of liquid water and the addition of snow. All of these processes are controlled by the layer temperature, temperature gradient, density and liquid water content. Noting that specific surface areas and grain size are related by:

$$\hat{s} = \frac{3}{\rho_i r_e}, \tag{3.7}$$

where $\rho_i \sim 917\text{kg/m}^3$ is the density of snow and r_e is the layer grain size, we use the method proposed by *Flanner and Zender* (2006) to estimate the effect of snow aging on grain size. Following (*Flanner and Zender*, 2006), we assume

$$r_e(t) = [r_e(t-1) + dr_{e,dry} + dr_{e,wet}]f_{old} + r_{e,0}f_{new} + r_{e,rfz}f_{rfrz}, \tag{3.8}$$

$dr_{e,dry}$ is the dry snow metamorphism caused by grain size change, $dr_{e,wet}$ is the water-induced metamorphism caused by grain size change, f_{old} is the mass fraction of snow carrying form previous time, f_{new} is the mass fraction of freshly-fallen snow, f_{rfrz} is the mass fraction of refrozen liquid water, $r_{e,0}$ is the effective radius of freshly-fallen snow, and $r_{e,rfz}$ is the effective radius of refrozen liquid water.

3.3.4 Turbulent heat fluxes

Turbulent heat fluxes are estimated using the bulk aerodynamic method based on Monin-Obukhov similarity theory (e.g., *Andreassen et al.*, 2008):

$$Q_{sen} = \rho_a C_{pa} U_* \theta_*, \tag{3.9}$$

$$Q_{lat} = \rho_a L_v U_* q_*, \tag{3.10}$$

where ρ_a is the air density, C_{pa} is specific heat capacity of air, L_v is the latent heat of evaporation or sublimation, U_* is the surface friction velocity, θ_* is the turbulent

scale parameters for temperature and q_* is the specific humidity. The functions U_*, θ_* and q_* are given by (*Andreassen et al.*, 2008):

$$U_* = \frac{ku(z_r)}{\ln(\frac{z_r}{z_0}) - \Psi_m(\frac{z_r}{L})}, \tag{3.11}$$

$$\theta_* = \frac{k(T_a(z_r) - T_s)}{\ln(\frac{z_r}{z_T}) - \Psi_h(\frac{z_r}{L})}, \tag{3.12}$$

$$q_* = \frac{k(q(z_r) - q(z_q))}{\ln(\frac{z_r}{z_q}) - \Psi_e(\frac{z_r}{L})}. \tag{3.13}$$

k is the von Karman constant, u is the wind speed at reference height z_r and L is the Monin-Obukhov length (*Andreassen et al.*, 2008):

$$L = \frac{\rho_a C_{pa} U_*^3 T_a(z_r)}{kgQ_{sen}}, \tag{3.14}$$

with T_a and T_s air and surface temperatures, Ψ_m, Ψ_e and Ψ_h are stability correction functions, z_0, z_T and z_q are the roughness lengths of wind speed, temperature and water vapor, respectively. With the assumption that $\Psi_e = \Psi_h$, for stable conditions, we apply the stability functions proposed by *Holtslag and De Bruin* (1988),

$$\Psi_m = \frac{az_r}{L} + b(\frac{z_r}{L} - \frac{c}{d})e^{-d\frac{z_r}{L}} + \frac{bc}{d}, \tag{3.15}$$

$$\Psi_h = (1 + \frac{2az_r}{3L})^{1.5} + b(\frac{z_r}{L} - \frac{c}{d})e^{-d\frac{z_r}{L}} - 1, \tag{3.16}$$

with $a = 1$, $b = 2/3$, $c = 5$, $d = 0.35$. For unstable conditions, we use the stability function proposed by *Dyer* (1974):

$$\Psi_m = (1 - 16\frac{z_r}{L})^{-0.25}, \tag{3.17}$$

$$\Psi_h = (1 - 16\frac{z_r}{L})^{-0.5}. \tag{3.18}$$

For z_u, z_q and z_T we use the method proposed by *Andreas* (1987) where

$$\ln(z_T) = \ln(z_0) + 0.317 - 0.565\ln(z/\nu) - 0.183[\ln(z/\nu)]^2, \tag{3.19}$$

and

$$\ln(z_q) = \ln(z_0) + 0.396 - 0.512\ln(z/\nu) - 0.180[\ln(z/\nu)]^2, \tag{3.20}$$

with ν the kinematic viscosity of the air.

The conductive fluxes between the surface and subsurface layer are determined by Fourier's law, discussed in more detail in the subglacial model. We neglect the heat supplied by liquid precipitation, assuming it has a small impact on the energy budget, although this may be a questionable assumption for portions of Greenland, especially in the future if the climate transitions to a wetter state.

3.3.5 Subsurface model

The subsurface model takes the temperature at the surface as a boundary condition and computes the temperature within a column of snow/ice along with any melt/refreezing within the column. The temperature as a function of depth in the englacial model is calculated using the energy equation (*Greuell and Konzelmann*, 1994)

$$\rho C_p \frac{\partial T}{\partial t} = \frac{\partial}{\partial Z}\left(\kappa \frac{\partial T}{\partial Z}\right) + L_f M - L_f F \tag{3.21}$$

where T is the temperature of ice or snow for the layer, κ is the thermal diffusivity, Z is the vertical coordinate, C_p is the heat capacity of the snow and ice, L_f is the latent heat of melting, M is the mass of snow or ice melting mass within the depth and F is the mass of melt water that refreezes. At the bottom of the column we assume no heat transport can occur and we set the vertical temperature gradient to zero.

3.3.6 Enthalpy method

In practice, Equation (3.21) can be cumbersome to implement when both ice, snow and water phases are present. To simplify the treatment of mixed phases, we apply the enthalpy method (*Anderson*, 1976). The specific enthalpy H is defined up to an arbitrary constant as (*Moran et al.*, 2010)

$$H = u + p/\rho, \tag{3.22}$$

where u is the internal energy (relative to a reference configuration) and p/ρ represents the change in energy caused by a volume change. If heat transfer occurs under constant pressure, there is no volume change and we can neglect the second term in Equation (3.22) and the enthalpy becomes $H = U$ (*Aschwanden et al.*, 2012). The enthalpy for a layer with temperature T below the pressure melting temperature T_m, is

$$H = \int_{T_0}^{T} C_p dT^* \tag{3.23}$$

where T_0 is an (arbitrary) reference temperature and we assume C_p is constant. The enthalpy for a layer with water present is defined as:

$$H = \int_{T_0}^{T_m} C_p dT^* + L_f \tag{3.24}$$

The advantage of the enthalpy method is that it simplifies the energy equation when there is a mixture of snow, ice and water, whence we find:

$$H = \begin{cases} \displaystyle\int_{T_0}^{T} C_p dT^* & T < T_m, \\ \displaystyle\int_{T_0}^{T} C_p dT^* + \omega L_f & T = T_m. \end{cases} \tag{3.25}$$

where ω is the water fraction in the layer. Using Equation (3.25), the energy equation then becomes:

$$\rho \frac{\partial H}{\partial T} = \frac{\partial}{\partial z}\left(\kappa \frac{\partial T}{\partial z}\right). \tag{3.26}$$

Because the enthalpy is a function of the layer temperatures, we can retrieve the temperature from the enthalpy and *vice versa*. The advantage of the enthalpy method is that we do not need to solve the Steffan problem associated with the moving melt/refreezing boundary within a layer. The disadvantage is that we are unable to resolve the freezing boundary within individual layers.

We solve Equation (3.26) using a finite difference approximation using an unevenly spaced grid with more closely spaced layers near the surface, where variability is greatest. We use an explicit time step, taking the smallest of the maximum stable time step or 1 hour, whichever is smallest.

3.3.7 Thermal conductivity

To solve the thermal diffusion equation in the englacial model, we need to know the thermal diffusivity κ of the layer. This depends on the density of snow/ice in the column. To estimate density, we use the method given by *Van Dusen* (1929) to calculate the thermal conductivity within each layer:

$$\kappa(\rho) = 0.021 + 4.2 \times 10^{-3}\rho + 2.2 \times 10^{-9}\rho^3, \tag{3.27}$$

where κ is the layer thermal conductivity and ρ is the average density with the layer. For simplicity, we assume the specific heat capacity within every layer is constant.

3.3.8 Density

Density is modulated by two processes: firn densification and refreezing liquid water. This can be encapsulated with an equation of the form:

$$\frac{d\rho}{dt} = K(\rho, T) + \frac{F}{\Delta z}, \tag{3.28}$$

where K represents firn densification, F represents the refreezing rate in units of mass per unit time, and Δz is the layer thickness. We adapted the method from *Arthern et al.* (2010) based on in *situ* measurement of snow, which expresses the change in snow density as:

$$K(\rho, T) = \dot{b}C(\dot{b})g(\rho_{ice} - \rho)\exp(-\frac{E_c}{RT} + \frac{E_g}{RT}), \tag{3.29}$$

where g gravitational acceleration, $\dot{b}$ is the snow accumulation rate, $C(\dot{b})$ is an empirical coefficient, E_c and E_g are the activation energies associated with creep by lattice diffusion and grain growth, respectively and R is the universal gas constant. We use the parameters modified by *Ligtenberg et al.* (2011) based on Greenland measurements:

$$C(\dot{b}) = \begin{cases} 0.0991 - 0.0103\log(\dot{b}) & \text{if } \rho \leq 550 \text{ kg/m}^3, \\ 0.0701 - 0.0086\log(\dot{b}) & \text{if } \rho > 550 \text{ kg/m}^3. \end{cases} \tag{3.30}$$

When surface meltwater is present, liquid water will percolate downward and refreeze at subsurface layers when the layer temperature is below the freezing point.

We define the layer liquid water content W as the mass ratio of liquid water to the total mass of the layer. The maximum irreducible liquid water content of the layer W_{mi} is expressed as a function of layer porosity defined by (*Coleou and Lesaffre*, 1998)

$$W_{mi} = 1.7 + 5.7\frac{P}{1-P}, \tag{3.31}$$

where, $P = 1 - \rho/\rho_{ice}$ is the layer porosity.

If the layer water content is less than the irreducible water content, any liquid water is trapped in the layer and can not percolate lower. If the water content exceeds the threshold, the portion above the threshold will be transported downward to the next layer. We apply the bucket scheme to simulate the percolation processes (*Hirashima et al.*, 2010). In the bucket scheme, the downward moving water is either stored at one of the lower layers provided the layer can store the water, or is drained away from the model as runoff where percolation is prevented, usually at the firn-ice interface. We assume the transport speed is sufficiently rapid so that the meltwater is able to "settle" in a single time step. Surface transport is assumed to occur in the direction where the slope is greatest with an efolding time that is proportional to the slope.

3.3.9 Regridding: Effect of snowfall, melting and densification on layer thickness

Snowfall, melt and densification change the layer thickness, making it difficult to maintain a constant layer thickness over time. We allow the thickness in every layer to change over time by up to 20% of the initially specified layer thickness. When the surface layer thickness change associated with snowfall or melting exceeds the threshold thickness, we re-set the layer thickness to the initial thickness as follows. After fresh snowfall is added to the surface layer, we combine the snowfall with the surface layer using mixture theory (*Lecomte et al.*, 2011; *Aschwanden et al.*, 2012) so that the new layer density and temperature in the layer become:

$$\rho_1^{'} = \frac{\rho_{sn} h_s + \rho_1 h_1}{h_s + h_1}, \tag{3.32}$$

$$T_1^{'} = \frac{T_{sn} h_s + T_1 h_1}{h_s + h_1}, \tag{3.33}$$

where ρ_{sn} and T_{sn} are the fresh snowfall density and temperature, ρ_1 and T_1 are the top layer density and temperature, h_s and h_1 are the snow precipitation thickness and top layer thickness, $\rho_1^{'}$ and $T_1^{'}$ are the new layer density and temperature. We assume freshly fallen snow has a density of 250 kg/m^{-3} and the assume the temperature of snow is identical to the surface air temperature. When the air temperature is above freezing point, the precipitation is taken as liquid water.

After adding snow (Figure 3.1 b and e), the new layer thickness is $h_1' = h_s + h_1$. If the new layer thickness is larger than the accumulated critical threshold thickness H_{ac}, which we set to 120% of the initial layer thickness, we re-grid by separating the surface layer into a portion that equals the original specified initial thickness and combine the excess portion with the adjacent layer below. Then the density and layer temperature in the first layer become:

$$\rho_1^{'} = \frac{\rho_s h_s + \rho_1 (H_1 - h_s)}{H_1}, \tag{3.34}$$

and

$$T_1^{'} = \frac{T_{sn} h_s + T_1 (H_1 - h_s)}{H_1}, \tag{3.35}$$

where H_1 is the initial layer thickness. Then we check the second layer to determine if it now exceeds the threshold. If it does, we separate it using a similar procedure. This can trigger re-gridding in the lower layers, which proceeds analogously.

In contrast, when surface melt or densification occurs, the surface layer will thin. We allow the layer thickness to decrease until the layer thickness is less than 80% of the initially specified layer thickness. Once the layer thickness exceeds the threshold, we combine the surface layer with the adjacent layer below to create a new upper layer thickness equal to the original layer thickness H_1 (Figure 3.1 d and e). We again use mixture theory to combine the layers such that the density and temperature in the

top layer become:

$$\rho_1^{'} = \frac{\rho_1 h_1 + \rho_2 (H_1 - h_1)}{H_1}, \quad T_1^{'} = \frac{T_1 h_1 + T_2 (H_1 - h_1)}{H_1}. \tag{3.36}$$

Similar to before, we then proceed to re-grid the lower layers if necessary.

3.3.10 Layer spacing and domain size

Our interest is in the upper part of the ice sheet and we apply our model to the upper 20 m of the ice sheet surface, but this can be changed for studies over longer periods of time. Layer properties change much more quickly at the surface than the bottom of the column. Because of this, we use more closely spaced layers at the surface and gradually increase layer thickness towards the bottom. We set the thickness of layers so that the top layer is 0.15 meters and layer thickness increases linearly from the surface to the bottom of the domain. We experimented with an array of uneven layer thickness and found our results had little sensitivity to the particular choice, provided we had sufficient resolution in the upper layers.

3.4 Model initialization, spin up and time step

Because this is a column model, every site is independent and can be initialized separately. We first initialize the vertical temperature profile for every site based on the mean annual surface temperature. We assume the density profile linearly increases from 300 kg m^{-3} to 900 kg m^{-3} for the upper 20 meters depth. We then spin the model up by driving the model with the first year of meteorological inputs we have. This is repeated until we obtain a steady state solution for temperature and density. We use this temperature and density profile as the initial condition for all subsequent model runs. This approach works well for the upper layers, where surface melt is concentrated, but ignores the fact that the temperature at tens of

meters depth depends on (non-steady) atmospheric conditions in past decades (or longer). This has little effect on the surface layers, but is problematic for deeper layers. During all model runs we check to make sure mass and energy are conserved. We also conducted sensitivity experiments where we decreased the time step and increased the number of layers in our model, but these changes had little effect on model results.

3.5 Model Calibration and Validation

We first applied our model to several different automatic weather station (AWS) from the PROMICE project (*Ahlstrøm et al.*, 2008) to calibrate uncertain parameters and assess model performance. We use hourly recorded automatic weather station data from each site for the calibration and validation. However, the PROMICE automatic weather stations do not provide precipitation or snow flux data. To account for snowfall, we use ERA-interim precipitation data with nearest neighbor interpolation to provide precipitation for automatic weather stations. Sites used in our calibration and validation are shown in Figure 3.2. Unfortunately, PROMICE sites lie in the ablation zone of the ice sheet making it more difficult to assess model performance in the accumulation zone of the ice sheet. However, our primarily interest for this study is on melt production so the lack of accumulation zone cites is less of a concern for this study.

3.5.1 Model Calibration: Effect of unresolved katabatic winds

The numerical model contains many uncertain parameterizations. For most of these we used "off the shelf " values provided by previous studies. However, the surface roughness (which may vary spatially and even temporally) is poorly constrained by these existing measurements. Before we compare the model results with observational data, we first performed a model calibration for this parameter using the

meteorological data from the automatic weather station at KAN_U (Figure 3.2). We used this site because it contains the longest record with the fewest missing data of all stations we examined.

To perform the calibration, we first sampled the parameter from a specified range. We then ran the model forward for one year (the maximum period of observation at KAN_U) and then assessed model performance by calculating the root mean square (RMS) difference between the simulated and observed surface temperature (Figure 3.3). Examining Figure 3.3, we see that the smallest RMS occurs for an unphysically large surface momentum roughness length of $z_0 = 0.5$ meters. The substantial momentum roughness needed to match observations points to the possibility that our model is underestimating turbulent fluxes associated with katabatic winds. With katabatic winds, the wind speed maximum may occur beneath automatic weather station measurements height (10 m) and this will lead to a substantial underestimate of the turbulent heat flow (*Giesen et al.*, 2008). Following *Giesen et al.* (2008), we applied a reduction factor to the stability correction for the turbulent fluxes of 1/3. With this correction, the minimum roughness length is a more reasonable $z_0 = 0.05$ m (Figure 3.3). We also applied a stability correction factor of 1/9. However, the difference between our best fit roughness when the correction is 1/9 is similar to the roughness when the correction is 1/3, but the 1/3 correction yields a slightly smaller RMS. Hence, we apply the 1/3 correction to turbulent fluxes.

We also optimized for the emissivity and found that our smallest RMS occurred when the emissivity $\epsilon \sim 1.0$, indicating that for the purposes of our model, the surface can be treated to a good approximation as a blackbody. There are numerous additional model parameters that could also be calibrated, but given the large uncertainty in meteorological forcing associated with not resolving katabatic winds we decided to keep the "off the shelf" values of other parameterizations fixed to avoid the possibility that we tune parameterizations to create compensating errors.

Comparing model predictions against observations of surface temperature after only adjusting the roughness and setting the emissivity to unity we see strong agreement between model predictions and observations (Figure 3.4). The difference between daily mean surface temperatures predicted by our model and measured by the AWS range from 0.75°C during 2009 to 0.45°C in 2012 (correction coefficient as 0.99, Figure 3.5). Discrepancies between model predictions and observations are largest during winter where our model predicts warmer temperatures. This may be due to the relative crude correction we make to account for katabatic winds. Even with the relatively crude ERA-interim derived precipitation, our model is able to simulate surface temperatures accurately. However, we caution that surface mass balance derived from ERA-interim snowfall measurements, may be less satisfactory.

3.5.2 Model Validation

To check how well this calibration translates to other sites, we conducted the same comparison at two other sites, KAN_M and THU_U (see Figure 3.2 for locations), with the same best fitting parameters for the surface roughness previously obtained. A scatter plot (Figure 3.5) of modeled versus observed daily mean surface temperature shows that our model is able to reproduce surface temperatures at KAN_M and THU_U (correlation coefficient 0.99). Station KAN_M, where we have nearly 4 years of data, shows a slight (0.45 °C) warm bias whereas station THU_U shows a slight (0.84°C) cold bias. During the melt season, our model requires that the surface temperature must be at the melting point. Observation of the surface temperature from automatic weather stations indicate that the observed surface temperature hovers around the melting point, but occasionally exceeds the melting point temperature, suggesting some observational errors. Nonetheless, these results provide a consistency check that show that model performs well for these three sites.

3.6 Comparison with ERA-interim driven model: comparison with different downscaling schemes

Having demonstrated that our model produces accurate results when driven by high quality automatic weather station data, we next compared model predictions at the same automatic weather station locations, but this time driving the model using ERA-interim reanalysis data combined with statistical downscaling schemes of varying sophistication. Because the ERA-interim data are provided with 3 hour time steps, we linearly interpolate the ERA-interim data to a 1 hour time step so that it is coincident with the automatic weather stations data.

The simplest type of spatial interpolation we can perform is nearest neighbor interpolation. In this scheme, we drive our model with inputs from ERA-interim data associated with the nearest ERA-interim grid cell. This is the most computationally efficient type of interpolation because the surface energy balance at all points within a footprint receive the same forcing and we make no attempt to correct for lapse rate associated with variations in ice sheet surface elevation differences within a footprint. We next compared model results forced with bilinearly interpolated ERA-interim data. Again, we make no attempt to correct for changes in surface temperatures associated with elevation changes. Finally, we examined nearest neighbor and bilinear interpolation methods, but this time we applied a lapse rate correction based on the moist adiabatic lapse rate (-6 K km^{-1}), although the actual lapse rate varies with temperature and humidity.

3.6.1 Performance of different downscaling schemes

To assess model skill for each downscaling scheme, we compared the daily mean surface temperature obtained from the automatic weather station with our model driven by (1) automatic weather station data and (2) ERA-interim interpolated data

(Figure 3.6, 3.8). For consistency, we also compared surface melt rate predictions with surface melt determined using (3) a Positive Degree Day (PDD) method (*Braithwaite*, 1995) and (4) extracted from the MAR regional climate model (*Marco Tedesco and Alexander*, 2013).

Results are summarized in Table 3.3. The difference between observed surface temperature at the automatic weather stations and predicted by our model is, as expected, smallest when we drive the model directly with the automatic weather station data. We do see a degradation in model skill when the model is forced with the much coarser scale ERA-interim reanalysis data, although the model still performs respectably. From Table 3.3, the bilinear interpolation with a lapse rate correction matches observed surface temperatures the best with the smallest temperature difference for site KAN_U, UPE_U and KPC_U. In contrast, the nearest neighbor interpolation method's prediction of surface melt appears to most closely resemble the automatic weather station driven model and regional climate model MAR (*Marco Tedesco and Alexander*, 2013). We note that the advantage of bilinear over nearest neighbor in matching surface temperature is small, while nearest neighbor more closely matches estimates of melt from the AWS and MAR model. Including a lapse rate correction has a small, but positive improvement in all sites. This suggests that nearest-neighbor interpolation with a simple lapse rate correction is a viable means of downscaling ERA-interim forcing.

3.6.2 Comparison between surface temperature and melt using nearest neighbor interpolation

Based on the performance of the nearest neighbor interpolation scheme with a lapse rate correction, we next examined a time series of modeled and observed temperatures and melt rates based on nearest neighbor interpolation with a lapse rate correction for the sites KAN_M, KAN_U and THU_U (Figure 3.6 3.8).

Examining Figure 3.6, we see that as before predicted surface temperatures match observed temperatures remarkably well for all 4 years we have data at KAN_U when the model is driven directly by AWS data. Model performance degrades when we use the downscaled ERA-interim forcing, but predictions of surface temperature remain surprisingly good. The ERA driven model tends to underestimate the magnitude of the high and low peaks of surface temperature. This is likely a consequence of an inadequate wind field needed to accurately simulate sensible heat fluxes.

We also compared melt production rates simulated by the model (forced by AWS and ERA-interim) and positive degree method. Here we have no direct observations of melt production at these sites and consider the AWS driven model the best guess. The length of the simulated melt season is similar for all three methods. Peaks in melt production computed using the downscaled ERA-interim forcing are often larger than peaks computed using other methods. We find, however, that the total melt production is similar for all methods. The melt rate predicted by the PDD method is initially much smaller than the other methods, but grows systematically throughout the melt seasons. The ERA-interim driven model shows smaller melt rates during the beginning and end of the melt season and much large melt rates in the middle of the melt season.

We see similar results at other sites (Figure 3.7 and 3.8). Figure 3.7 clearly shows large interannual variability in melt rates in 2009 versus 2012. This interannual variability is much larger than the differences in melt production estimates using the different methods. This strongly suggests that climate forcing, rather than method of computing melt production, is the most critical variable in computing surface melt.

The site with the greatest variability is THU_U (Figure 3.8), where the melt rate is also the largest (up to 4 m.w.e!). At this site, melt estimated using the AWS forcing is significantly larger than melt computed using the other methods. At this site, model predictions diverge from the observations more than at other sites. The

ERA-interim downscaled forcing is colder on average than the observations suggest. The AWS based melt production estimate is also systematically larger than melt computed using the downscaled data. This may be related to the lapse rate correction we applied. Topography in this region is highly variable and the AWS site is near a topographic high which may lead to an over correction when our simple lapse rate is applied.

3.7 Statistical downscaling with multiple elevation classes

3.7.1 Effect of number of elevation classes

Given the relative insensitivity of our model to the interpolation method, we next attempted to statistically downscale ERA-interim data to generate subgrid scale surface melt estimates across the entire Greenland Ice Sheet. To do this we used a high resolution DEM (*Morlighem et al.*, 2014). We first found all digital elevation model points in every ERA-interim climate forcing footprint, then divided the digital elevation model points into discrete classes based on their surface elevation, analogous to the 10 elevation classes used by the Community Earth System Model (CESM) (*Hurrell et al.*, 2013). For the climate forcing, we obtain the mean surface elevation from ERA-interim geopotential data and correct the climate forcing based on the lapse rate within every elevation class. The model is run for every elevation class and the total melt within the footprint is obtained by adding the melt obtained in each elevation class weighted by the area of glacier ice within each class.

The lapse rate correction downscaling method yields different predicted surface temperature and melt rates within each elevation class (Figure 3.9). Differences are largest in the coastal regions where the surface elevation spans a larger altitude range and smallest in the interior of the ice sheet where the elevation range within a footprint is small. The accuracy of the downscaling, however, depends in part on the number of

elevation classes used. In the interior of the ice sheet, where the elevation is relatively smooth we may only require a handful of classes to resolve variations in surface melt. For example, in Figure 3.9b, there is little difference in the average melt rate when 4 or 8 classes are used. However, near the margins, where slopes are largest, we may require a much larger number of elevation class. Figure 3.9a shows an example where we may need as many as 16 elevation classes to converge. Fortunately, we found that since melt rate varies smoothly with elevation, we could linearly interpolating between 4 elevation classes and then linearly interpolate to estimate the melt production on 16 or more elevation classes. This substantially diminishes the speed of computations.

3.7.2 Application to the Greenland Ice Sheet 2012 melt season

To illustrate the potential of this method, Figure 3.10 shows a comparison between melt production integrated over one year from the state-of-the-art regional model MAR (*Marco Tedesco and Alexander*, 2013) for 2012 and predictions from our ERA-interim driven model with and without downscaling using only 4 elevation classes. Even without downscaling, our model predicts similar magnitudes and patterns of surface melt. However, statistical downscaling results in pronounced differences in regional patterns that more closely resemble regional projections based on MAR, including an 18% increase in surface melt in the Southeastern Greenland and a 14% decrease in mass loss from Southwestern Greenland. The net difference in mass loss is, however, small (about 2%). This suggests that we can obtain realistic results using very simple interpolation schemes and a limited number of elevation classes.

3.8 Conclusions

In this study, we presented a distributed surface energy balance model, combined with a subsurface model that simulates the mass and energy balance of the Greenland Ice Sheet. The model was first calibrated and validated with local automatic weather

station data. Comparison between observed and simulated surface temperatures were consistent with the observational data, with agreement best during the melt season when melt production is largest.

We then showed that model performance was degraded when the model was driven by ERA-interim data, but that we still obtained similar patterns and quantities of melt production. We further found that the agreement could be improved by a very simple nearest-neighbor interpolation that included an elevation dependent lapse-rate correction. Differences between the model and observations were largest during the winter for both the ERA-interim and AWS driven model, hinting that unresolved katabatic winds may play a key role in degrading the model results.

We found that we could decrease the difference between observed and simulated temperatures and melt rates by interpolating the ERA-interim data and applying a crude nearest neighbor lapse rate correction based on the moist adiabatic lapse rate. We only found minor differences between interpolation methods, but found the nearest neighbor interpolation with a lapse rate correction provided the best match with melt rates. Not surprisingly, downscaling had the greatest effect near the coasts, where elevation gradients are largest and the melt amount may differ by a factor of three within a single ERA-footprint.

A crucial limitation of our study is that we focused primarily on melt production. Precipitation is also important in assessing surface mass balance and it may be necessary to examine statistically downscaling schemes for precipitation to improve local mass balance. Overall, the numerical model is relatively cheap and can be incorporated into large-scale ice sheet models at a fraction of the cost of regional models. This is especially true given that we only require 4 elevation classes within a single ERA-interim footprint to perform the downscaling.

Projections of surface mass balance trends for the next century rely on global climate models and, even for a single forcing scenario, there is large variability between

different model predictions. Computationally efficient tools, like our model coupled with statistically downscaling can be used to assess how the model spread influences the range of possible surface mass balance projections, something that is currently challenging to do with regional models. Moreover, our model can be easily integrated into large-scale ice sheet models to provide a more physically based estimate of surface melting and runoff than is possible using a positive degree day.

3.9 Acknowledgments

This project is funded through the NASA Earth and Space Science Fellowship. Data from the Program for Monitoring of the Greenland Ice Sheet (PROMICE) were provided by the Geological Survey of Denmark and Greenland (GEUS) at http://www.promice.dk. Data from the Program for Monitoring of the Greenland Ice Sheet (PROMICE) and the Greenland Analogue Project (GAP) were provided by the Geological Survey of Denmark and Greenland (GEUS) at http://www.promice.dk.

Symbol	Definition	Units
Q_n	Net energy flux	$W\,m^{-2}$
$SW_\downarrow$	Incoming shortwave radiation	$W\,m^{-2}$
$SW_\uparrow$	Reflected shortwave radiation	$W\,m^{-2}$
$LW_\downarrow$	Incoming longwave radiation	$W\,m^{-2}$
$LW_\uparrow$	Outgoing longwave radiation	$W\,m^{-2}$
Q_{sen}	Sensible heat flux	$W\,m^{-2}$
Q_{lat}	Latent heat flux	$W\,m^{-2}$
Q_{con}	Conductive heat flux	$W\,m^{-2}$
$\dot{m}$	Melt amount	$kg\,m^{-2}\,s^{-1}$
L_f	latent heat of melting	$J\,kg^{-1}$
ε	Surface emissivity	
σ	Stephan-Boltzmann constant	$W\,m^{-2}\,K^{-4}$
α	Surface albedo	
$\delta\alpha_c, \delta\alpha_u, \delta\alpha_\tau$	Surface albedo corrections	
$\hat{s}$	Specific surface area	$m^2\,kg$
r_e	Effective radius	m
ρ_s	Surface layer density	$kg\,m^{-3}$
ρ_a	Air density	$kg\,m^{-3}$
C_{pa}	Specific heat capacity	$J\,K^{-1}\,kg^{-1}$
L_{va}	Latent heat of evaporation	$J\,kg^{-1}$
U_*	Surface friction velocity	$m\,s^{-1}$
θ_*	Turbulent scale parameters for temperature	K
q_*	Specific humidity	$g\,kg^{-1}$
k	Von Karman constant	
L	Monin-Obukhov length	m
u	Wind speed at reference height	$m\,s^{-1}$
T_a	Air temperature at reference height	K
T_s	Surface temperature	K
z_r	Reference height	m
z_0, z_T, z_q	Roughness length for momentum, temperature and humidity	m
Ψ_m, Ψ_h, Ψ_e	Stability functions for momentum, temperature and humidity	
ν	Kinematic viscosity of the air	m

Table 3.1: Definitions of symbols and variables used in the surface energy balance model.

Table 3.2: Symbols and variables used in the Surface Energy Balance Model.

Symbol	Definition	Unit
ρ	Density of column layer	$kg\,m^{-3}$
T	Temperature of column layer	K
C_p	Specific heat capacity of column layer	$J\,K^{-1}\,kg^{-3}$
M	Mass of layer melt	kg
F	Refreeze mass of layer water	kg
κ	Thermal conductivity of column layer	$W\,K^{-1}m^{-1}$
Z	Vertical coordinate	m
H	Specific enthalpy	$J\,kg^{-1}$
$K(\rho, T)$	Firn densification	$kg\,m^{-3}s^{-1}$
$C(\dot{b})$	gravitational densification	$kg\,m^{-3}\,s^{-1}$
$\dot{b}$	accumulation rate	$m\,ma^{-1}$
g	gravitational acceleration	$kg\,m^{-3}\,s^{-1}$
ρ_{ice}	density of pure ice	$kg\,m^{-3}\,s$
ρ_w	density of pure water	$kg\,m^{-3}\,s$
R	universal gas constant	$J\,mol^{-1}\,K^{-1}$
Ec	activation energy associated with lattice diffusion	$kJ\,mol^{-1}$
Eg	activation energy associated with grain growth	$kJ\,mol^{-1}$
W	layer liquid water content	
W_{mi}	maximum irreducible liquid water content of the layer	
P	layer porosity	

	KAN_U		KAN_M		THU_U		UPE_U		KPC_U	
Method	ΔT	Melt	ΔT	Melt	ΔT	Melt	ΔT	Melt	ΔT	Melt
AWS	0.65	0.91	0.65	1.80	0.84	3.43	0.86	2.87	0.83	1.13
Nearest Neighbor	1.62	0.75	1.63	1.97	3.08	3.05	3.34	2.47	1.80	0.91
Nearest Lapse	1.55	0.68	1.61	1.68	3.34	2.11	2.99	2.69	1.78	0.89
Bilinear	1.51	0.64	2.13	2.11	2.70	2.52	2.93	2.55	1.75	0.91
Bilinear Lapse	1.49	0.64	2.05	1.21	3.28	1.65	2.81	2.64	1.62	0.77
PDD	–	0.70	–	1.80	–	1.89	–	2.35	–	1.07
MAR Neighbor	1.98	0.75	2.63	1.31	3.12	3.95	1.70	2.78	4.12	0.42

Table 3.3: Comparison between automatic weather station observation data and model result using different statistical downscaling schemes (ΔT is temperature difference with unit K, $Melt$ is melt rate with unit $m.w.e\,yr^{-1}$).

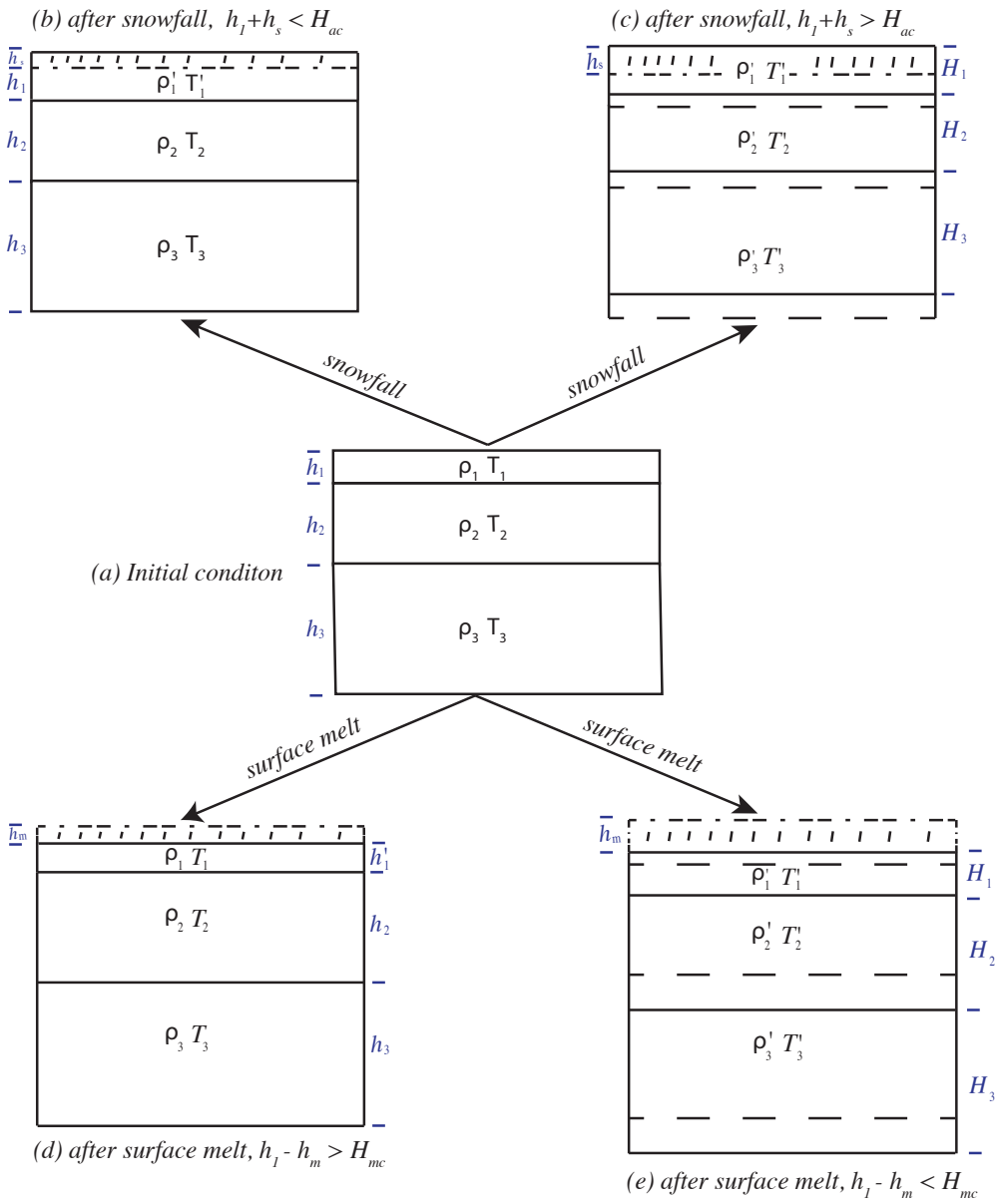

Figure 3.1: Diagram illustrating the layer re-gridding algorithm we use. Middle panel shows the initial condition. Panels b-c show the adjustment of surface layers after snowfall. In panel (b), the increase in layer thickness associated with snow deposition is not sufficient to trigger re-gridding. Panel (c) shows the case when the increased thickness exceeds the critical layer thickness and triggers re-gridding. Panels d-e show the analogous case for surface melting. In panel (d) melting is insufficient to trigger re-gridding. In panel (e), melting thickness exceeds the critical layer thickness and triggers re-gridding.

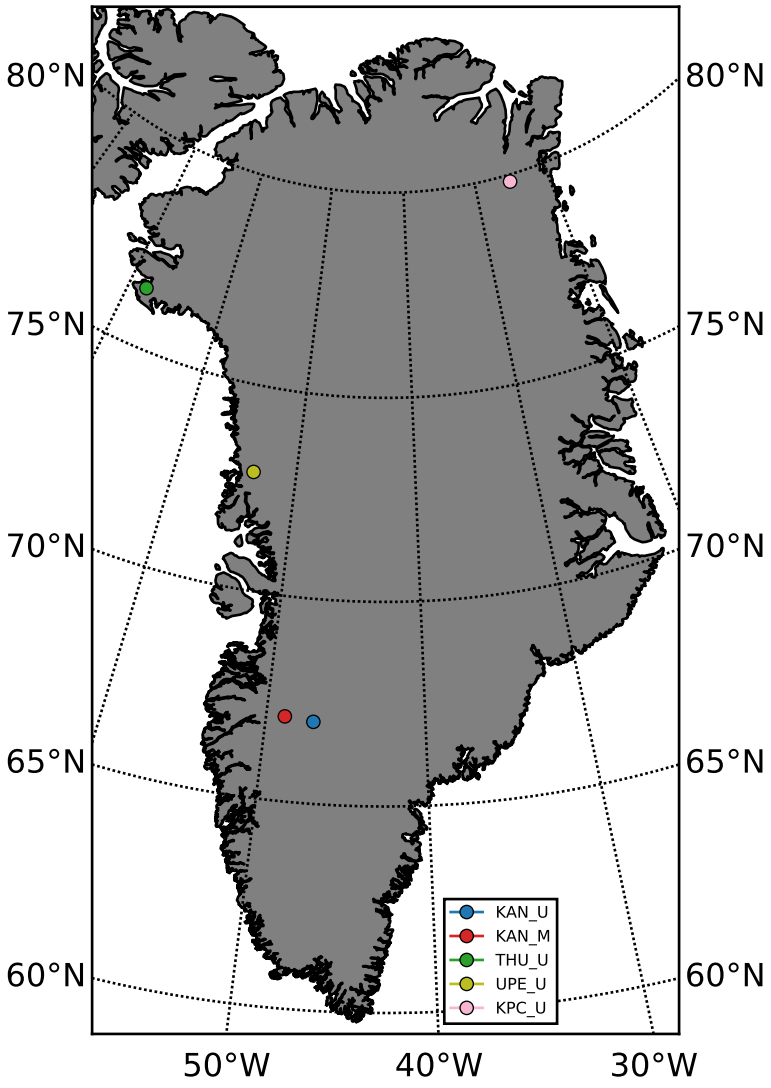

Figure 3.2: Location of five Automatic Weather Stations from the PROMICE network (*Ahlstrøm et al.*, 2008) used for calibration and validation of the surface energy balance model.

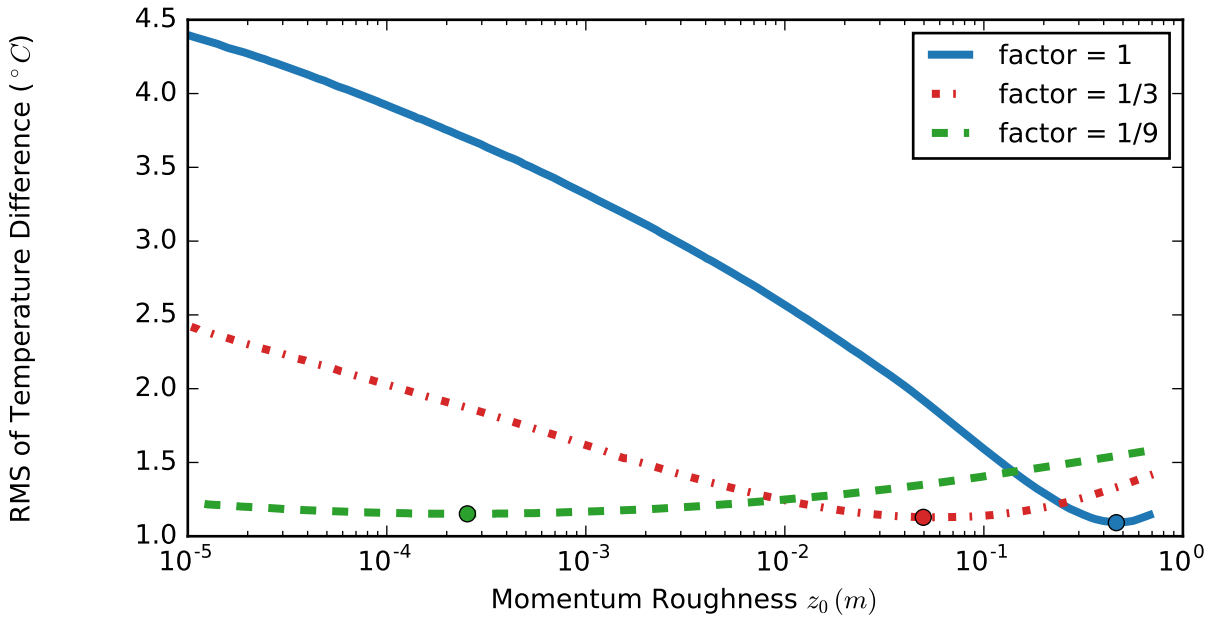

Figure 3.3: Calibration of the roughness for momentum Z_0 at site KAN_U. The blue line shows the RMS temperature misfit for different roughness length scales. The dashed red and green lines shows the roughness when the turbulent fluxes are reduced by factor of 1/3 and 1/9, as might be appropriate if katabatic wind are present.

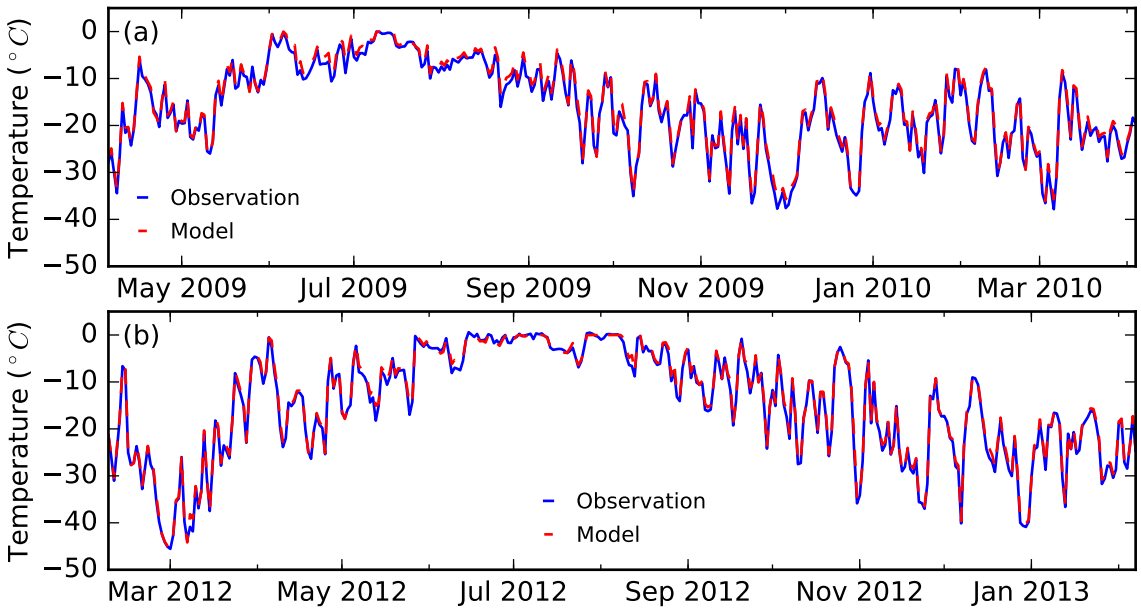

Figure 3.4: Comparison between observed and modeled daily mean surface temperatures result at site KAN_U for two time periods where we have nearly continuous data coverage for one full year. In panel (a) the mean temperature difference is 0.75°C, in panel (b) the mean temperature difference is 0.45°C.

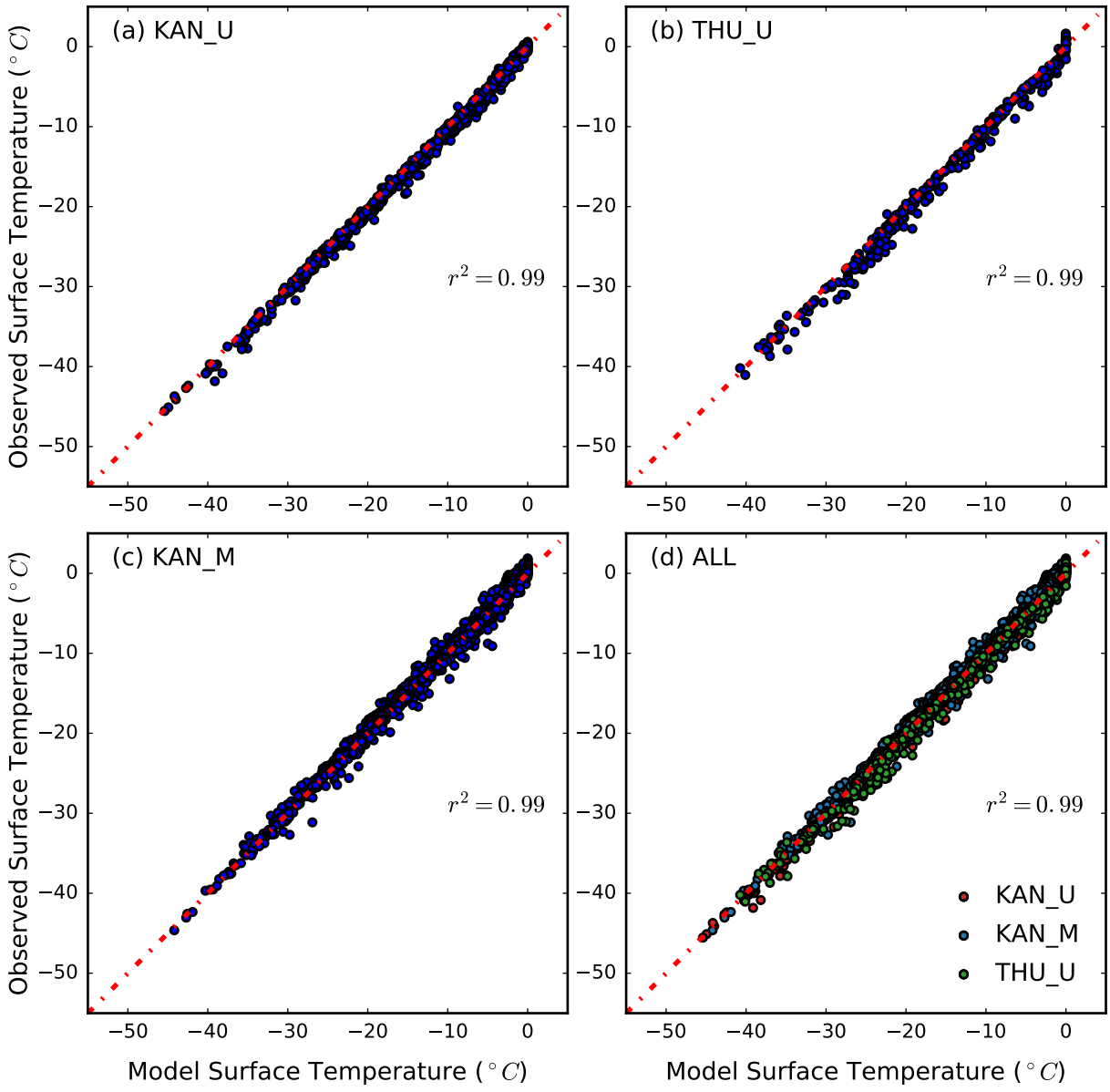

Figure 3.5: Scatter plot of observed versus modeled temperatures at three different stations. Panels a-c show the results for sites KAN_U, THU_U and KAN_M, respectively. Panel d shows a scatter plot for all three sites combined.

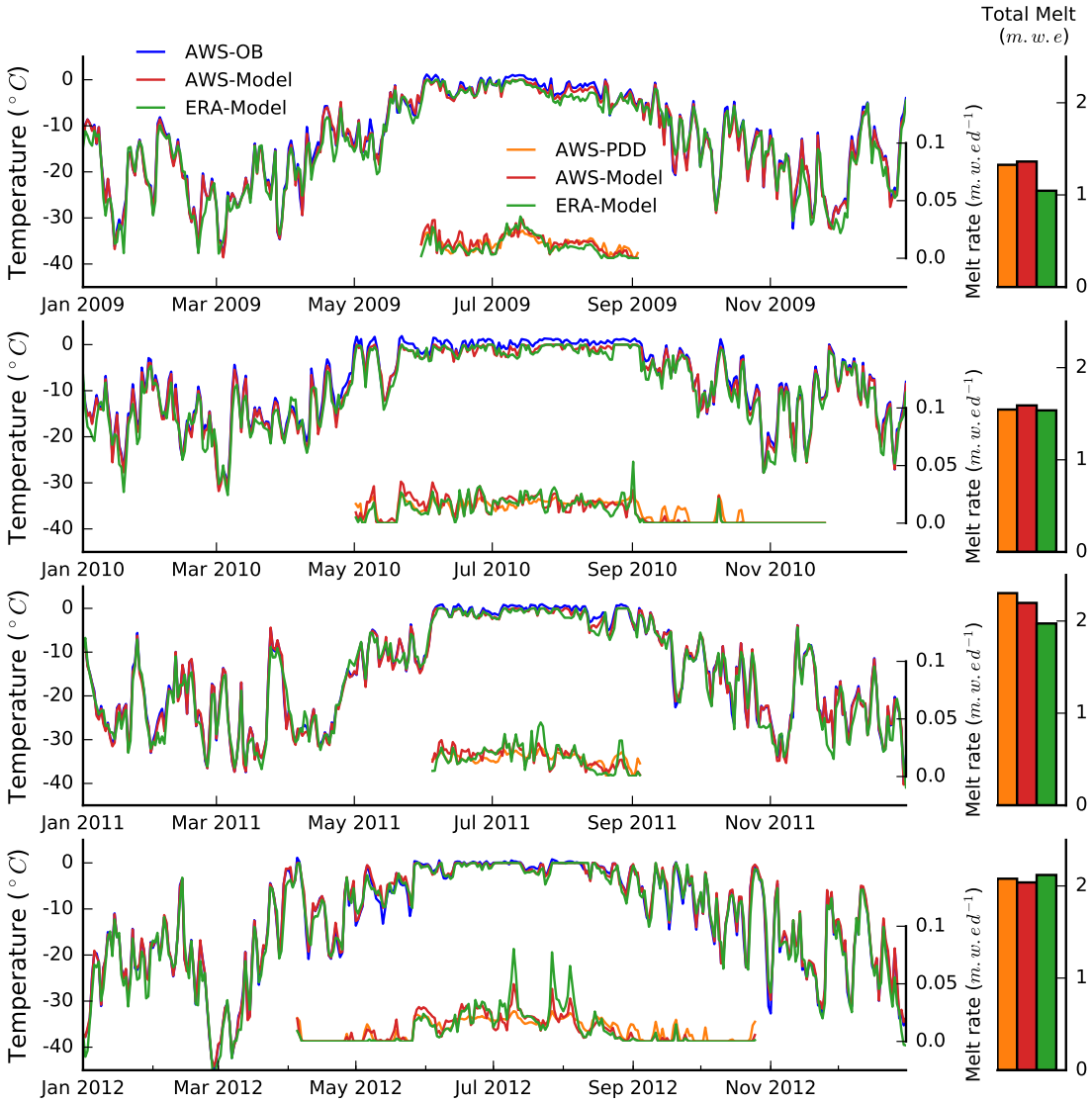

Figure 3.6: Daily mean surface temperature and melt rate at KAN_M for 2009 and 2012. The blue line shows observed surface temperatures from the AWS stations, the red line shows model result driven by the AWS data, the green line shows model result forced with ERA-interim statistically downscaled data using nearest neighbor interpolation with a lapse rate correction. The orange line shows melt production rates estimated with the PDD method driven by AWS data. Total melt production for the year is shown for the three methods on the right with corresponding colors.

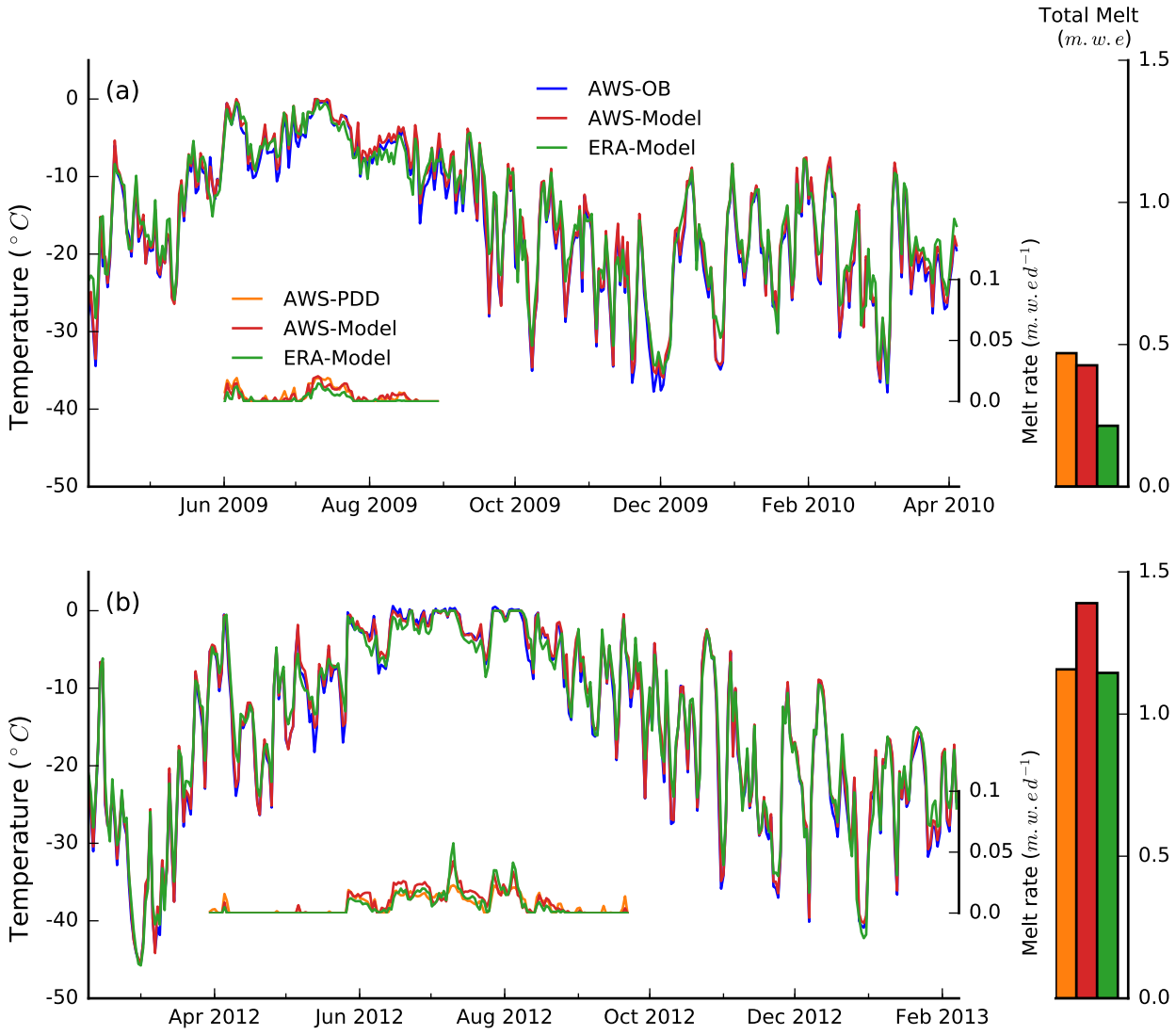

Figure 3.7: Daily mean surface temperature and melt rate at KAN_U for 2009 (Panel a) and 2012 (Panel b). The blue line shows observed surface temperatures from the AWS stations. The red line shows predicted surface temperatures and melt production rates for our model when forced directly with the AWS. The green line shows surface temperature and melt production rates for our model forced by ERA-interim forcing statistically downscaled using nearest neighbor interpolation with a lapse rate correction. The orange line shows melt production rates estimated from the PDD method. Total melt production for the year is shown for the three methods on the right with corresponding colors.

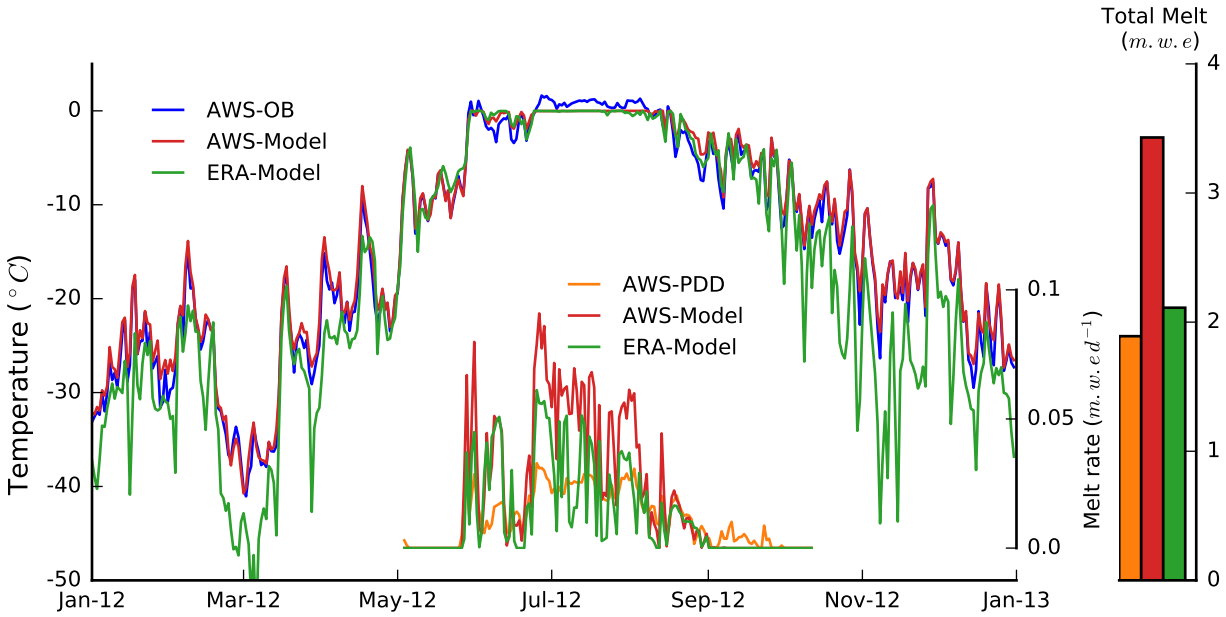

Figure 3.8: Daily mean surface temperature and melt rate at THU_U for 2012. The blue line shows observed surface temperatures from the AWS stations. The red line shows predicted surface temperatures and melt production rates for our model when forced directly with the AWS. The green line shows surface temperature and melt production rates for our model forced by ERA-interim forcing statistically downscaled using nearest neighbor interpolation with a lapse rate correction. The orange line shows melt production rates estimated from the PDD method. Total melt production for the year is shown for the three methods on the right with corresponding colors.

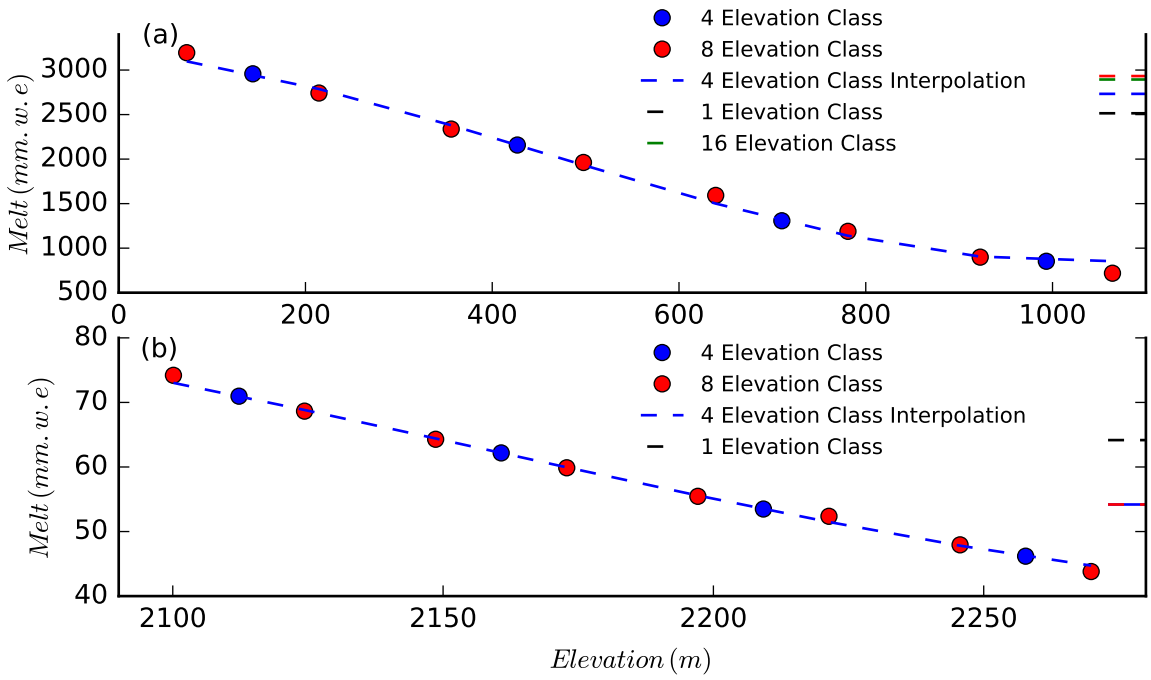

Figure 3.9: The effect of the numbers of elevation classes on the interpolation results. Panel (a) shows integrated melt amount for 2012 for a site with a large topographic gradient (81N, 62W). Panel (b) shows integrated melt amount over 2012 for a site with smaller elevation gradients (77N, 56W). The bars on the right hand side of the figure show the average melt rate within the footprint computed using 1, 4, 8 and 16 elevation classes.

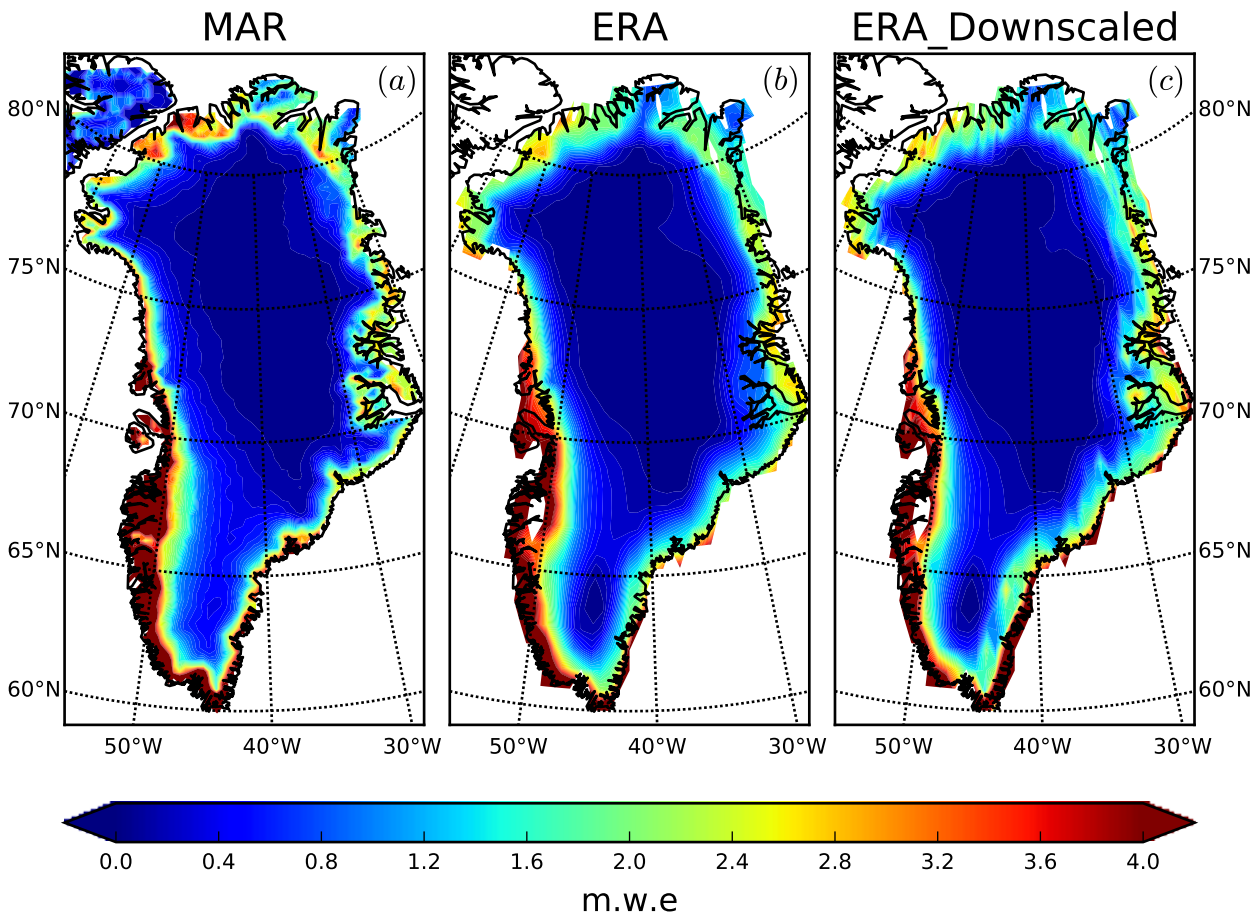

Figure 3.10: Comparison between surface melt production on the Greenland Ice Sheet predicted by the MAR model (Panel a) (*Marco Tedesco and Alexander*, 2013), melt production based on our model driven by ERA-interim result without downscaling (Panel b) and melt producing based on our model driven by ERA-interim with nearest neighbor interpolation and a lapse rate correction (Panel c).

CHAPTER IV

How much can Greenland melt?

4.1 Abstract

Observations show that the Greenland Ice Sheet is losing mass to the ocean at an increasingly rapid rate and this rate is expected to accelerate as the climate continues to warm. Much of the accelerating mass loss from the ice sheet stems from increased mass loss associated with increased surface melt and runoff and this contribution is likely to increase significantly over the next century as atmospheric temperatures continue to rise. However, projections of mass loss associated with surface melting show a range of values with some projections indicating negligible mass loss and others indicating substantial increases in surface mass loss. Here we seek an upper bound of sea level rise originating from Greenland Ice Sheet associated with surface mass balance to assist in 21st century climate projections. We drive a distributed surface energy balance and englacial model with the Coupled Model Intercomparison Project Phase 5 (CMIP5) model ensemble using a range of forcings. To bound ice sheet mass loss, we turn the entire ice sheet dark to account for increased black carbon deposition, assume all meltwater instantaneously drains to the bed through an efficient drainage system and increase the long wavelength radiation assuming that ice sheet is perpetually covered by optically thick clouds. We find that for the baseline simulation, under RCP 8.5 (business as usual) forcing, we obtain 3–12 cm sea level

equivalent by 2100, consistent with previous estimates. With the upper bound, the contribution to sea level from surface melt triples to 10–33 cm. Overall, we find that despite the factor of three range in predictions, surface melt, even under the most extreme conditions is relatively well constrained compared to dynamic discharge, which could contribute as much as 1 m to sea level.

4.2 Introduction

Observations show that mass loss from the Greenland Ice Sheet has accelerated markedly (*Chen et al.*, 2006; *Hanna et al.*, 2008; *Velicogna*, 2009; *Flato et al.*, 2013; *Fettweis et al.*, 2013) with total mass loss doubling over the past decade (*Tedesco et al.*, 2016). This increased mass loss results both from increased dynamic discharge associated with acceleration and retreat of outlet glaciers (*Howat et al.*, 2008, 2007) along with increased surface melt and runoff (*Enderlin et al.*, 2014) associated with the increasingly negative surface mass balance of the ice sheet. As the climate continues to warm, this trend is likely to accelerate with surface mass balance increasingly negative as the melt season lengthens and intensifies. Moreover, once extreme events may become more commonplace. For example, the extreme melt cross Greenland Ice Sheet in 2012 summer set new records for both surface melt extent (*Nghiem et al.*, 2012) and melt duration (*Tedesco et al.*, 2013) was caused by increased long wave radiation associated with optically thick clouds over the ice sheet.

Several studies have sought to constrain the dynamic contribution of the Greenland Ice Sheet to sea level rise (*Pfeffer et al.*, 2008; *Nowicki et al.*, 2013; *Bindschadler et al.*, 2013; *Gillet-Chaulet et al.*, 2012; *Church et al.*, 2013). For example, *Gillet-Chaulet et al.* (2012) estimate that the dynamic contribution of the Greenland Ice Sheet to sea level rise by 2100 is within the range 7–14 cm. In contrast, *Pfeffer et al.* (2008) attempted to bound the potential contribution of the Greenland Ice Sheet to sea level rise assuming that all of Greenland's glaciers and estimated an upper bound

closer to 1 meter of sea level rise equivalent (*Pfeffer et al.*, 2008).

These studies, however, ignored, the contribution of surface melt to the mass balance. Given that surface mass loss currently accounts for nearly two thirds of the current mass loss (*Enderlin et al.*, 2014) and could increase to over 80% (*Goelzer et al.*, 2013), this could result in a substantial underestimate of future projections. Again, previous studies suggest bewilderingly contradictory projections of Greenland surface mass balance to sea level rise in the coming century. For example, early estimates suggest that any increased melt is nearly exactly compensated by an increase in snowfall leading to a negligible contribution sea level rise of <1 cm that is largely independent of emission scenario (*Bugnion*, 2000). In contrast, more recent projections that employ the more advanced machinery of regional climate models suggest a more substantial $\sim$10$\pm$5 cm sea level equivalent by 2100 when models are forced under the business as usual RCP 8.5 emission scenario (*Fettweis et al.*, 2012).

Here we seek to correct this deficiency and seek to bound the contribution that surface melt alone can contribute to sea level rise. Our estimate relies on a surface energy and englacial model, which we drive with atmospheric forcing derived from suite of models associate with the the Coupled Model Inter-comparison Project Phase 5 (CMIP5). We use a simple statistical downscaling scheme, which lacks the finesse of dynamical downscaling using regional models, but has the advantage that, by using appropriate members of the CMIP5 ensemble, we can assess the variability associated with different climate realizations associated with the suite of projections. As we shall show, our simple statistical downscaling scheme yields projections that are consistent with regional model projections. We can also obtain an upper bound by assuming that black carbon covers the ice sheet surface, darkening it (*Tedesco et al.*, 2011, 2016). We further assume that all melt water is instantaneously transported off of the ice sheet to the bed. Finally, we assess errors in cloudiness by assuming that optically thick clouds persist over the entire ice sheet.

4.3 Method

4.3.1 Model description

The model we use here is a surface energy balance model coupled with mutilayer englacial model. The model requires seven climatology inputs: downward shortwave radiation, downward longwave radiation, air temperature, wind speed, humidity, precipitation and surface pressure, which we obtain from the CMIP5 model suite. The model uses these inputs to predict surface melt water production and runoff. The surface mass budget of the Greenland Ice Sheet is then determine from the difference between precipitation (snowfall) and total surface water runoff. Additional details about the model and its validation are given in (*Xiao et al., 2016*). We use the (*Gardner and Sharp*, 2010) albedo parameterization, corrected to account for light absorbing black carbon in snow. For our 'extreme' black snow and ice case, we a 100-fold increase in black carbon in the snow setting black carbon to as 1 m.m.p.v. Once the snow erodes, we set the bare ice albedo to 0.4, consistent with values from 'dark snow' region of Southwestern Greenland (*Wientjes et al.*, 2011). For baseline simulations that do not invoke black carbon, we assume negligible carbon in the snow and use a bare ice albedo of 0.52. Optically thick clouds will decrease both the shortwave radiation and increase the longwave radiation.

In our upper bound we ignore the decrease in incoming shortwave radiation and only consider the increase in long wavelength radiation. Finally, for the upper bound, once snow layers become saturated, we instantaneously removed all meltwater from the ice sheet.

4.3.2 CMIP5 data

We drive our model using a suite of model forcings obtained from the Coupled Model Intercomparison Project Phase 5 (CMIP5). Each model corresponds to a

different realization of the future climate and, by using the suite of models, we can take the multi-model mean and compute the range associated with variation between models for different emission scenarios. We drive our model using a nearest neighbor interpolation with a moist adiabatic lapse rate correction. We use the RCP 8.5 forcing, corresponding to a radiative forcing of $+8.5\,W\,m^{-2}$ by 2100. Details of the datasets we used in the study are in table 4.1. The model was spun up using the first 10 years data (from 2006–2016) until a steady state was reached. The simulation then proceeded from the steady-state configuration. We experimented with different initialization procedures, but these had little effect on our mass loss projections.

Forcing	Institutes	Period	Resolution
ACCESS1.3	Commonwealth Scientific and Industrial Research Organisation	$2006-2100$	$1.25^\circ \times 1.87^\circ$
BCC-CSM1.1	Beijing Climate Center	$2006-2100$	$2.79^\circ \times 2.81^\circ$
BNU-ESM	College of Global Change and Earth System Science	$2006-2100$	$2.79^\circ \times 2.81^\circ$
CanESM2	Canadian Centre for Climate Modelling and Analysis	$2006-2100$	$2.79^\circ \times 2.81^\circ$
GFDL-CM3	Geophysical Fluid Dynamics Laboratory	$2006-2100$	$2.00^\circ \times 2.50^\circ$
INM-CM4	Institute for Numerical Mathematics	$2006-2100$	$1.50^\circ \times 2.00^\circ$
IPSL-CM5A-LR	Institut Pierre Simon Laplace	$2006-2100$	$1.89^\circ \times 3.75^\circ$
MIROC5	The University of Tokyo	$2006-2100$	$1.40^\circ \times 1.40^\circ$
MRI-CGCM3	Meteorological Research Institute	$2006-2100$	$1.12^\circ \times 1.12^\circ$

Table 4.1: Summary of different forcings used in the simulations, resolution is latitude by longitude.

4.3.3 Statistical downscaling

To downscale the data to the ice sheet surface, we divided each CMIP5 model footprint into a set of a elevation classes, which each class encompassing 150 m of elevation. The digital elevation model we used was based on the digital elevation model from (*Ekholm and Krabill*, 2001) with 150 m. We then use nearest neighbor interpolation with an elevation dependent lapse rate correction for surface temperature to downscale the global climate forcing to a resolution appropriate for the ice

sheet.

4.4 Results

We first examined our projections based on the baseline scenario (Figure 4.2). Our estimates of surface mass balance at the beginning of the century are comparable to observations, with the multi-model mean about 200 GT/a. By the end of the century, annual rates of mass loss range from 250–1000 GT/a. These rates translate into a total sea level rise of 3–12 cm by 2100, comparable to prior results (*Fettweis et al.*, 2012). The range in projections associated with different models varies by about a factor of three and remains remarkably steady throughout the simulation period.

We next examined the effect of the 'upper bound' (Figure 4.2). The upper bound roughly triples the mass loss and the rate of mass increases from 250 GT/a to 500–3000 GT/a. This results in an associated increase in sea level rise equivalent of 10–33 cm, by the end of the century. The uncertainty associated with the multi-model ensemble is again consistently about a factor of three, with the lower end of the upper bound simulations overlapping with the upper end of the baseline simulations.

Despite the large variability in model resolution (temporal and spatial), we found little systematic variability in projections using relatively coarse spatial or temporal resolution. This suggests that the spread in outcomes if largely controlled by the different climate sensitivities associated with the different climate models. Moreover, the spread in model outcomes is relatively constrained with the difference between the upper bound and baseline simulations only yielding a factor of three difference (9 cm versus 23 cm).

4.5 Conclusions

In this study, we drove a coupled surface energy balance/englacial model with CMIP5 data set using the RCP 8.5 climate forcing scenario. Unlike some previous studies, we find that Greenland will loss more mass than it gains from precipitation. This mass loss under the baseline scenario will increase from 200 Gt yr^{-1} to 1000 Gt yr^{-1} by the end of the century. Our upper bound increases this range from 500 Gt yr^{-1} to 2500 Gt yr^{-1}. The black carbon will decrease both the snow and bare ice albedo leading to positive feedback that makes the ever increasing mass loss especially dire in the later part of the century. The related sea level will rises by about 30 cm in the upper bound and 8 cm in the baseline scenario. This estimates are far beneath some of the more dire projections where sea level rise from Greenland exceeds 1 m, but even the baseline estimate of $\sim$8 cm constitutes are large increase in sea level rise that is comparable to some estimates of dynamic discharge from Greenland (*Gillet-Chaulet et al.*, 2012). This suggests that surface mass balance and dynamic discharge may play an equal role in determining the fate of the Greenland Ice Sheet. However, even the upper bound is incompatible with estimates of sea level rise that approaches or exceeds 1 m. Sea level rise of this magnitude would require increased dynamical discharge, perhaps of the type envisioned by *Pfeffer et al.* (2008)

4.6 Appendix: Albedo

Albedo is a crucial for our estimate of surface mass balance of Greenland. Figure 4.3 shows a comparison of model predicted albedo in the ablation zone of the ice sheet and in the accumulation zone of the ice sheet with and without black carbon. In the accumulation zone (top panel of Figure 4.3), the addition of black carbon has a smaller effect during the winter because snowfall dilutes the presence of black carbon. The effect of black carbon is largest during the melt season when large melt events

occur, but these events are gradually diluted by the addition of fresh snow. In the ablation zone, the effect of black carbon on the albedo is larger year round (bottom panel of Figure 4.3).

Figure 4.4 shows the average albedo over the entire Greenland over the next century with and without black carbon. Both simulations show the decrease trend of the mean surface albedo. The addition of black carbon systematically decreases the albedo and the albedo in simulations with black carbon decreases more rapidly than simulations without black carbon.

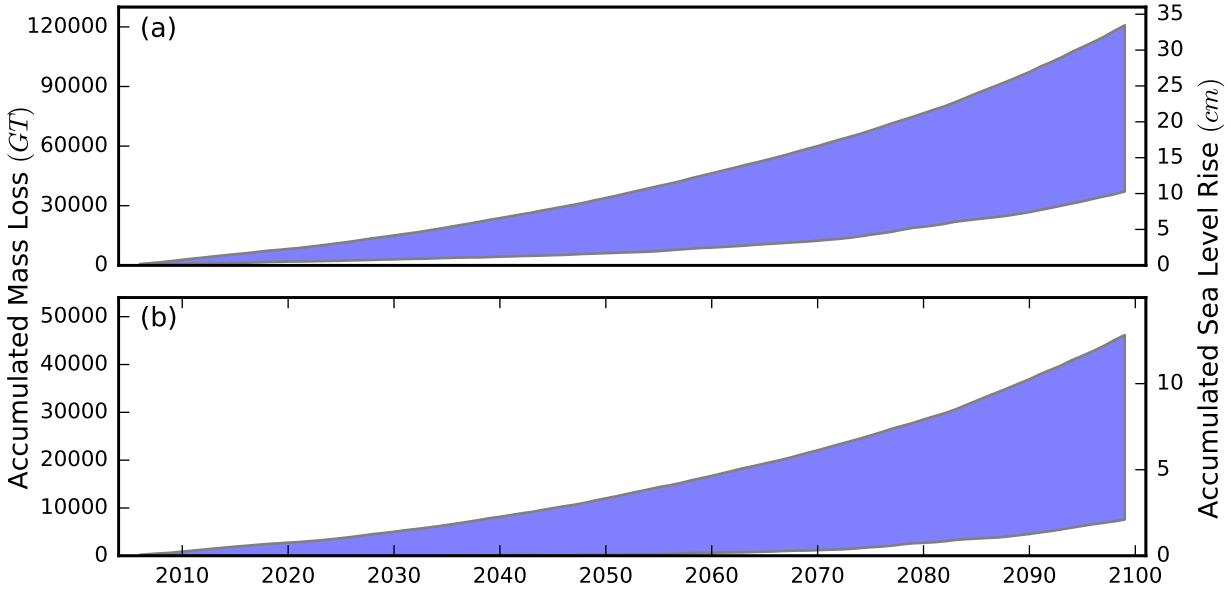

Figure 4.1: Accumulated surface mass loss and related sea level rise for Greenland Ice Sheet. Panel (a) is the upper bound for the Greenland, panel (b) is the baseline mass loss.

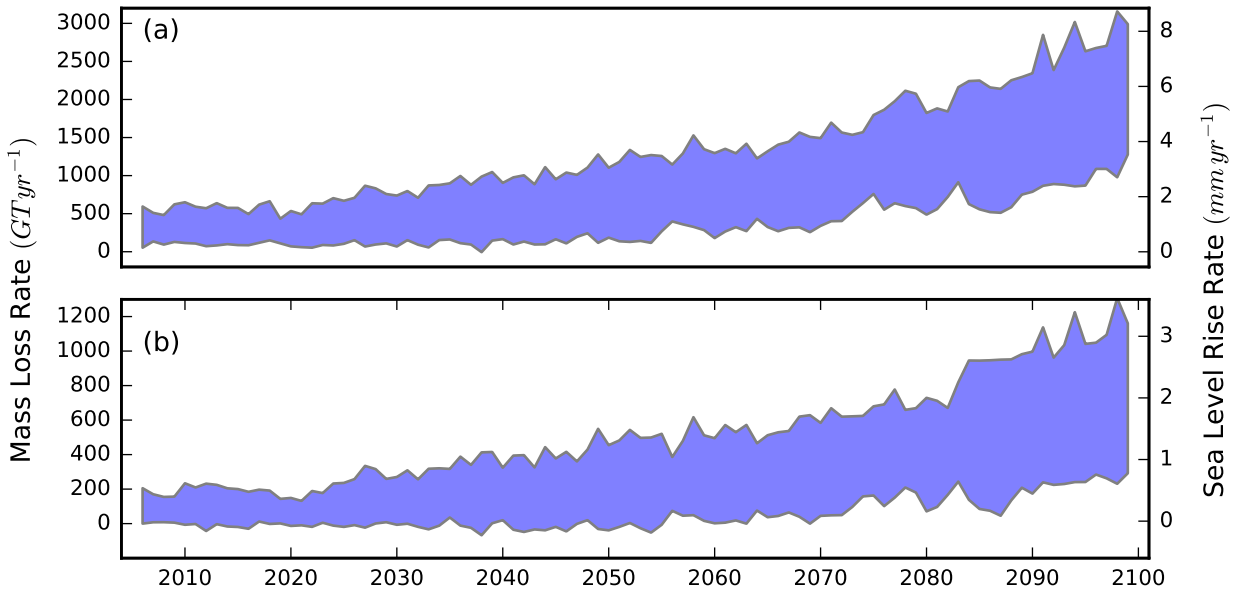

Figure 4.2: Surface mass loss rate and related sea level rise rate for Greenland Ice Sheet. Panel (a) is the upper bound for the Greenland, panel (b) is the baseline mass loss rate.

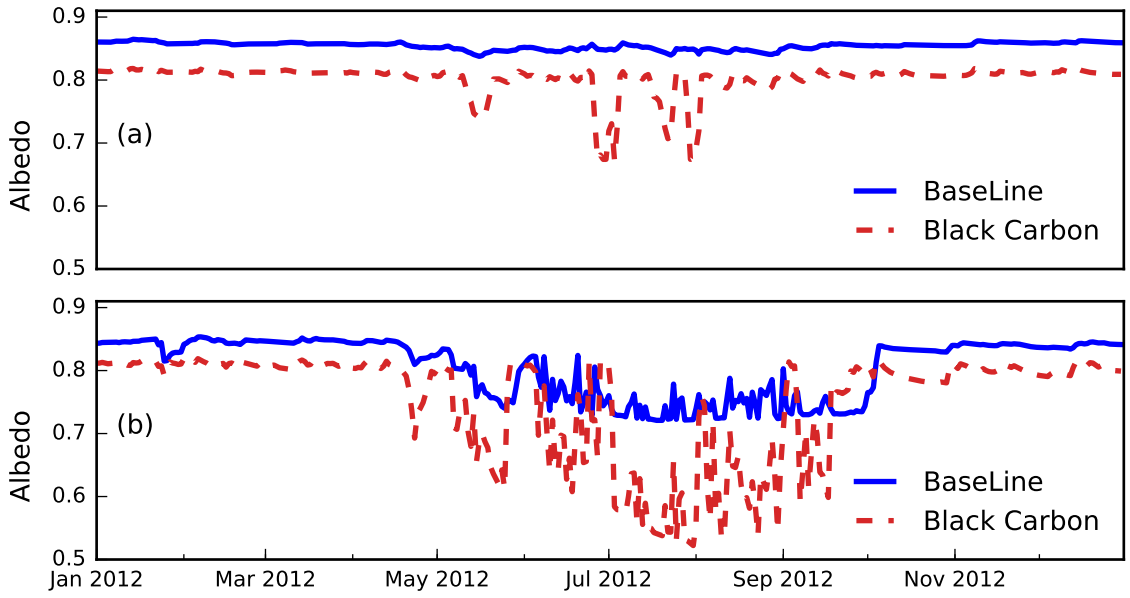

Figure 4.3: Surface albedo comparison between baseline case and with black carbon and low bare ice albedo. Panel (a) shows the albedo comparison between baseline and upper bound cases at accumulation zone (72N, 38W). Panel (b) shows the comparison at ablation zone (67N, 50W). The solid blue line shows the baseline simulation and the dashed red line shows the effect of adding black carbon.

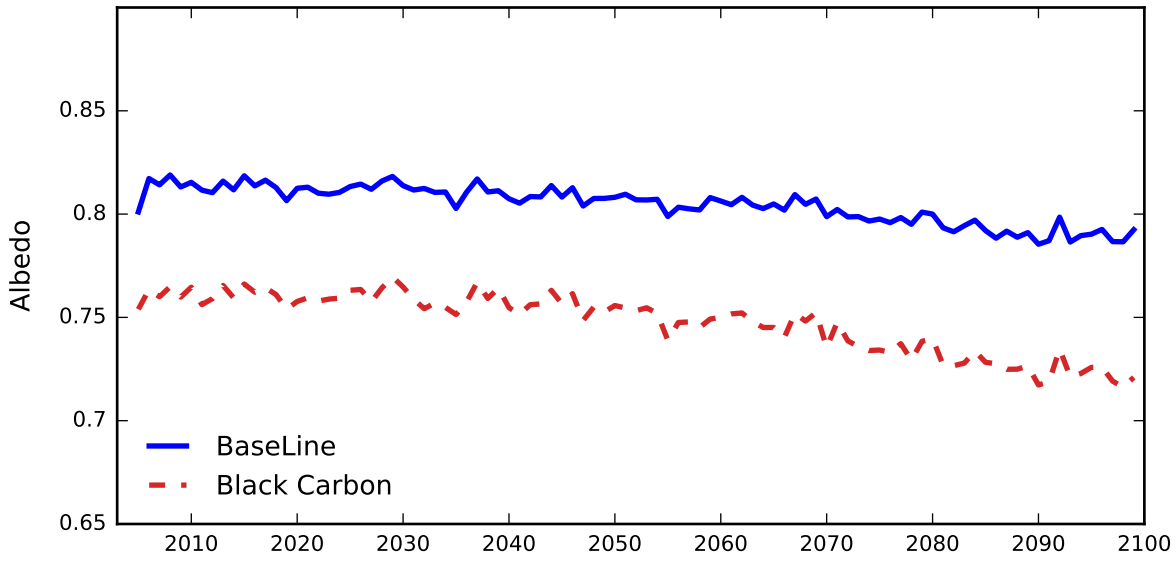

Figure 4.4: Mean surface albedo comparison between baseline and upper bound for Greenland Ice Sheet from $2010 - 2100$. The solid blue line shows the baseline simulation and the dashed red line shows the effect of adding black carbon.

CHAPTER V

Conclusion

This dissertation has discussed surface energy balance model driven by automatic weather station and global climate data to project current and future mass balance of the Greenland Ice Sheet. Specifically, two major topics have been addressed. The first topic describes the model and how model performance degrades when driven by global climate forcing as opposed to high quality automatic weather station data. In the second study, we provide a projection of futureGreenland Ice Sheet surface mass loss in the coming century based on the multimodal CMIP5 ensemble. We describe each of the topics in more detail below.

5.1 Surface Energy and Mass Balance Model

In the first study, we first described how to build our column based physical numerical model on the Greenland Ice Sheet. Then the model was calibrated with the AWS data from the Greenland Ice Sheet. We applied several downscaling and interpolation methods on the global climate data to assess optimal methods to downscale the data. We found the nearest neighbor interpolation method with a local elevation based lapse rate correction performed the best providing melt rates comparable to those obtained when the model was driven by the AWS and regional climate models.

5.2 Upper Bound For Future Projections

In the second study, we predicted the Greenland Ice Sheet surface mass loss in the coming century based on current trends and estimated the worst case scenario assuming perpetual clouds that increased longwave radiation and black carbon turned the ice sheet black. This upper bound suggests that mass loss over the Greenland Ice Sheet could approach 2500 Gt by 2100 with an accumulated sea level rise of 25-30 cm. This is roughly three times the sea level rise associated with our baseline scenario, which suggests 10 cm sea level rise in the coming century.

5.3 Future work

The model developed here has the potential to be used for a range of applications, including long term forecasts of ice sheet surface mass balance and paleo studies of ice sheet surface mass balance. However, there are also areas in which the model could be substantially improved. A few of these are described below.

1. Surface meltwater transport is treated in a crude and idealized manner in our model. In the surface and energy balance model, we remove surface water based on a crude exponential efolding time based on the surface slope . A better method that we have experimented with involves a more detailed meltwater transport model that couples surface transport using a cellular automata model coupled with an ice sheet erosion model. This model improvement allows us to capture meltwater channels and pond formation, key supra-glacial features of the Greenland Ice Sheet surface.

2. An additional weakness of our calibration is that we only were able to calibrate our model using ablation zone data sources. The roughness in ablation zone, needed for turbulent heat transport are usually larger than those in accumulated

zone leading to the potential for a model mismatch in the ablation zone. It would be satisfying to compare the model with more observational data that include the accumulation zone and ablation zone.

3. We have also not explored greatly the effect of using daily averages as opposed to hourly or three hourly data in driving our surface mass balance model. It is possible that we can further improve the efficiency of the model by only using daily means. This would also be advantageous for longer time scale runs when hourly forcing may not be available (CMIP5 model runs rarely record 3 hourly data) and for paleo runs (where only paleoclimate forcing is available).

Overall, we think that these directions would yield promising additional results that could aid the community in developing high quality estimates of ice sheet mass balance.

BIBLIOGRAPHY

BIBLIOGRAPHY

Ahlstrøm, A. P., et al. (2008), A new programme for monitoring the mass loss of the Greenland Ice Sheet, *Geological Survey of Denmark and Greenland Bulletin*, *15*, 61–64.

Andersen, M., et al. (2015), Basin-scale partitioning of Greenland Ice Sheet mass balance components (2007–2011), *Earth and Planetary Science Letters*, *409*, 89–95.

Anderson, E. (1976), A point energy and mass balance model of a snow cover. Silver Spring, MD US. National Oceanic and Atmospheric Administration (NOAA), *Tech. rep.*, Technical Report NWS 19.

Andreas, E. L. (1987), A theory for the scalar roughness and the scalar transfer coefficients over snow and sea ice, *Boundary-Layer Meteorology*, *38*(1-2), 159–184.

Andreassen, L. M., M. R. Van Den Broeke, R. H. Giesen, and J. Oerlemans (2008), A 5 year record of surface energy and mass balance from the ablation zone of Storbreen, Norway, *Journal of Glaciology*, *54*(185), 245–258.

Arthern, R. J., D. G. Vaughan, A. M. Rankin, R. Mulvaney, and E. R. Thomas (2010), In situ measurements of Antarctic snow compaction compared with predictions of models, *Journal of Geophysical Research: Earth Surface*, *115*(F3).

Aschwanden, A., E. Bueler, C. Khroulev, and H. Blatter (2012), An enthalpy formulation for glaciers and ice sheets, *Journal of Glaciology*, *58*(209), 441–457.

Bamber, J., et al. (2013), A new bed elevation dataset for Greenland, *The Cryosphere*, *7*(2), 499–510.

Barletta, V. R., L. S. Sørensen, and R. Forsberg (2013), Scatter of mass changes estimates at basin scale for Greenland and Antarctica, *The Cryosphere*, *7*(5), 1411–1432.

Barry, R., and T. Y. Gan (2011), *The global cryosphere: past, present and future*, Cambridge University Press.

Barry, R., and G. Kiladis (1982), Climatic characteristics of Greenland, *Climatic and physical characteristics of the Greenland Ice Sheet*, *1*, 7–33.

Bates, R. L., J. A. Jackson, et al. (1984), *Dictionary of geological terms*, vol. 584, Anchor Books.

Bennartz, R., M. Shupe, D. Turner, V. Walden, K. Steffen, C. Cox, M. Kulie, N. Miller, and C. Pettersen (2013), July 2012 Greenland melt extent enhanced by low-level liquid clouds, *Nature*, *496*(7443), 83–86.

Bennike, O., and S. Björck (2002), Chronology of the last recession of the Greenland Ice Sheet, *Journal of Quaternary Science*, *17*(3), 211–219.

Bindschadler, R. A., et al. (2013), Ice-sheet model sensitivities to environmental forcing and their use in projecting future sea level (the searise project), *Journal of Glaciology*, *59*(214), 195–224.

Bøggild, C. E., R. E. Brandt, K. J. Brown, and S. G. Warren (2010), The ablation zone in northeast Greenland: ice types, albedos and impurities, *Journal of Glaciology*, *56*(195), 101–113.

Bougamont, M., J. L. Bamber, and W. Greuell (2005), A surface mass balance model for the Greenland Ice Sheet, *Journal of Geophysical Research: Earth Surface*, *110*(F4).

Box, J., X. Fettweis, J. Stroeve, M. Tedesco, D. Hall, and K. Steffen (2012), Greenland Ice Sheet albedo feedback: thermodynamics and atmospheric drivers, *The Cryosphere*, *6*(4), 821–839.

Box, J. E. (2002), Survey of Greenland instrumental temperature records: 1873–2001, *International Journal of Climatology*, *22*(15), 1829–1847.

Box, J. E., D. H. Bromwich, and L.-S. Bai (2004), Greenland Ice Sheet surface mass balance 1991–2000: Application of Polar MM5 mesoscale model and in situ data, *Journal of Geophysical Research: Atmospheres*, *109*(D16).

Box, J. E., D. H. Bromwich, B. A. Veenhuis, L.-S. Bai, J. C. Stroeve, J. C. Rogers, K. Steffen, T. Haran, and S.-H. Wang (2006), Greenland Ice Sheet Surface Mass Balance Variability (1988-2004) from Calibrated Polar MM5 Output, *Journal of Climate*, *19*(12), 2783–2800.

Box, J. E., L. Yang, D. H. Bromwich, and L.-S. Bai (2009), Greenland Ice Sheet Surface Air Temperature Variability: 1840-2007, *Journal of Climate*, *22*(14), 4029–4049.

Braithwaite, R., and O. Olesen (1984), Ice ablation in West Greenland in relation to air temperature and global radiation, *Zeitschrift für Gletscherkunde und Glazialgeologie*, *20*, 155–168.

Braithwaite, R. J. (1995), Positive degree-day factors for ablation on the Greenland Ice Sheet studied by energy-balance modelling, *Journal of Glaciology*, *41*(137), 153–160.

Braithwaite, R. J., and O. B. Olesen (1989), Calculation of glacier ablation from air temperature, West Greenland, in *Glacier fluctuations and climatic change*, pp. 219–233, Springer.

Bromwich, D. H., J. J. Cassano, T. Klein, G. Heinemann, K. M. Hines, K. Steffen, and J. E. Box (2001), Mesoscale Modeling of Katabatic Winds over Greenland with the Polar MM5, *Monthly Weather Review*, *129*(9), 2290–2309.

Brun, E., E. Martin, V. Simon, C. Gendre, and C. Coleou (1989), An energy and mass model of snow cover suitable for operational avalanche forecasting, *Journal of Glaciology*, *35*(121), 333–342.

Brun, E., P. David, M. Sudul, and G. Brunot (1992), A numerical model to simulate snow-cover stratigraphy for operational avalanche forecasting, *Journal of Glaciology*, *38*(128), 13–22.

Buchardt, S. L., and D. Dahl-Jensen (2007), Estimating the basal melt rate at NorthGRIP using a Monte Carlo technique, *Annals of Glaciology*, *45*(1), 137–142.

Bugnion, V. (2000), Reducing the uncertainty in the contribution of greenland to sea-level rise in the 20th and 21st centuries, *Annals of Glaciology*, *31*(1), 121–125.

Cassano, J. J., J. E. Box, D. H. Bromwich, L. Li, and K. Steffen (2001), Evaluation of Polar MM5 simulations of Greenland's atmospheric circulation, *Journal of Geophysical Research: Atmospheres*, *106*(D24), 33,867–33,889.

Cazenave, A. (2006), How fast are the ice sheets melting?, *Science*, *314*(5803), 1250.

Cazenave, A., and F. Remy (2011), Sea level and climate: measurements and causes of changes, *Wiley Interdisciplinary Reviews: Climate Change*, *2*(5), 647–662.

Chen, J., C. Wilson, and B. Tapley (2006), Satellite gravity measurements confirm accelerated melting of Greenland Ice Sheet, *Science*, *313*(5795), 1958–1960.

Church, J. A., and N. J. White (2006), A 20th century acceleration in global sea-level rise, *Geophysical research letters*, *33*(1).

Church, J. A., et al. (2013), Sea-level rise by 2100, *Science*, *342*(6165), 1445–1445.

Coleou, C., and B. Lesaffre (1998), Irreducible water saturation in snow: experimental results in a cold laboratory, *Annals of Glaciology*, *26*, 64–68.

Cuffey, K. M., and W. S. B. Paterson (2010), *The physics of glaciers*, Academic Press.

Dahl-Jensen, D., et al. (2009), The Greenland Ice Sheet in a Changing Climate: Snow, *Water, Ice and Permafrost in the Arctic (SWIPA), Arctic Monitoring and Assessment Programme (AMAP), Oslo.*

Das, S. B., I. Joughin, M. D. Behn, I. M. Howat, M. A. King, D. Lizarralde, and M. P. Bhatia (2008), Fracture propagation to the base of the Greenland Ice Sheet during supraglacial lake drainage, *Science*, *320*(5877), 778–781.

De Ridder, K., and H. Gallée (1998), Land surface-induced regional climate change in southern Israel, *Journal of applied meteorology*, *37*(11), 1470–1485.

Douville, H., J. F. Royer, and J. F. Mahfouf (1995), A new snow parameterization for the Meteo-France climate model, *Climate Dynamics*, *12*(1), 21–35.

Dumont, M., E. Brun, G. Picard, M. Michou, Q. Libois, J. Petit, M. Geyer, S. Morin, and B. Josse (2014), Contribution of light-absorbing impurities in snow to Greenland's darkening since 2009, *Nature Geoscience*, *7*(7), 509–512.

Dyer, A. (1974), A review of flux-profile relationships, *Boundary-Layer Meteorology*, *7*(3), 363–372.

Ekholm, S., and W. B. Krabill (2001), A new, high-resolution digital elevation model of Greenland fully validated with airborne laser altimeter data, *Journal of Geophysical Research*, *106*(B4), 6733–6745.

Enderlin, E. M., I. M. Howat, S. Jeong, M.-J. Noh, J. H. Angelen, and M. R. Broeke (2014), An improved mass budget for the Greenland Ice Sheet, *Geophysical Research Letters*, *41*(3), 866–872.

Ettema, J., M. R. van den Broeke, E. van Meijgaard, W. J. van de Berg, J. L. Bamber, J. E. Box, and R. C. Bales (2009), Higher surface mass balance of the Greenland Ice Sheet revealed by high-resolution climate modeling, *Geophysical Research Letters*, *36*(12).

Ettema, J., M. Van den Broeke, E. v. Meijgaard, W. Van de Berg, J. Box, and K. Steffen (2010a), Climate of the Greenland Ice Sheet using a high-resolution climate model–Part 1: Evaluation, *The Cryosphere*, *4*(4), 511–527.

Ettema, J., M. Van den Broeke, E. Van Meijgaard, W. Van de Berg, et al. (2010b), Climate of the Greenland Ice Sheet using a high-resolution climate model-Part 2: Near-surface climate and energy balance, *The Cryosphere*, *4*(4), 529–544.

Fahnestock, M., W. Abdalati, I. Joughin, J. Brozena, and P. Gogineni (2001), High geothermal heat flow, basal melt, and the origin of rapid ice flow in central Greenland, *Science*, *294*(5550), 2338–2342.

Fettweis, X. (2007), Reconstruction of the 1979-2006 Greenland Ice Sheet surface mass balance using the regional climate model MAR, *The Cryosphere*, *1*(1), 21–40.

Fettweis, X., H. Gallée, F. Lefebre, and J.-P. Van Ypersele (2005), Greenland surface mass balance simulated by a regional climate model and comparison with satellite-derived data in 1990–1991, *Climate Dynamics*, *24*(6), 623–640.

Fettweis, X., B. Franco, M. Tedesco, J. Van Angelen, J. Lenaerts, M. Van den Broeke, H. Gallée, et al. (2012), Estimating Greenland Ice Sheet surface mass balance contribution to future sea level rise using the regional atmospheric climate model MAR, *Cryosphere discussions*, *6*, 3101–3147.

Fettweis, X., E. Hanna, C. Lang, A. Belleflamme, M. Erpicum, and H. Gallée (2013), Important role of the mid-tropospheric atmospheric circulation in the recent surface melt increase over the Greenland ice sheet, *Cryosphere (The)*, *7*, 241–248.

Finsterwalder, S. (1887), Der suldenferner, *Zeitschrift des Deutschen und Osterreichischen Alpenvereins*, *18*, 72–89.

FitzGerald, D. M., M. S. Fenster, B. A. Argow, and I. V. Buynevich (2008), Coastal impacts due to sea-level rise, *Annu. Rev. Earth Planet. Sci.*, *36*, 601–647.

Flanner, M. G., and C. S. Zender (2006), Linking snowpack microphysics and albedo evolution, *Journal of Geophysical Research: Atmospheres*, *111*(D12).

Flato, G., et al. (2013), Evaluation of Climate Models. In: Climate Change 2013: The Physical Science Basis. Contribution of Working Group I to the Fifth Assessment Report of the Intergovernmental Panel on Climate Change, *Climate Change 2013*, *5*, 741–866.

Forster, R. R., et al. (2014), Extensive liquid meltwater storage in firn within the Greenland Ice Sheet, *Nature Geoscience*, *7*(2), 95–98.

Gallée, H., and G. Schayes (1994), Development of a three-dimensional meso-γ primitive equation model: katabatic winds simulation in the area of Terra Nova Bay, Antarctica, *Monthly Weather Review*, *122*(4), 671–685.

Gardner, A. S., and M. J. Sharp (2010), A review of snow and ice albedo and the development of a new physically based broadband albedo parameterization, *Journal of Geophysical Research: Earth Surface*, *115*(F1).

Giesen, R., M. Van den Broeke, J. Oerlemans, and L. Andreassen (2008), Surface energy balance in the ablation zone of Midtdalsbreen, a glacier in southern Norway: interannual variability and the effect of clouds, *Journal of Geophysical Research: Atmospheres*, *113*(D21).

Gillet-Chaulet, F., O. Gagliardini, H. Seddik, M. Nodet, G. Durand, C. Ritz, T. Zwinger, R. Greve, and D. G. Vaughan (2012), Greenland ice sheet contribution to sea-level rise from a new-generation ice-sheet model, *The Cryosphere*, *6*(6), 1561–1576.

Goelzer, H., P. Huybrechts, J. J. Fürst, F. Nick, M. L. Andersen, T. L. Edwards, X. Fettweis, A. J. Payne, and S. Shannon (2013), Sensitivity of Greenland Ice Sheet projections to model formulations, *Journal of Glaciology*, *59*(216), 733–749.

Gregory, J., and P. Huybrechts (2006), Ice-sheet contributions to future sea-level change, *Philosophical Transactions of the Royal Society of London A: Mathematical, Physical and Engineering Sciences*, *364*(1844), 1709–1732.

Greuell, W. (1992), Hintereisferner, Austria: mass-balance reconstruction and numerical modelling of the historical length variations, *Journal of Glaciology*, *38*(129), 233–244.

Greuell, W., and T. Konzelmann (1994), Numerical modelling of the energy balance and the englacial temperature of the Greenland Ice Sheet. Calculations for the ETH-Camp location (West Greenland, 1155 m asl), *Global and Planetary Change*, *9*(1), 91–114.

Groh, A., H. Ewert, M. Fritsche, A. Rülke, R. Rosenau, M. Scheinert, and R. Dietrich (2014), Assessing the current evolution of the Greenland Ice Sheet by means of satellite and ground-based observations, *Surveys in Geophysics*, *35*(6), 1459–1480.

Håkansson, L., J. Briner, H. Alexanderson, A. Aldahan, and G. Possnert (2007), 10 Be ages from central east Greenland constrain the extent of the Greenland Ice Sheet during the Last Glacial Maximum, *Quaternary Science Reviews*, *26*(19), 2316–2321.

Hall, D., G. Riggs, and V. Salomonson (2011), MODIS/Terra snow cover daily L3 global 0.05 Deg CMG V004, *Boulder, CO, USA: National Snow and Ice Data Center*.

Hanna, E., P. Valdes, and J. McConnell (2001), Patterns and variations of snow accumulation over Greenland, 1979-98, from ECMWF analyses, and their verification, *Journal of climate*, *14*(17), 3521–3535.

Hanna, E., P. Huybrechts, K. Steffen, J. Cappelen, R. Huff, C. Shuman, T. Irvine-Fynn, S. Wise, and M. Griffiths (2008), Increased runoff from melt from the Greenland Ice Sheet: a response to global warming, *Journal of Climate*, *21*(2), 331–341.

Harper, J., N. Humphrey, W. Pfeffer, J. Brown, and X. Fettweis (2012), Greenland Ice-Sheet contribution to sea-level rise buffered by meltwater storage in firn, *Nature*, *491*(7423), 240–243.

Hartmann, D. L. (2015), *Global physical climatology*, vol. 103, Newnes.

Helm, V., A. Humbert, and H. Miller (2014), Elevation and elevation change of Greenland and Antarctica derived from CryoSat-2, *The Cryosphere*, *8*(4), 1539–1559.

Hirashima, H., S. Yamaguchi, A. Sato, and M. Lehning (2010), Numerical modeling of liquid water movement through layered snow based on new measurements of the water retention curve, *Cold Regions Science and Technology*, *64*(2), 94–103.

Hock, R. (1999), A distributed temperature-index ice-and snowmelt model including potential direct solar radiation, *Journal of Glaciology*, *45*(149), 101–111.

Hock, R. (2003), Temperature index melt modelling in mountain areas, *Journal of Hydrology*, *282*(1), 104–115.

Hock, R. (2005), Glacier melt: a review of processes and their modelling, *Progress in physical geography*, *29*(3), 362–391.

Hock, R., V. Radic, et al. (2007), Climate sensitivity of Storglaciaren, Sweden: an intercomparison of mass-balance models using ERA-40 re-analysis and regional climate model data, *Annals of glaciology*, *46*(1), 342–348.

Holtslag, A., and H. De Bruin (1988), Applied modeling of the nighttime surface energy balance over land, *Journal of Applied Meteorology*, *27*(6), 689–704.

Howat, I. M., and A. Eddy (2011), Multi-decadal retreat of Greenland's marine-terminating glaciers, *Journal of Glaciology*, *57*(203), 389–396.

Howat, I. M., I. Joughin, and T. A. Scambos (2007), Rapid changes in ice discharge from Greenland outlet glaciers, *Science*, *315*(5818), 1559–1561.

Howat, I. M., I. Joughin, M. Fahnestock, B. E. Smith, and T. A. Scambos (2008), Synchronous retreat and acceleration of southeast Greenland outlet glaciers 2000–06: Ice dynamics and coupling to climate, *Journal of Glaciology*, *54*(187), 646–660.

Hurrell, J. W., et al. (2013), The community earth system model: a framework for collaborative research, *Bulletin of the American Meteorological Society*, *94*(9), 1339–1360.

Huybrechts, P. (1994), The present evolution of the Greenland Ice Sheet: an assessment by modelling, *Global and Planetary Change*, *9*(1-2), 39–51.

Huybrechts, P. (2002), Sea-level changes @articlenowicki2013insights, title=Insights into spatial sensitivities of ice mass response to environmental change from the SeaRISE ice sheet modeling project II: Greenland, author=Nowicki, Sophie and Bindschadler, Robert A and Abe-Ouchi, Ayako and Aschwanden, Andy and Bueler, Ed and Choi, Hyeungu and Fastook, Jim and Granzow, Glen and Greve, Ralf and Gutowski, Gail and others, journal=Journal of Geophysical Research: Earth Surface, volume=118, number=2, pages=1025–1044, year=2013, publisher=Wiley Online Library at the LGM from ice-dynamic reconstructions of the Greenland and Antarctic ice sheets during the glacial cycles, *Quaternary Science Reviews*, *21*(1), 203–231.

Huybrechts, P., A. Letreguilly, and N. Reeh (1991), The Greenland Ice Sheet and greenhouse warming, *Palaeogeography, Palaeoclimatology, Palaeoecology*, *89*(4), 399–412.

Immerzeel, W. W., L. P. Van Beek, and M. F. Bierkens (2010), Climate change will affect the Asian water towers, *Science*, *328*(5984), 1382–1385.

Jacob, T., J. Wahr, W. T. Pfeffer, and S. Swenson (2012), Recent contributio @articlenowicki2013insights, title=Insights into spatial sensitivities of ice mass response to environmental change from the SeaRISE ice sheet modeling project II: Greenland, author=Nowicki, Sophie and Bindschadler, Robert A and Abe-Ouchi, Ayako and Aschwanden, Andy and Bueler, Ed and Choi, Hyeungu and Fastook, Jim and Granzow, Glen and Greve, Ralf and Gutowski, Gail and others, journal=Journal of Geophysical Research: Earth Surface, volume=118, number=2, pages=1025–1044, year=2013, publisher=Wiley Online Library ns of glaciers and ice caps to sea level rise, *Nature*, *482*(7386), 514–518.

Janssens, I., and P. Huybrechts (2000), The treatment of meltwater retention in mass-balance parameterizations of the Greenland Ice Sheet, *Annals of Glaciology*, *31*(1), 133–140.

Jordan, R. (1991), A one-dimensional temperature model for a snow cover: Technical documentation for SNTHERM. 89., *Tech. rep.*, DTIC Document.

Kehrwald, N. M., L. G. Thompson, Y. Tandong, E. Mosley-Thompson, U. Schotterer, V. Alfimov, J. Beer, J. Eikenberg, and M. E. Davis (2008), Mass loss on Himalayan glacier endangers water resources, *Geophysical Research Letters*, *35*(22).

Key, J., C. Fowler, J. Maslanik, T. Haran, T. Scambos, and W. Emery (2002), The Extended AVHRR Polar Pathfinder (APP-x) Product, v 1.0, *Digital Media, Space Science and Engineering Center, University of Wisconsin, Madison, WI*.

Khan, S. A., A. Aschwanden, A. A. Bjørk, J. Wahr, K. K. Kjeldsen, and K. H. Kjær (2015), Greenland Ice Sheet mass balance: a review, *Reports on Progress in Physics*, *78*(4), 046,801.

Khan, S. A., et al. (2014), Sustained mass loss of the northeast Greenland Ice Sheet triggered by regional warming, *Nature Climate Change*, *4*(4), 292–299.

Koenig, L. S., C. Miège, R. R. Forster, and L. Brucker (2014), Initial in situ measurements of perennial meltwater storage in the Greenland firn aquifer, *Geophysical Research Letters*, *41*(1), 81–85.

Kuhn, M. (1993), Methods of assessing the effects of climatic changes on snow and glacier hydrology, *IAHS Publications-Publications of the International Association of Hydrological Sciences*, *218*, 135–144.

Kuusisto, E. (1980), On the values and variability of degree-day melting factor in Finland, *Hydrology Research*, *11*(5), 235–242.

Lambeck, K., T. M. Esat, and E.-K. Potter (2002), Links between climate and sea levels for the past three million years, *Nature*, *419*(6903), 199–206.

Lecomte, O., T. Fichefet, M. Vancoppenolle, and M. Nicolaus (2011), A new snow thermodynamic scheme for large-scale sea-ice models, *Annals of Glaciology*, *52*(57), 337–346.

Lefebre, F., H. Gallée, J.-P. van Ypersele, and W. Greuell (2003), Modeling of snow and ice melt at ETH Camp (West Greenland): a study of surface albedo, *Journal of Geophysical Research: Atmospheres*, *108*(D8).

Lenaerts, J., M. Den Broeke, W. Berg, E. v. Meijgaard, and P. Kuipers Munneke (2012), A new, high-resolution surface mass balance map of Antarctica (1979–2010) based on regional atmospheric climate modeling, *Geophysical Research Letters*, *39*(4).

Lenaerts, J. T., M. Vizcaino, J. Fyke, L. Kampenhout, and M. R. Broeke (2016), Present-day and future Antarctic ice sheet climate and surface mass balance in the Community Earth System Model, *Climate Dynamics*, pp. 1–15.

Lenderink, G., B. van den Hurk, E. van Meijgaard, A. van Ulden, and H. Cuijpers (2003), *Simulation of present-day climate in RACMO2: first results and model developments*, Koninklijk Nederlands Meteorologisch Instituut.

Ligtenberg, S., M. Heilsen, and M. van de Broeke (2011), An improved semi-empirical model for the densification of Antarctic firn, *The Cryosphere*, *5*(4), 809–819.

Lythe, M. B., and D. G. Vaughan (2001), BEDMAP: A new ice thickness and subglacial topographic model of Antarctica, *Journal of Geophysical Research: Solid Earth*, *106*(B6), 11,335–11,351.

Marco Tedesco, X. F., and P. M. Alexander (2013), MAR v3.2 regional climate model data for Greenland, *NSF Arctic Data Center*, doi:10.5065/D6JH3J7Z.

Moran, M. J., H. N. Shapiro, D. D. Boettner, and M. B. Bailey (2010), *Fundamentals of engineering thermodynamics*, John Wiley & Sons.

Mori, M., M. Watanabe, H. Shiogama, J. Inoue, and M. Kimoto (2014), Robust arctic sea-ice influence on the frequent eurasian cold winters in past decades, *Nature Geoscience*, *7*(12), 869–873.

Morlighem, M., E. Rignot, J. Mouginot, H. Seroussi, and E. Larour (2014), Deeply incised submarine glacial valleys beneath the Greenland Ice Sheet, *Nature Geoscience*, *7*(6).

Mote, T. L. (2003), Estimation of runoff rates, mass balance, and elevation changes on the Greenland Ice Sheet from passive microwave observations, *Journal of Geophysical Research: Atmospheres*, *108*(D2).

Nghiem, S., D. Hall, T. Mote, M. Tedesco, M. Albert, K. Keegan, C. Shuman, N. DiGirolamo, and G. Neumann (2012), The extreme melt across the Greenland Ice Sheet in 2012, *Geophysical Research Letters*, *39*(20).

Nowicki, S., et al. (2013), Insights into spatial sensitivities of ice mass response to environmental change from the searise ice sheet modeling project ii: Greenland, *Journal of Geophysical Research: Earth Surface*, *118*(2), 1025–1044.

Oerlemans, J., et al. (1998), Modelling the response of glaciers to climate warming, *Climate dynamics*, *14*(4), 267–274.

Ohmura, A. (2001), Physical basis for the temperature-based melt-index method, *Journal of Applied Meteorology*, *40*(4), 753–761.

Oleson, K. W., et al. (2010), Technical description of version 4.0 of the Community Land Model (CLM), *Tech. rep.*, NCAR.

Pfeffer, W. T., M. F. Meier, and T. H. Illangasekare (1991), Retention of Greenland runoff by refreezing: implications for projected future sea level change, *Journal of Geophysical Research: Oceans*, *96*(C12), 22,117–22,124.

Pfeffer, W. T., J. Harper, and S. O'Neel (2008), Kinematic constraints on glacier contributions to 21st-century sea-level rise, *Science*, *321*(5894), 1340–1343.

Pritchard, H. D., R. J. Arthern, D. G. Vaughan, and L. A. Edwards (2009), Extensive dynamic thinning on the margins of the Greenland and Antarctic ice sheets, *Nature*, *461*(7266), 971–975.

Reeh, N. (1989), Parameterization of melt rate and surface temperature on the Greenland Ice Sheet, *Polarforschung*, *59*(3), 113–128.

Reeh, N. (1999), Mass balance of the Greenland Ice Sheet: Can modern observation methods reduce the uncertainty?, *Geografiska Annaler: Series A, Physical Geography*, *81*(4), 735–742.

Reeh, N., C. Mayer, H. Miller, H. H. Thomsen, and A. Weidick (1999), Present and past climate control on fjord glaciations in Greenland: Implications for IRD-deposition in the sea, *Geophysical Research Letters*, *26*(8), 1039–1042.

Reijmer, C., E. Van Meijgaard, and M. Van den Broeke (2005), Evaluation of temperature and wind over Antarctica in a Regional Atmospheric Climate Model using 1 year of automatic weather station data and upper air observations, *Journal of Geophysical Research: Atmospheres*, *110*(D4).

Reijmer, C., M. Van den Broeke, X. Fettweis, J. Ettema, L. Stap, et al. (2012), Refreezing on the Greenland Ice Sheet: a comparison of parameterizations, *The Cryosphere*, *6*, 743–762.

Rignot, E., and J. Mouginot (2012), Ice flow in Greenland for the international polar year 2008–2009, *Geophysical Research Letters*, *39*(11).

Rignot, E., J. Box, E. Burgess, and E. Hanna (2008), Mass balance of the Greenland Ice Sheet from 1958 to 2007, *Geophysical Research Letters*, *35*(20).

Robinson, A., R. Calov, and A. Ganopolski (2012), Multistability and critical thresholds of the Greenland Ice Sheet, *Nature Climate Change*, *2*(6), 429–432.

Shepherd, A., et al. (2012), A reconciled estimate of ice-sheet mass balance, *Science*, *338*(6111), 1183–1189.

Singh, P., and N. Kumar (1996), Determination of snowmelt factor in the Himalayan region, *Hydrological sciences journal*, *41*(3), 301–310.

Stroeve, J. C., J. E. Box, and T. Haran (2006), Evaluation of the MODIS (MOD10A1) daily snow albedo product over the Greenland Ice Sheet, *Remote Sensing of Environment*, *105*(2), 155–171.

Tedesco, M., X. Fettweis, M. Van den Broeke, R. Van de Wal, C. Smeets, W. J. van de Berg, M. Serreze, and J. Box (2011), The role of albedo and accumulation in the 2010 melting record in Greenland, *Environmental Research Letters*, *6*(1), 014,005.

Tedesco, M., X. Fettweis, T. Mote, J. Wahr, P. Alexander, J. Box, and B. Wouters (2013), Evidence and analysis of 2012 Greenland records from spaceborne observations, a regional climate model and reanalysis data, *Cryosphere (The)*, *7*, 615–630.

Tedesco, M., S. Doherty, X. Fettweis, P. Alexander, J. Jeyaratnam, and J. Stroeve (2016), The darkening of the Greenland Ice Sheet: trends, drivers, and projections (1981–2100), *Cryosphere (The)*, *10*, 477–496.

Van Angelen, J., J. Lenaerts, S. Lhermitte, X. Fettweis, P. Kuipers Munneke, M. Van den Broeke, E. Van Meijgaard, C. Smeets, et al. (2012), Sensitivity of Greenland Ice Sheet surface mass balance to surface albedo parameterization: a study with a regional climate model, *The Cryosphere*, *6*, 1175–1186.

Van den Broeke, M., J. Bamber, J. Ettema, E. Rignot, E. Schrama, W. J. van de Berg, E. van Meijgaard, I. Velicogna, and B. Wouters (2009), Partitioning recent Greenland mass loss, *science*, *326*(5955), 984–986.

Van den Broeke, M., C. Bus, J. Ettema, and P. Smeets (2010), Temperature thresholds for degree-day modelling of Greenland Ice Sheet melt rates, *Geophysical Research Letters*, *37*(18).

Van Dusen, M. (1929), Thermal conductivity of non-metallic solids, in *International critical tables of numerical data, physics, chemistry and technology*, vol. 5, pp. 216–217, McGraw-Hill New York.

Van Meijgaard, E., L. Van Ulft, W. Van de Berg, F. Bosveld, B. Van den Hurk, G. Lenderink, and A. Siebesma (2008), The KNMI regional atmospheric climate model RACMO version 2.1, *Koninklijk Nederlands Meteorologisch Instituut*, *43*.

Van Tricht, K., S. Lhermitte, J. T. Lenaerts, I. V. Gorodetskaya, T. S. LEcuyer, B. Noël, M. R. van den Broeke, D. D. Turner, and N. P. Van Lipzig (2016), Clouds enhance Greenland Ice Sheet meltwater runoff, *Nature communications*, *7*.

Van Wessem, J., et al. (2014), Improved representation of East Antarctic surface mass balance in a regional atmospheric climate model, *Journal of Glaciology*, *60*(222), 761–770.

Vaughan, D. G., et al. (2013), Observations: cryosphere, *Climate change*, pp. 317–382.

Velicogna, I. (2009), Increasing rates of ice mass loss from the Greenland and Antarctic ice sheets revealed by GRACE, *Geophysical Research Letters*, *36*(19).

Vernon, C. L., J. Bamber, J. Box, M. Van den Broeke, X. Fettweis, E. Hanna, and P. Huybrechts (2013), Surface mass balance model intercomparison for the Greenland Ice Sheet, *Cryosphere (The)*, *7*, 599–614.

Vionnet, V., E. Brun, S. Morin, A. Boone, S. Faroux, P. Le Moigne, E. Martin, and J. Willemet (2012), The detailed snowpack scheme Crocus and its implementation in SURFEX v7. 2, *Geoscientific Model Development*, *5*, 773–791.

Wallace, J. M., and P. V. Hobbs (2006), *Atmospheric science: an introductory survey*, vol. 92, Academic press.

Wientjes, I., and J. Oerlemans (2010), An explanation for the dark region in the western melt zone of the Greenland Ice Sheet, *The Cryosphere*, *4*(3), 261–268.

Wientjes, I., R. Van de Wal, G.-J. Reichart, A. Sluijs, and J. Oerlemans (2011), Dust from the dark region in the western ablation zone of the Greenland Ice Sheet, *The Cryosphere*, *5*(3), 589–601.

Yau, M. K., and R. Rogers (1996), *A short course in cloud physics*, Elsevier.

Zuo, Z., and J. Oerlkmans (1996), Modelling albedo and specific balance of the Greenland Ice Sheet: calculations for the Sendre Stromøord transect, *Journal of glaciology*, *42*(141), 305–317.

Zwally, H. J., W. Abdalati, T. Herring, K. Larson, J. Saba, and K. Steffen (2002), Surface melt-induced acceleration of Greenland ice-sheet flow, *Science*, *297*(5579), 218–222.